ABSTRACT

Title of dissertation: SILICON-BASED TERAHERTZ WAVEGUIDES

Shanshan Li, Doctor of Philosophy, 2015

Dissertation directed by: Professor Thomas E. Murphy
Department of Electrical and Computer Engineering

In this thesis, we present the design, fabrication and measurement of two types of silicon-based terahertz waveguides. The first is anisotropically etched highly doped silicon surface for supporting terahertz plasmonic guided wave. We demonstrate propagation of terahertz waves confined to a semiconductor surface that is periodically corrugated with subwavelength structures. We observe that the grating structure creates resonant modes that are confined near the surface. The degree of confinement and frequency of the resonant mode is found to be related to the pitch and depth of structures. The second is silicon dielectric ridge waveguide used to confine terahertz pulses and study silicon's terahertz intensity-dependent absorption. We observe that the absorption saturates under strong terahertz fields. By comparing the response between lightly-doped and intrinsic silicon waveguides, we confirm the role of hot carriers in this saturable absorption. We introduce a nonlinear dynamical model of Drude conductivity that, when incorporated into a wave propagation equation, predicts a comparable field-induced transparency and elucidates the physical mechanisms underlying this nonlinear effect. The results

are numerically confirmed by Monte Carlo simulations of the Boltzmann transport equation, coupled with split-step nonlinear wave propagation.

SILICON-BASED TERAHERTZ WAVEGUIDES

by

Shanshan Li

Dissertation submitted to the Faculty of the Graduate School of the
University of Maryland, College Park in partial fulfillment
of the requirements for the degree of
Doctor of Philosophy
2015

Advisory Committee:
Professor Thomas E. Murphy, Chair/Advisor
Professor Neil Goldsman
Professor Phillip A. Sprangle
Professor Steven Anlage
Professor Kiyong Kim

Dedication

To my parents.

Acknowledgments

During past 5 years of PhD study and research, there are so many people helped and encouraged me. I want to express my sincere thanks to all of them here.

First, I would like to express my deepest gratitude to my advisor and mentor, Professor Thomas E. Murphy, for his invaluable guidance and support. Without his brilliant advice and continuous encouragement, this thesis can not be possible. He has always been helpful and patient. From him, I've not only learned how to do research, but also learned how to be a better person.

I would like to thank all my colleagues, Dr. Gagan Kumar, Ryan J. Suess, Mohammad Mehdi Jadidi, Kyowon Kim, Dr. Vincent R. Pag*á*n, Dr. Jeremiah J. Wathen, Dr. Martin Mittendorff, and Dr. Shu-Zee Alencious Lo. In particular, I want to thank Dr. Gagan Kumar, who introduced me to the terahertz world and helped me conduct experiments, fabricate samples and do simulations. Their passion for research encouraged me. Their extraordinary understanding of nonlinear optics helped me. It's a great pleasure to work with them.

Last but not the least, I'd like to owe my great gratitude to my parents, Zhiguo Li and Shanling Zhao. In the past 27 years, they always stand by me and support me unconditionally. Their love guided me to overcome all the difficulties.

Table of Contents

List of Figures

Chapter 1: Introduction

Terahertz (THz) spectrum (Fig. 1.1) loosely can be defined as 0.1-10 THz. Wavelengths cover from 30 μm to 3 mm. Lying between well-developed microwave and infrared in the electromagnetic spectrum, it's least explored. Hence THz region is called "THz-gap". Since mid-1980s, tremendous work has been done to approach this region from microwave, the low frequency side, and infrared, the high frequency side. Technologies for THz application are rapidly growing and filling up the gap. Milestones include the development of THz time domain spectroscopy, THz imaging, and high power(mJ) THz generation. These innovations find application in an increasing wide variety of fields: spectral fingerprint [6]; biology and medical sciences [7]; homeland security [8]; next generation wireless transmission [9]; and monitoring

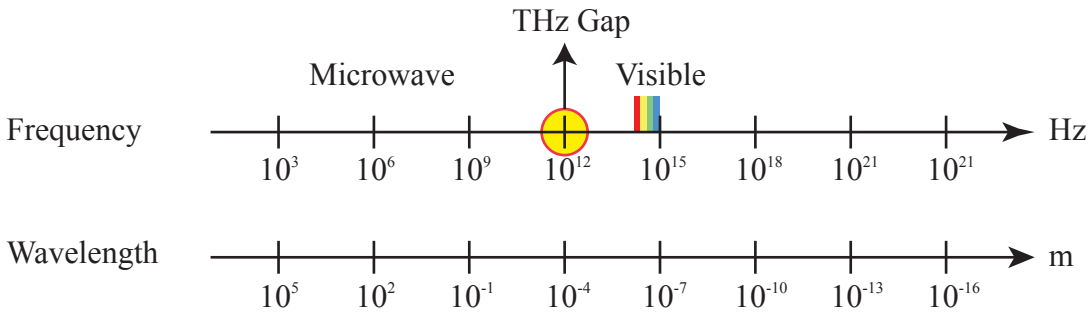

Figure 1.1: The electromagnetic spectrum.

the Earth's atmosphere [10].

1.1 Terahertz waveguides

The delivery of THz is very important for both communication and sensing applications. In recent years, there has been significant interest in developing guided wave components operating in the terahertz regime for applications that include bio-sensing [11,12], imaging [13], slow light devices [14], modulators and lasers [15]. Since terahertz is positioned between microwave and infrared, technology to study this region can be borrowed from both sides. Researchers proposed several terahertz waveguides solutions based on electronic and optical technologies, such as parallel plate waveguides [16,17], metal wire waveguides [18], dielectric hollow core waveguides [19], and dielectric solid core waveguides [20]. Metallic waveguides are downscaled versions of microwave guiding devices, as most metals at THz frequencies still behave like perfect conductor and metallic structures can be used for guidance in this region. Dielectric waveguide, technology from optical frequency range, is another major category of terahertz waveguides. Low absorption loss dielectrics in THz region, such as high-resistivity silicon(absorption loss<0.05 cm^{-1}), with proper fabrication of geometries can also be good candidate for THz guidance. Several reported terahertz waveguides have been listed in Table. 1.1. For metallic waveguides, loss comes from finite conductivity of the metals in THz frequencies. And the propagating mode suffers high dispersion around cut-off frequency if the dominant mode is not TEM mode. While for dielectric waveguide, the attenuation and distortion

Table 1.1: Several Typical Terahertz Waveguides

Terahertz waveguide	Material	Dimension(μm)	Absorption coefficient(cm^{-1})	reference
Circular waveguides	Stainless steel	Diameter=280	0.7	[24]
Parallel plate waveguides	Copper	Distance=108	0.1	[25]
Metal wire	Stainless steel	Diameter=900	0.03 for TM_{01}	[18]
Fish line	Polyethylene	Diameter=200	0.01	[20]
Teflon pipe	Teflon	Diameter=9000	0.0008	[26]
Polymer porous-core fiber	cyclic olefin copolymer	Diameter=900	0.08	[27]

of terahertz wave are due to material absorption and dispersion from material and geometry.

In this thesis, we present the fabrication and application of two types of silicon-based terahertz waveguides. One is anisotropically etched highly doped silicon surface for supporting THz plasmonic guided wave [21], [22]. The other is intrinsic silicon ridge waveguide used to study silicon's terahertz intensity-dependent absorption [23].

1.2 Characteristics of silicon

Among all the dielectrics, silicon is one of the most favorable materials for terahertz applications. The linear absorption and index of refraction of silicon in terahertz region have been studied since 1990s with the development of Terahertz Time Domain Spectroscopy(THz-TDS).

From previous work [1], intrinsic silicon shows exceptionally low loss and negligible group-velocity dispersion in THz region (shown in Fig. 1.2). These properties make intrinsic Si appealing to be used as windows, quasi-optic lens, and dielectric slab or ribbon waveguides. For better understanding of the importance of intrinsic silicon, Table. 1.2 provides the properties at 1 THz of several popular materials for terahertz optics production. Among all the materials, undoped silicon is the most transparent.

However, the excellent transparency is only the behavior of intrinsic or high resistivity silicon. The absorption of terahertz wave in silicon is greatly carrier density dependent. With increasing doping density of free carriers, silicon can become almost opaque. When silicon doping density exceeds 10^{19} cm^{-3}, it exhibits metallic properties at terahertz frequencies. Fig. 1.3 displays how the real and imaginary permittivity ϵ of doped silicon change with doping density. Absorption is related to permittivity by $\alpha = \frac{\mathrm{Im}(n)\omega}{c} = \frac{\mathrm{Im}(\sqrt{\epsilon})\omega}{c}$. With doping density above 10^{19} cm^{-3}, the permittivity and thus absorption strongly increase. A comparison of relative permittivity and skin depth at 1 THz of highly-doped Si, gold and copper is shown in Table. 1.3. We can directly conclude that highly doped silicon behaves like metal.

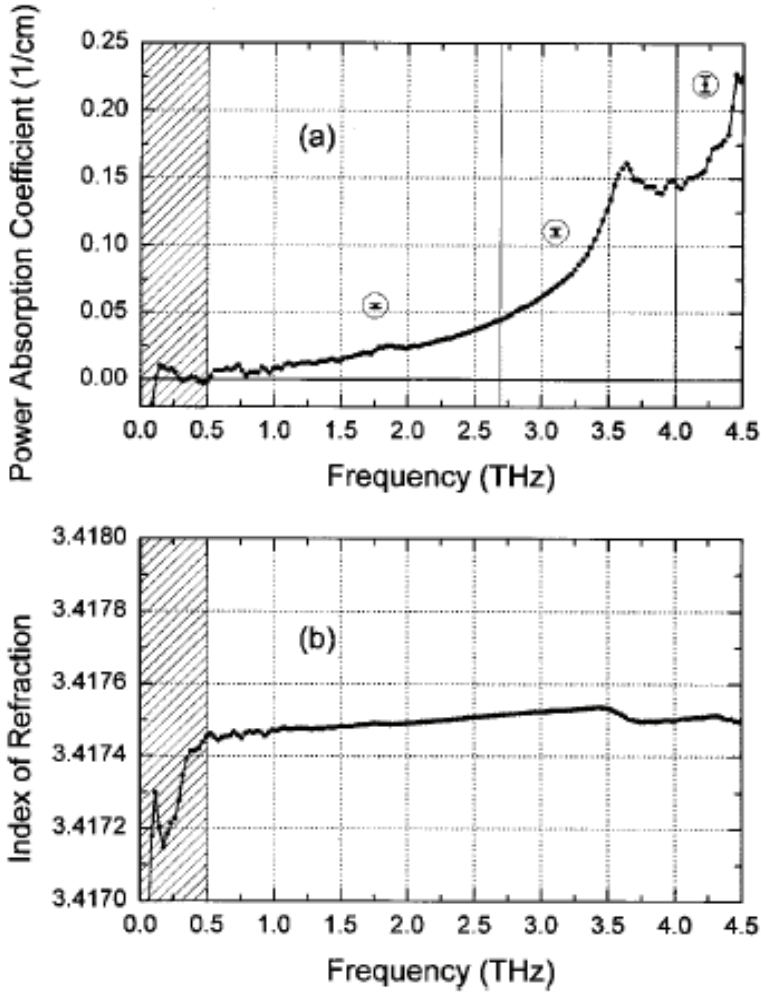

Figure 1.2: (a) The power absorption coefficient and (b)measured refractive index of float-zone, high-resistivity silicon [1]

Table 1.2: Properties of several important THz materials at 1 THz

Material	Refractive index	Absorption(cm^{-1})
High resistivity(10 kΩ·cm) silicon	3.44	0.02
Sapphire	3.41/3.07	1.0
Quartz	2.15/2.11	0.1
Fused silica	1.95	2.0
TPX	1.46	0.4
PTFE	1.43	0.6
PMMA	1.5	20
HDPE	1.54	0.4

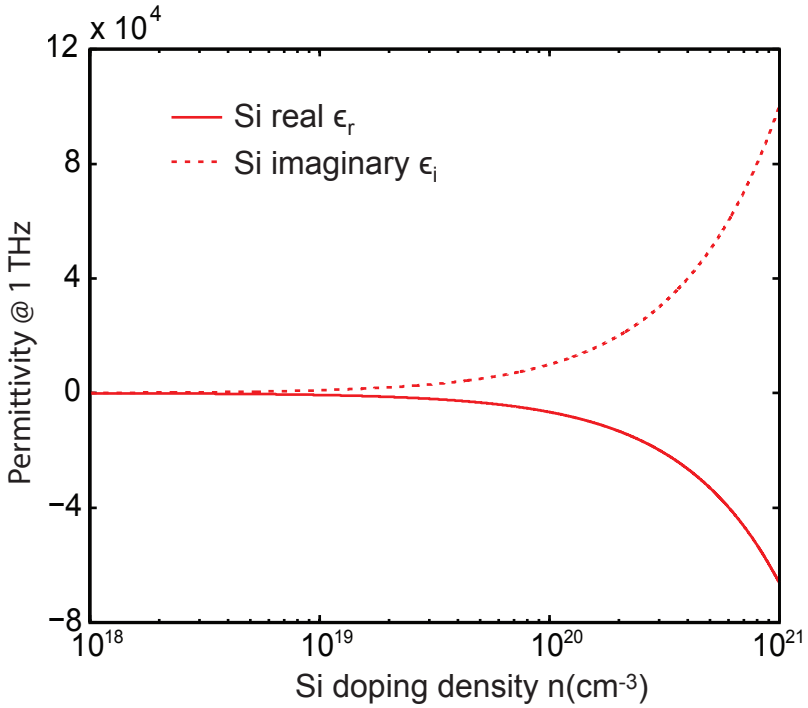

Figure 1.3: Doped Si real and imaginary permittivity versus doping density.

And compared to metal, it's easier to pattern periodically sub-wavelength structures with mature fabrication technologies. It can therefore replace metal to fabricate THz plasmonic waveguide, which we will discuss later.

Previous work of silicon in terahertz region are mostly focused on linear properties of this material. The loss in silicon is typically described by the Drude model [28] [29]. The Drude model treats free carriers in solid in a classical way and provides a good prediction of the carriers' linear behavior inside bulk silicon. The Drude model predicts the frequency-dependent complex dielectric constant, conductivity and absorption are:

$$\epsilon = \epsilon_\infty + i\sigma/\omega\epsilon_0, \tag{1.1}$$

Table 1.3: Relative permittivity and skin depth at 1 THz

Material	Relative permittivity	Skin depth(μm)
Silicon (n=4×10^{19} cm^{-3})	(-1.3+2i)×10^4	0.35
Gold	(-1.1+7.2i)×10^5	0.074
Copper	(-3.36+4.46i)×10^4	0.23

$$\sigma = \sigma_{dc} i\Gamma/(\omega + i\Gamma) = i\epsilon_0\omega_p^2/(\omega + i\Gamma), \tag{1.2}$$

$$\alpha = \frac{q^2 N\Gamma}{\epsilon_0 c m^* n(\omega^2 + \Gamma^2)}, \tag{1.3}$$

in which ϵ_∞ is the contribution of the bound electrons, Γ is the momentum scattering rate, $\omega_p = Nq^2/\epsilon_0 m^*$ is plasma frequency, m^* is effective mass, N is the doping density, $\sigma_{dc} = e\mu N$ represents DC conductivity, q is the elementary charge, ϵ_0 is the free-space permittivity, $n = Re(\sqrt{\epsilon})$ is the real part refractive index, and c is the free-space light velocity. α is the absorption coefficient. Intensity decays with distance as $I(z) = I(0)\,\mathrm{e}^{-\alpha z}$. Since the relation between momentum scattering rate Γ and carrier mobility μ is $\mu = q/(m^*\Gamma)$, the Drude absorption sometimes is represented as:

$$\alpha = \frac{qN\Gamma^2\mu}{\epsilon_0 c n(\omega^2 + \Gamma^2)}. \tag{1.4}$$

This formula is more useful when we discuss how field-dependent mobility effects absorption in section 1.4.3.

We note here that the original Drude model is linear and thus doesn't reveal any evidence of field-dependent absorption. In Chapter 3, we will propose a modified Drude model to support the nonlinear absorption we observed in silicon.

1.3 Terahertz plasmonic wavguides

1.3.1 Surface plasmon polaritons (SPPs)

In infrared and visible electromagnetic frequencies, plasmonic waveguides (like those shown in Fig. 1.4(a), in which electromagnetic wave is highly confined at the surface of metallic material, can offer simple geometry and sub-wavelength confinement of a guided mode. The bounded electromagnetic wave is called surface plasmon polariton, which can exist at the interface between any two materials where the real part of the dielectric function changes sign across the interface. This surface plasmon concept originates in the plasma approach of Maxwell's theory: the free electrons of a metal are treated as an electron liquid of high density and density fluctuations occurring on the surface of such a liquid are called plasmons. From Maxwell's theory, excitation of the surface plasmons can only be achieved by using TM incidence beam. The dispersion relation for the surface mode is [30]:

$$k_x = \frac{\omega}{c}\sqrt{\frac{\epsilon_m \epsilon_d}{\epsilon_m + \epsilon_d}}, \epsilon_m + \epsilon_d < 0, \tag{1.5}$$

in which ϵ_m and ϵ_d are relative permittivity of metal and dielectric respectively, c is the free space light velocity. Fig. 1.4(b) shows typical dispersion relations for radiative mode, quasi-bound mode and this plasmonic or bound mode obtained from

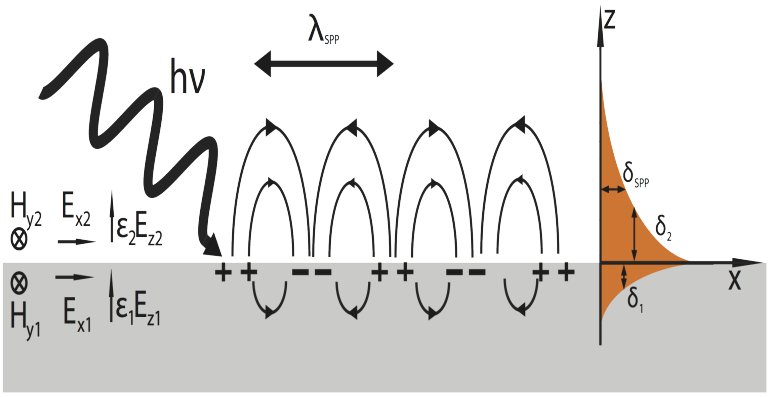

(a)

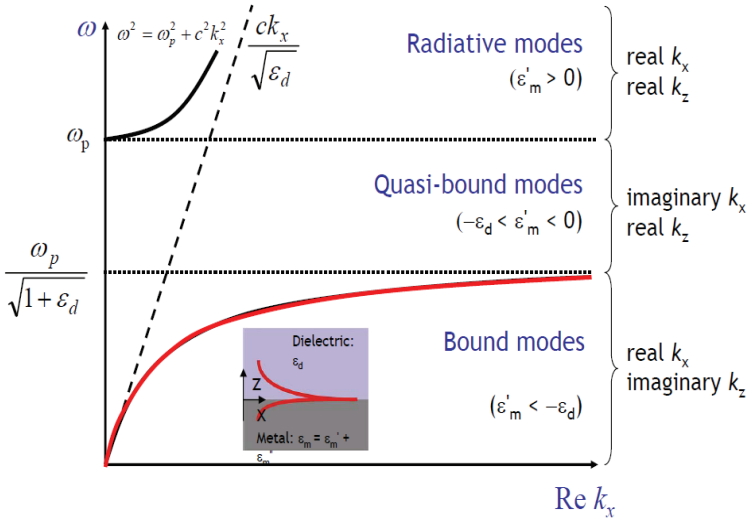

(b)

Figure 1.4: (a)Surface plasmon polaritons travel along metal-dielectric interface(`http://en.wikipedia.org/wiki/Surface_plasmon`). (b)Dispersion relation for bound mode(surface plasmon), quasi-bound mode and radiative mode(`http://optics.hanyang.ac.kr/~shsong/27-Metals.pdf`)

Maxwell equations. We can see the curve of plasmonic mode at the beginning follows the light line and then bends over and reaches limit(called surface plasma frequency ω_{sp}) at high frequency, which leads to slower group velocity and tighter confinement. The relation between surface plasmon frequency and plasmon frequency is

$$\omega_{sp} = \frac{\omega_p}{\sqrt{1+\epsilon_d}}. \tag{1.6}$$

Because of its sub-wavelength spatial confinement, this type of waveguide finds applications in sensing and switching. However, at THz frequencies, traditional plasmonic metals and highly doped dielectrics have negligible penetration depth and behave like perfect conductors. Therefore, traditional surface plasmons cannot exist in this frequency region.

1.3.2 Mimicking Surface Plasmons with structured surfaces in THz region

In order to compensate the wavevector mismatch and mimic plasmonic dispersion at optical wavelengths where metals behave like perfect conductor, Pendry proposed [31] and developed [2] a method—periodically patterning conductive surface. Grating structure on conductive surface creates resonant modes that are confined near the surface. The schematic for rectangular apertures that Pendry used in his 2004 paper is shown in Fig. 1.5(a). By supposing an effective homogeneous field in surrounding material and arguing the instantaneous flow of energy across the surface must be the same, he calculated the dispersion relation for this structure is:

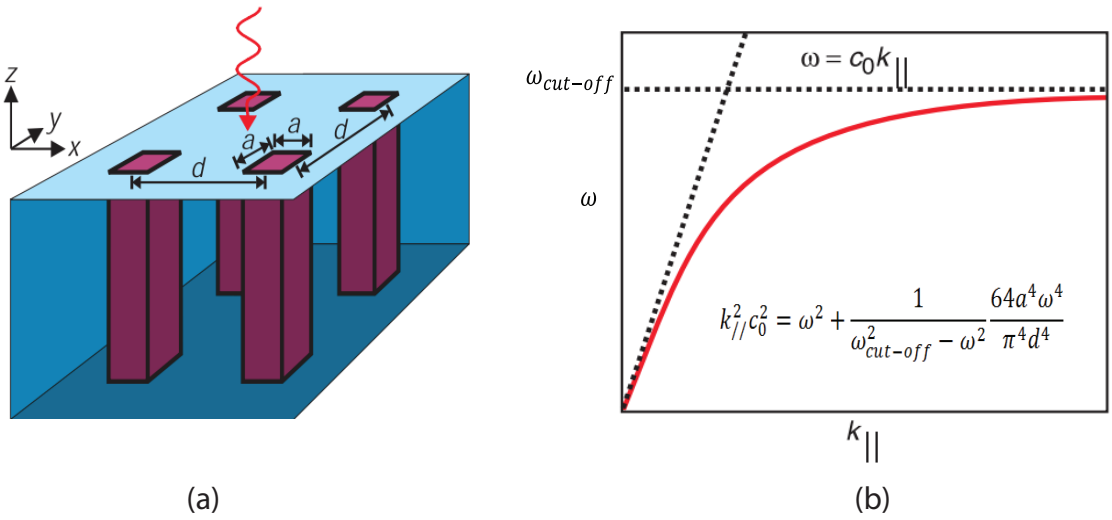

Figure 1.5: (a)Schematic and (b)dispersion relation of rectangular apertures. [2]

$$k_{//}^2 c^2 = \omega^2 + \frac{1}{\omega_{cut-off}^2 - \omega^2} \frac{64a^4\omega^4}{\pi^4 d^4}, \; \omega_{cut-off} = \frac{\pi c}{a\sqrt{\epsilon_h \mu_h}} \tag{1.7}$$

and ploted in Fig. 1.5(b). In Eq. 1.7, $k_{//}$ is the wave vector along the metal surface, c is the free space light velocity, d is the distance between each hole, a is the length of these square apertures, $\omega_{cut-off} = \frac{\pi c}{\sqrt{\epsilon_h \mu_h}}$ is the cut-off frequency of this waveguide, and ϵ_h and μ_h are the permittivity and permeability of any material that may be filling the holes. By comparing Fig. 1.5(b) and Fig. 1.4(b), we can conclude this kind of structure mimicks the dispersion relation of a traditional surface-plasmon polariton. The limit the dispersion relation reached is the exactly cut-off frequency of this waveguide. Pendry pointed out this technology can be applied to any frequency(metals are nearly perfect conductors from zero frequency to terahertz regime)even where traditional surface plasmons do not exist before.

Since then, much experimental, theoretical, and numerical work has been re-

ported on terahertz plasmonic waveguides using metallic corrugated surface. Several geometries, including metallic aperture [32], rectangular gratings [33], triangular grooves [34], have been demonstrated and shown to support highly confined surface modes.

In these previous work, fabrication of corrugated structures on metal has been proved to be challenging because of the difficulty of patterning or etching metal. There is a need for alternative substrate. By recalling that silicon, when heavily doped($> 10^{19}$ cm^{-3}), can be treated as perfect conductor in THz regime and can therefore replace the periodic metallic structures originally used to guide waves. Moreover, this approach can benefit from the mature silicon fabrication technologies. What's more, unlike metals, the dielectric properties of silicon can be manipulated by changing doping density or photo-illumination, or current injection which in turn determines the degree of confinement and loss for plasmonic wave. In Chapter 2, we will show terahertz time domain measurements and simulated results for plasmonic waveguide based on anisotropically etched silicon substrate.

1.4 Nonlinear terahertz exploration

1.4.1 High power terahertz generation

Traditional terahertz generation methods include photoconductive antenna, optic rectification in second-order nonlinear crystals like ZnTe or GaP and photo-dember effect on InAs. These low terahertz energy sources provide 0.1-10 THz bandwidth and enable applications like terahertz imaging and spectroscopy. However,

for important applications such as terahertz pump-terahertz probe measurement of dynamics and terahertz electron spin resonance, high power terahertz source is required. In recent years, several group reported the development of high power terahertz generation. One solution is to use free electron pump laser [35]. This can provide 10-100 μJ terahertz. However, the large-scale pump facility is not easily accessible. Another solution utilizes large-aperture photoconductive switch [36] illuminated by ultrashort laser pulses, which can produce 1 μJ in energy. However, strong saturation of generated THz signal limits scaling with increasing laser pulse energy. Some group reported by using large aperture ZnTe [37], they can also generate μJ terahertz pulse through optical rectification. Efficiency of this method is limited by the free carriers absorption in ZnTe. The record for high THz field generation is with nonlinear organic crystals [38,39], such as DAST. This kind of crystals has very high nonlinear coefficient(for example second order nonlinear coefficient d_{eff}=615 pmV^{-1} for DAST) and can generate 8 GV/m [39] THz by optical rectification. However, nonlinear organic crystal is not widely used due to difficulties with fabrication. Nowadays, two most appealing high power terahertz generation methods are terahertz generation using two-color mixing in plasma [40] [41] and optical rectification of femtosecond laser in $LiNbO_3$(LN) with tilted pump pulse scheme [42] [43].

Two color mixing generation: This technique generates single-cycle high power THz pulses by mixing fundamental ω and second-harmonic 2ω pump pulses in gas plasma. Typical schematic of this method is shown in Fig. 1.6. In most experiments, fundamental pump beam has a center wavelength of 800 nm. A Beta

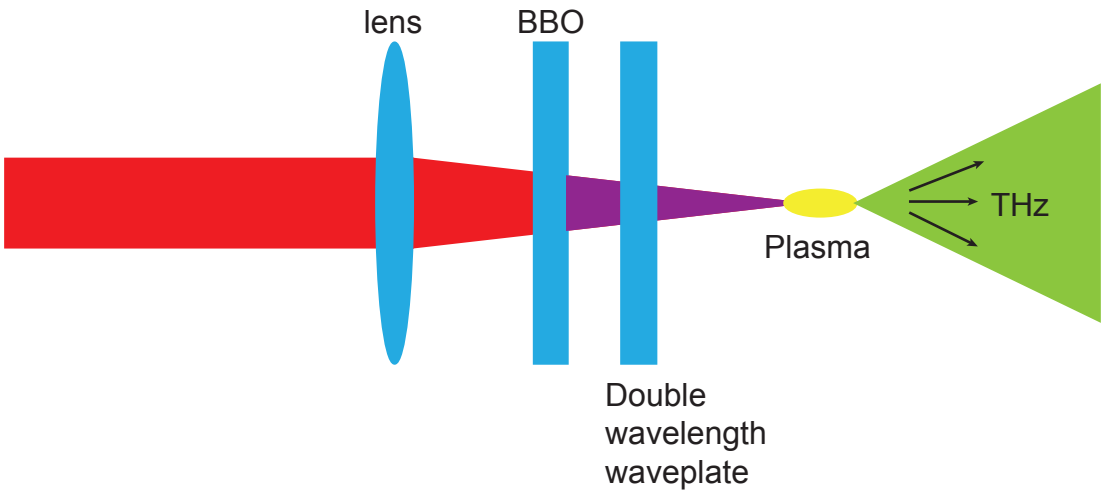

Figure 1.6: Experiment setup for terahertz two-color generation.

Barium Borate(BBO) crystal is used to generate second-harmonic, in this case 400 nm. A double wavelength waveplate, half wave plate at 800nm and full wave plate at 400nm, is used to rotate 400 nm to be polarized in the same direction as 800 nm for highly efficient THz generation. The 800 nm and 400 nm pump pulses are focused by a lens to generate plasma in gas. Third order nonlinear effect takes place in plasma and generates THz. There is no damage threshold for the emitter since effective media is gas. Conversion efficiency from optical to THz energy exceeded 10^{-4} [44]. And the bandwidth is only limited by pump laser duration. THz pulses with several μJ power has been reported using this technique [45].

Generation by optical rectification in $LiNbO_3$: Another widely used method for ultrashort high field THz generation is utilizing tilted pump pulse technique for efficient optical rectification in $LiNbO_3$(LN) [43, 46]. In this thesis, our high power terahertz source is based on tilted pump-pulse scheme. Compared to ZnTe(d_{eff}=68.5

pmV^{-1}) or GaP(d_{eff}=24.8 pmV^{-1}), $LiNbO_3$(d_{eff}=168 pmV^{-1}) has much larger nonlinear coefficient for optical rectification generation. What's more, LN is an attractive nonlinear crystal because it has a higher band gap than other commonly used EO materials. This makes LN less susceptible to multiphoton absorption of the excitation laser pulses. Multiphoton absorption is known to not only give a higher possibility for optical damage to the crystal, but also generate free carriers in the nonlinear material that screen the THz generation. This is considered the major cause of saturation in THz generation through optical rectification when high excitation laser power is used for other crystals. The higher band gap allows LN crystals to hold higher laser power, and thus delivers stronger THz radiation.

However, unlike ZnTe or GaP, this crystal is not automatically fulfill the velocity-matching requirement for efficient optical rectification. The group velocity of the (near-IR) pump is more than two times larger then the THz phase velocity. The THz wave and NIR beam "walk away" from each other in a short distance. The large angle between THz and optical beam also brings difficulty in coupling the THz wave out of the LN. This greatly limits LN's application. In 2002, Hebling [47] proposed to use tilted pulse front pumping (TPFP) scheme (shown in Fig. 1.7) to realize velocity matching in $LiNbO_3$ and generated μJ terahertz radiation. By diffracting the incoming ultrashort pump pulse off an optical grating, we can introduce a tilt of the pulse front and make the projected group velocity of the pump onto the propagation direction of the THz radiation be equal to the THz phase velocity. This velocity matching condition can be expressed as:

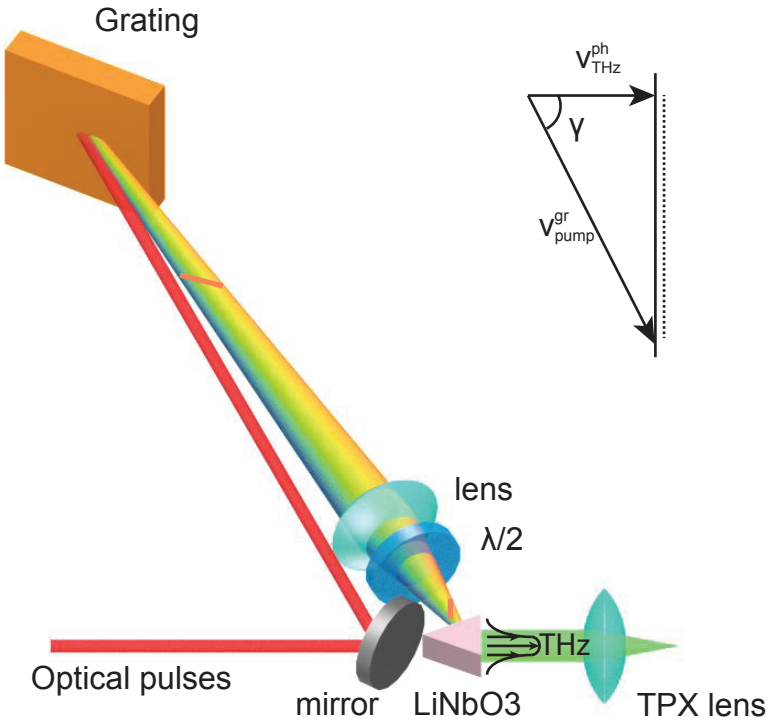

Figure 1.7: Typical experiment setup of tilted pulse front pumping method. Inset is velocity matching using TPFP

$$v_{Pump}^{group} \cdot \cos(\gamma) = v_{THz}^{phase}. \tag{1.8}$$

For LN, $\gamma = 63° at 1THz$ for LN. The lens in Fig. 1.7 enlarges the angular dispersion introduced by the grating and recreates the original short pulse duration inside of the medium by imaging the grating surface into the crystal. Orange lines are tilted pulse fronts of pump beam before and after the lens. A half-wave plate rotates the polarization of pump beam to align with LN's optical axis for maximizing optical rectification effect. By changing the grating and imaging parameters, the experimental setup can easily be adapted to different pump wavelengths and repetition rates.

Thereafter, this technology is rapidly developed. More than 1 MV/cm [43] and up to 125 μJ per pulse [46] terahertz has been generated. This greatly inspired and enabled terahertz nonlinear optics exploration.

1.4.2 Terahertz nonlinear spectroscopy

The interaction of THz radiation with semiconductors has been studied extensively and include effects such as free carrier absorption, the photon drag effect or intersubband transitions. However, few studies have been reported on the nonlinear terahertz characteristics of semiconductors using high fields.

With development of high power terahertz sources, terahertz induced nonlinear transmission has began to be observed in a variety of bulk semiconductors,

including Si [3, 4], Ge [3], GaAs [48–53], GaP [54] and InSb [55–57], and numerous hot carrier effects have been offered as explanations, including intervalley scattering, band nonparabolicity, and impact ionization.

Terahertz induced transparency [3]: In 2010, the time evolution of hot carrier distribution and the cooling was studied in Ge, GaAs and Si by using THz-pump/THz probe scheme. In all samples, high field terahertz induced absorption bleaching has been observed. And from the spectral analysis of the data, it can be seen the characteristics of the hot electron gas deviates significantly from the Drude behavior.

Terahertz induced impact ionization: When high power terahertz is directed to low bandgap semiconductor such as InSb [56], it can accelerate electrons inside InSb to overcome the bandgap and lead to increase in absorption caused by newly generated electron-hole pairs. This impact ionization phenomenon has been observed by Nelson's group using THZ-pump/THz-probe spectroscopy. More recently, Jepsen's group reported impact ionization in high resistivity silicon when the peak THz field exceeds 1 MV/cm, a condition that is difficult to experimentally achieve [58]. They utilized metal resonant antenna to concentrate the original hundred kV/cm THz field.

Nonlinear THz response at 2D metamaterial: Recently, two groups [59, 60] employed two-dimensional terahertz metamaterial to study the nonlinear transmission at semiconductor surface, and phenomenologically modeled the observations by a change in conductivity. Al-Naib used silicon as the substrate and observed enhanced transmission when increasing THz field from 0.4 to 90 kV/cm. Fan fabri-

cated a similar structure on GaAs. He observed enhanced transmission by increasing THz field from 20 to 160 kV/cm. However, reversed effect happened when the THz field was increased above that range. The reason for this reversal is that impact ionization increases the carrier concentration leading to suppressed transmission.

In most previous cases, the observations were carried out using wafers or windows with optical thickness of only a few terahertz wavelengths. In such thin samples, the cumulative nonlinearity is necessarily quite small, and it is difficult to separate propagation effects from interface effects such as small changes in reflectivity, or spatial effects such as self-focusing and diffraction. In this thesis, we will fabricate silicon ridge waveguide to increase interaction length between THz and carriers while maintaining high power THz in small region.

1.4.3 Silicon nonlinear terahertz phenomenon

Nonlinear properties of silicon, such as drift velocity saturation [61], impact ionization [62], two photon absorption [63], and self phase modulation [64], are fully studied in DC, mid IR and near IR. However until recently, terahertz induced nonlinear effects are less explored due to lack of high power terahertz source. In 2010, both Hebling [3](Fig. 1.8(a)) and Kaur [4](Fig. 1.8(b)) examined high power THz induced absorption bleaching in n-doped bulk silicon. Their work showed when terahertz field increased from several kV/cm to several hundreds of kV/cm, silicon became more transparent. More recently, Jepsen's group observed MV/cm teraherz induced impact ionization in high resistivity silicon wafers [58].

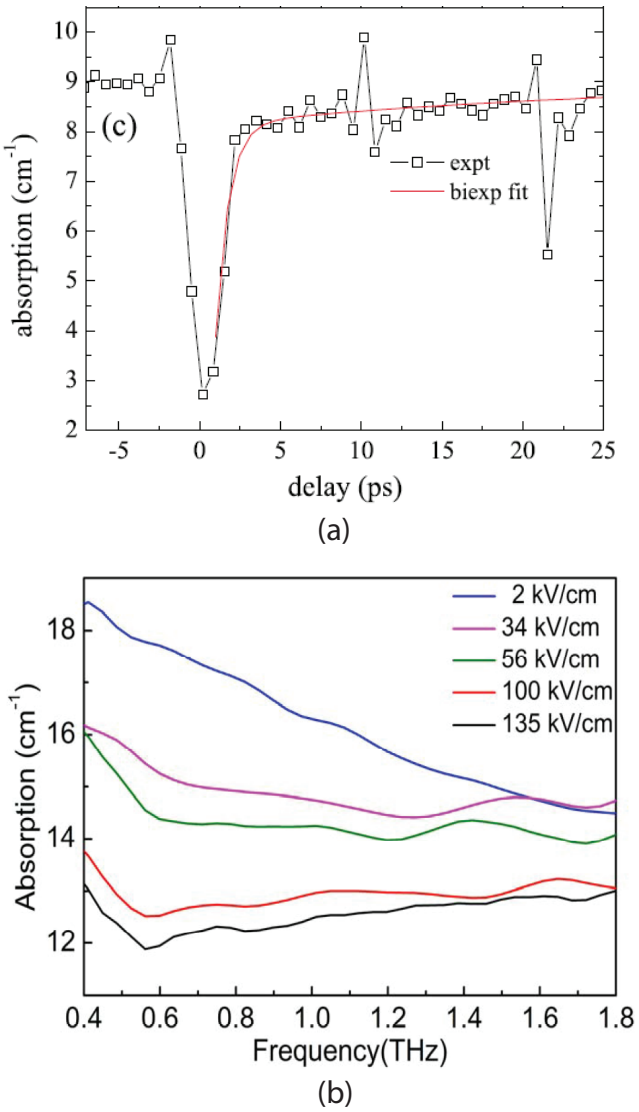

Figure 1.8: (a) Dynamic behavior of the saturation of free-carrier absorption in the n-type Si measured by terahertz pump terahertz probe method [3](b)Absorption of n-doped Si under different applied THz field [4].

As carriers dynamics play a important role in determining silicon absorption, most previous work used doped bulk silicon to study intensity-dependent absorption. Intrinsic or lightly doped bulk silicon is almost not studied for its negligible carrier-based absorption in THz regime. In order to overcome this difficulty, we fabricated Si ridge waveguide to increase interaction length between THz and carriers while maintaining high power THz in small region. Again, we observed high terahertz($\leq$100 kV/cm) induced transparency in lightly doped silicon ridge waveguides.

The absorption of silicon is related to mobility by Eq. 1.3. Inter-valley scattering, and thus higher effective mass and lower mobility, has been suggested to cause this saturable absorption. However, for better understanding of underlying physics, more rigorous study is needed. Hot carriers' transport is described by Boltzmann Transport Equation(BTE). Since Monte Carlo simulation is known to be able to provide precise solution to this equation, in this thesis, we develop a THz Monte Carlo simulation to study the nonlinear transmission phenomenon. It's known that carrier drift velocity saturates in bulk silicon for applied DC field above 45 kV/cm(Fig. 1.9 [5]), leading to a field-dependent reduction in mobility. We checked whether drift velocity behaves a similar way under high THz signal and causes reduction in absorption in silicon by using Monte Carlo simulation assembled with split-step nonlinear wave propagation in chapter 3. We also introduce a nonlinear dynamical model of Drude conductivity that, when incorporated into a wave propagation equation, accurately reproduces the observations and elucidates the physical mechanisms underlying this nonlinear effect.

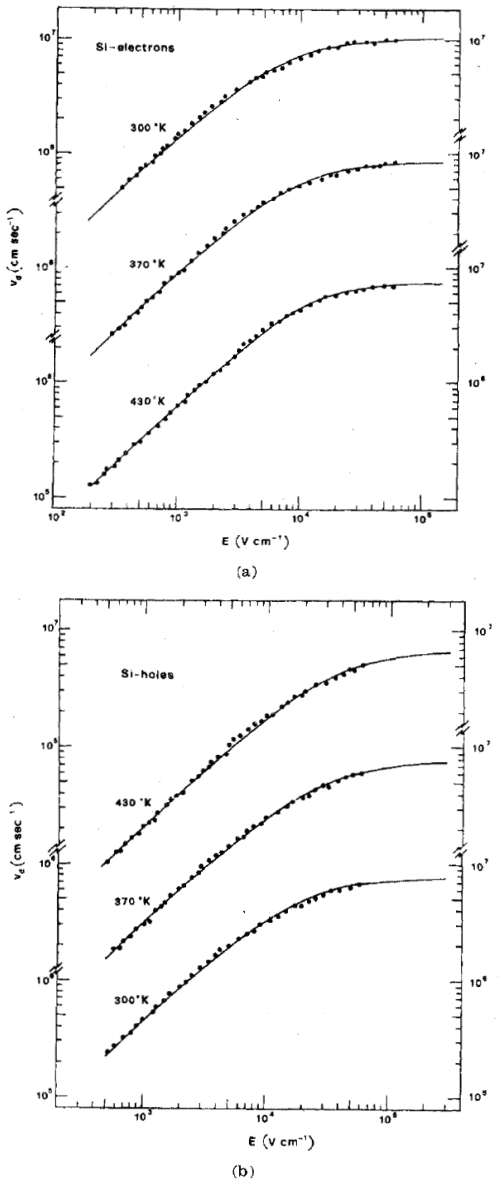

Figure 1.9: (a)Electron and (b)hole drift velocity in silicon as a function of electric field at three different temperatures. The points are the experimental data and the continuous line are from $v_d = \mu \frac{E}{\left[1+(E/E_c)^\beta\right]^{1/\beta}}$ [5].

1.5 Summary of dissertation

This thesis is mainly focused on two types of silicon-based terahertz waveguides and their applications. In this chapter, we introduced the background and motivation of our research. Current status and basic knowledge of terahertz waveguide, surface plasmon polaritons, high power terahertz generation, and silicon nonlinear terahertz phenomenon were discussed.

In chapter 2, we describe terahertz spoof plasmon polariton propagation on a highly doped silicon surface that is patterned with periodic V-grooves. Terahertz time domain spectroscopy is used to characterize the surface wave, and shows evidence of a resonant mode that is confined to the surface. Numerical and experimental measurements reveal that the resonant frequency and degree of confinement can be adjusted by tailoring the depth and period of the structures. Numerical simulations reveal that deeper structures can provide tighter surface confinement and slower group velocities for the resonant mode.

In chapter 3, we discuss the fabrication of silicon ridge waveguide and experimental setup for studying nonlinear terahertz optics. The field-induced transparency and associated carrier velocity saturation is shown to be dynamical effect that cannot be adequately explained by a modified effective mobility or Drude model. We present a simple, nonlinear Drude model that explains the observations, and we confirm the model using rigorous Monte Carlo simulations. Further, we introduce a numerical split-step method that models the interplay of nonlinearity and dispersion in the wave propagation. These results could have important consequences in fu-

ture high-power terahertz guidedwave nonlinear devices, such as terahertz frequency converters, parametric oscillators, mixers, and modulators.

In chapter 4, details about our Monte Carlo simulation introduced in chapter 3 are provided. First, ways to estimate input terahertz field amplitude in the simulation are introduced. Then processes and parameters of Monte Carlo simulation are presented. Velocity saturation at high THz field(obtained from Monte Carlo simulation) is observed for both electrons and holes.

In chapter 5, we briefly summarize this thesis and discuss the potential application of our nonlinear results and model.

Chapter 2: Plasmonic terahertz waveguide based on anisotropically etched highly doped silicon substrate

In recent years, electromagnetic waves propagating at the interface between a metal and dielectric have been of significant interest [18, 65–70]. These waves allow for sub-wavelength confinement of the field, overcoming the diffraction limit, and opening the possibility for unprecedented device miniaturization. Possible applications of surface waves include bio-sensing [71], nonlinear phenomenon [72], material characterization and surface enhanced Raman scattering [69, 73].

At visible and near infrared frequencies, many conventional metal surfaces support localized surface plasmon polariton modes that can be excited using prism-coupling method [74]. Such method cannot be applied at terahertz frequencies, where most metals behave more like perfect electrical conductors. In 2004, Pendry et.al proposed the introduction of a periodic texture to a conducting surface in order to compensate for the wavevector mismatch, thus allowing for excitation of surface waves with a wavenumber that exceeds that of the excitation [2]. Thereafter, extensive experimental and theoretical work has been reported on the excitation and confinement of surface waves using surface corrugations [75–81]. Highly confined surface modes have been demonstrated in several geometries, including metallic

apertures, blind holes, rectangular gratings, and others. Most of these devices have used laser micromachining, or planar photolithographic techniques such as liftoff, reactive-ion etching, thin-film deposition, and electroplating to form rectangular conductive features on a substrate.

More recently, other geometries have been proposed for plasmonic waveguides, including triangular surface grooves [34,82–86]. At telecommunication wavelengths, isolated V-groove structures have been experimentally verified to guide channel plasmon polariton with subwavelength confinement and low loss at bends [87,88]. More recently, Wood *et al.* numerically analyzed a surface plasmon mode sustained by periodic array of slanted rectangular grooves in a conductive substrate [89]. Fabrication of non-rectangular grooves in a metallic substrate has proved challenging because of the difficulty of patterning or etching metal, and consequently most of the prior research on such structures has been numerical.

In crystalline silicon, V-groove geometries and pyramidal troughs can be readily fabricated by employing anisotropic wet etching [90]. At terahetz frequencies, silicon can exhibit metallic properties when heavily doped and can be used to efficiently propagate surface plasmon polaritons when patterned with subwavelength structures. Unlike metals, the dielectric properties of silicon can be adjusted by controlling the free carriers concentration through doping, photoexcitation, or current injection, which in turn determines the degree of confinement and the loss for the plasmonic wave – an additional degree of freedom that is unavailable in most plasmonic substrates.

In this chapter, we report two types periodic structures, v-grooves and pyra-

midal troughs, patterned on highly doped silicon and serve as terahertz plasmonic waveguide. Terahertz time domain spectroscopy is used to characterize the surface wave, and shows evidence of a resonant mode that is confined to the surface. Numerical and experimental measurements reveal that the resonant frequency and degree of confinement can be adjusted by tailoring the depth and period of the structures. Numerical simulations reveal that deeper structures can provide tighter surface confinement and slower group velocities for the resonant mode.

2.1 V-groove waveguides

2.1.1 Numerical analysis of surface modes

Fig. 2.1a depicts the geometry of the semiconductor plasmonic waveguide considered here. The substrate is comprised of crystalline silicon that is patterned through anisotropic etching, such that the sides of the V-grooves are parallel to the $\langle 111 \rangle$ and $\langle \bar{1}\bar{1}1 \rangle$ crystallographic planes. The apex angle θ is therefore constrained to be $\theta = \tan^{-1}\sqrt{8} = 70.53°$, and the width-to-height ratio is likewise constrained to be $w/h = 2\tan\theta/2 = \sqrt{2}$. The pitch and height of the corrugation can be controlled through lithographic processing.

Fig. 2.1b depicts the calculated dispersion relation for three different grating line widths of $w = 100$, 200, and 250 μm, each with the same grating pitch of $p = 250$ μm. The dispersion curves were calculated using the finite difference time-domain method, and the solid black curve indicates the light line for wave propagation in the free-space region. We note that as the width (and hence the depth) of the V-

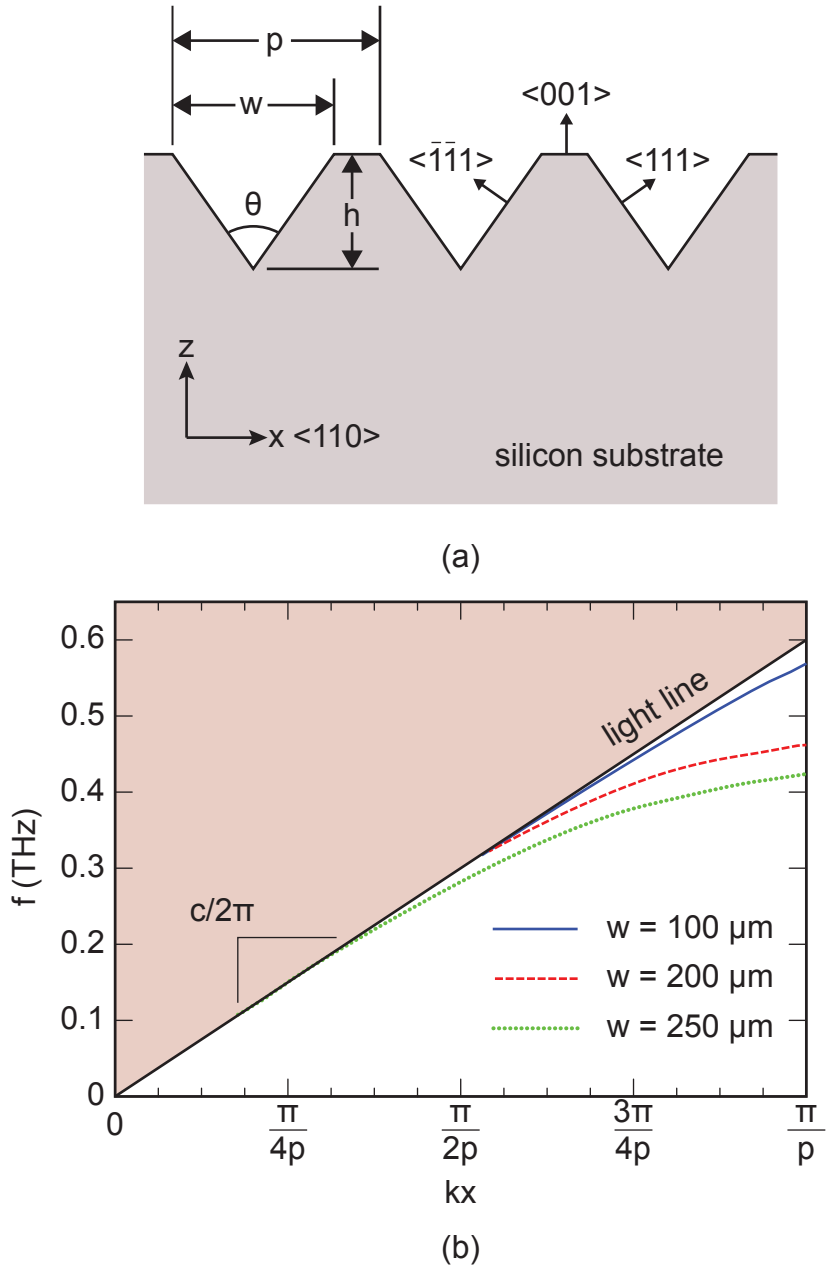

Figure 2.1: (a) Geometry of semiconductor plasmonic V-groove waveguide fabricated on a silicon substrate. The width and height are related by $w/h = 2\tan\theta/2 = \sqrt{2}$. (b) Numerically computed dispersion relations of the fundamental surface mode for three different line widths (w).

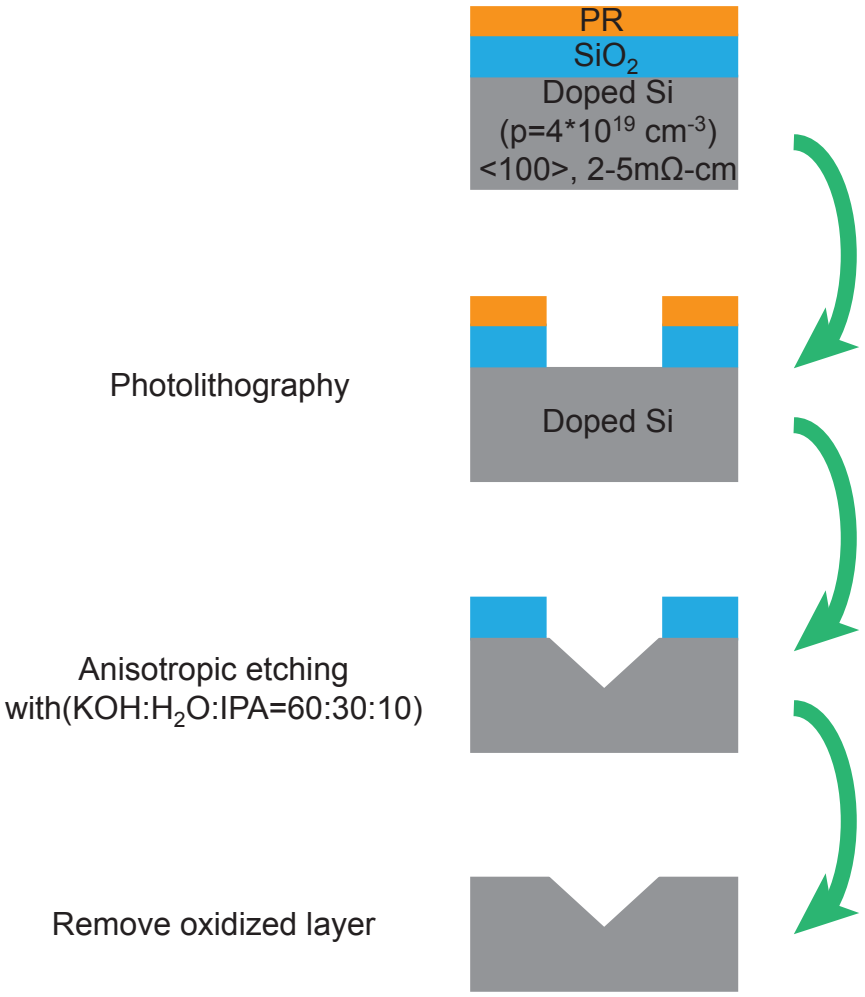

Figure 2.2: Anisotropic etching process

grooves is increased, the dispersion of the wave shows a pronounced curvature away from the light line, indicating slower phase and group velocities, especially near the first Brillouin edge.

2.1.2 Fabrication

The fabrication process is shown in Fig. 2.2. We fabricated our strutures on $\langle 100 \rangle$ boron-doped silicon wafers with resistivity of 2-5 mΩ·cm (dopant concertraion

4×10^{19} cm^{-3}). 1.2 μm thick silicon dioxide layer was deposited on both sides of substrate by using low pressure chemical vapor deposition (LPCVD). This layer was then patterned using UV contact photolithography followed by wet etching in buffered hydrofluoric acid, to produce a periodic array of openings in the SiO_2 film. The sample was then immersed in a solution of potassium hydroxide, water, and isopropanol in the ratio of 60:30:10 at a temperature of 80 °C to perform the anisotropic etching which forms the V-grooves. During the etching, the depth of the V-groove h was estimated to increase at approximately 0.4 μm/s. Following the etching, the remaining oxide mask layer was removed in a buffered hydrofluoric acid solution. Fig. 2.3a shows a representative cross-sectional scanning electron micrograph of a completed structure. The grating lines were each 30 mm wide, which was much larger than the terahertz beam size, thus ensuring that the propagation could be adequately approximated as a two-dimensional structure. Each waveguide was composed of an array containing 200 grating lines at a pitch of $p = 250$ μm, for a total length of 50 mm. Groove widths of $w = 100$ μm and 200 μm were fabricated (with corresponding depths of 71 and 141 μm). It should be noted that comparing with the wavelength of interest discussed below, the considered parameters indicate that we are operating in the subwavelength limit.

In order to facilitate coupling from a free-space terahertz beam into the plasmonic waveguide, a second photolithographic step was used to pattern a shallow 300 μm wide groove at 5 mm away from the edge of the V-groove array. This groove was etched to a depth of 100 μm using deep reactive ion etching (DRIE). When a terahertz beam from free space impinges at normal incidence onto the coupling

groove, a portion of the radiation scatters into the plasmonic waveguide mode.

2.1.3 Experiment set-up

Fig. 2.3b depicts the terahertz time-domain spectroscopy system used to characterize the plasmonic waveguides. Pulses from an amplified Ti:sapphire laser system were split (80:20) into pump and probe beams that generate and detect the terahertz waveforms, respectively. The optical pulses were 43 fs in duration, at a repetition period of 1 kHz and a central wavelength of 800 nm. Terahertz pulses were generated using optical rectification in a 1 mm thick ⟨110⟩-oriented ZnTe crystal, with an input pulse energy of 1.2 mJ and beam diameter of 10 mm. The pump beam was synchronously chopped at a rate of 250 Hz. The terahertz radiation was collected and collimated using off-axis parabolic mirrors, and focused at normal incidence onto the rectangular coupling groove. The impinging terahertz beam was linearly polarized in the direction perpendicular to the grooves (i.e., with the magnetic field parallel to the grooves), in order to ensure that the scattered radiation couples into the TM-polarized plasmonic mode of the structure.

At the opposite edge of the corrugated structure, the emerging terahertz beam was electrooptically sampled using a similar ZnTe crystal, which was brought into contact with the substrate. The probe beam of diameter 0.5 mm was adjusted to co-propagate with the terahertz wave through the ZnTe crystal at a height of 0.5 mm from the surface. Following the electrooptic crystal, a quarter wave plate, Wollaston prism, balanced photoreceiver, transimpedance amplifier, and lock-in detector (not

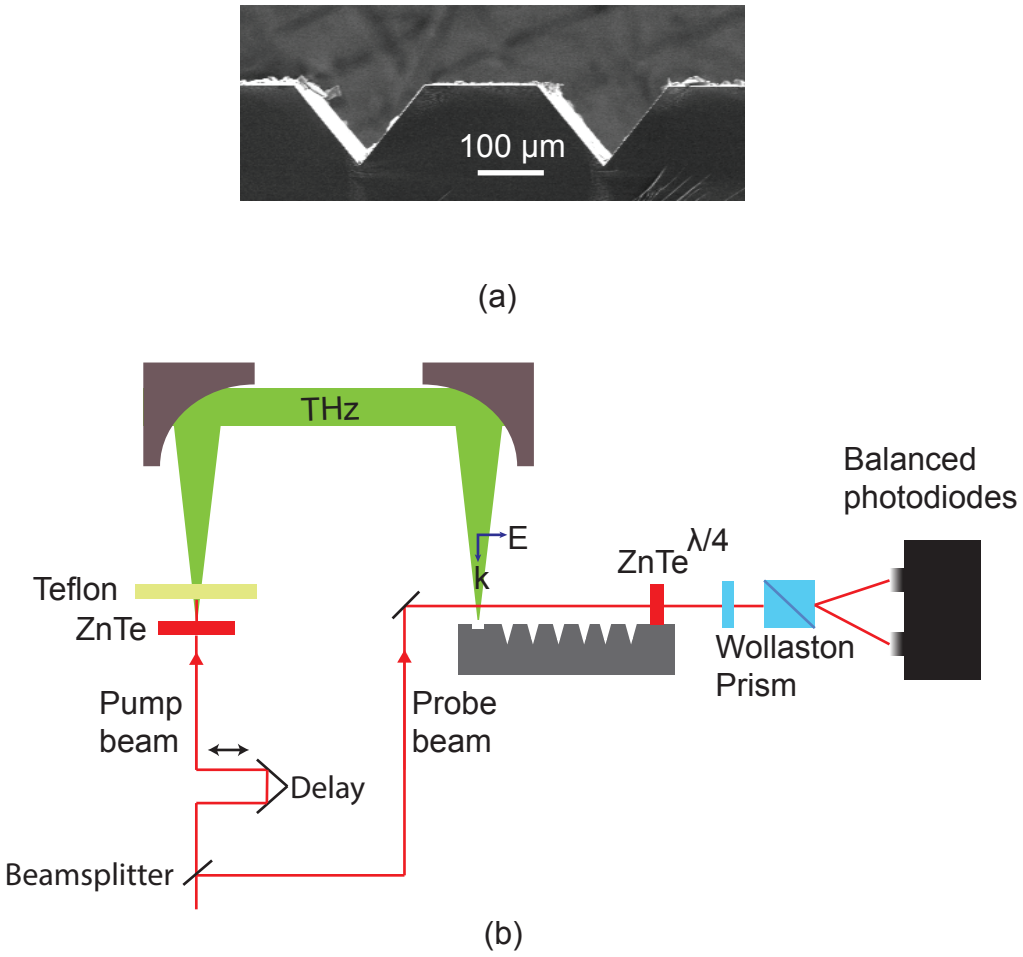

Figure 2.3: (a) Cross-sectional SEM image of a portion of the fabricated structure. (b) Schematic of the experimental setup. The ZnTe crystal is used to generate terahertz via photo-rectification. The detection is accomplished via electro-optic sampling using 1 mm thick (110) ZnTe crystal.

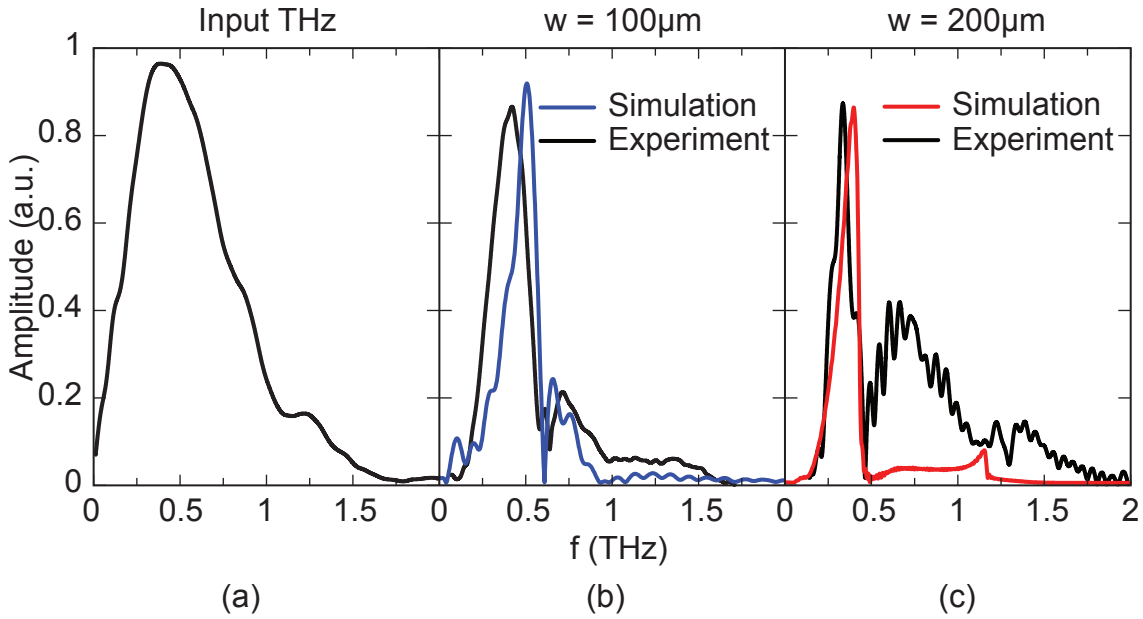

Figure 2.4: Experimentally measured frequency domain transmission spectra: (a) THz input signal used in the experiments, measured in back-to-back configuration. (b) Simulated (blue) and measured (black) transmission spectrum for plasmonic V-groove waveguide with $w = 100$ μm. (c) Simulated (red) and measured (black) transmission spectrum for plasmonic V-groove waveguide with $w = 200$ μm.

shown) were used to measure the terahertz electric field as the delay τ between the pump and probe was swept using a motorized translation stage.

2.1.4 Results

Fig. 2.4 shows the experimentally observed transmitted terahertz waveforms, together with numerical simulations obtained using finite element time-domain simulation. Fig. 2.4a depicts the input terahertz waveform, measured by redirecting the

terahertz wave directly to the electrooptic detector with the silicon waveguide absent. The simulations were conducted using the finite-element time-domain method, with perfect electrical conducting boundary conditions assumed at the silicon surface. For the dopant concentration considered here, the Drude model predicts a relative permittivity of $\epsilon = (-1.3 + 2.0i) \times 10^4$ at 1 THz, which is sufficiently large to justify treatment as a perfect conductor. To confirm the validity of the assumed PEC boundary conditions, we have repeated selected simulations using a more accurate 3D Drude model, and an equivalent surface impedance model, and found no significant difference in the numerical results.

Fig. 2.4b shows the terahertz spectrum measured at the output of the V-groove array, for the case when the grating line width was $w = 100$ μm. The blue curve shows the calculated spectrum obtained by numerically simulating the structure using the input waveform taken in Fig. 2.4a. Both the theory and numerical simulation show a pronounced null in the transmitted spectrum at a frequency of 0.58 THz. This frequency matches the frequency at the first Brillouin edge in Fig. 2.1, where the wavevector reaches p/π. The occurrence of null in the spectrum can be attributed to the interference effect occurring between the discrete resonance caused by the diffraction from the corrugations and the continuum transmission spectrum on the surface associated with the waveguide geometry. The interference effect between discrete and broad spectrum has been studied in the literature [91, 92]. The resonance associated with the null associated with strong confinement in the grating corrugations. The experimental measurements show weak Fabry-Pérot spectral fringes associated with multiple internal reflections inside of the ZnTe detection

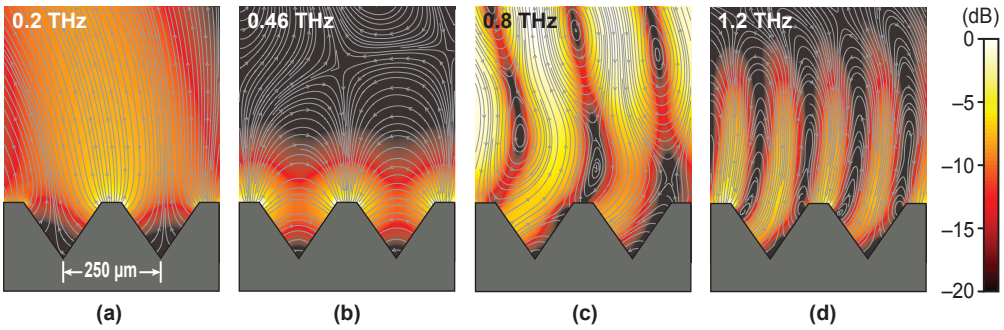

Figure 2.5: Electric fields calculated for $w = 200$ μm at four different frequencies below and above the resonant frequency: (a) 0.2 THz, below resonance, (b) 0.46 THz, on resonance, (c), 0.8 THz, above resonance, and (d) 1.2 THz, second-order resonance. The static frames shown here were captured at the peak of each cycle.

crystal, an effect that is not modeled in the simulation.

Fig. 2.4c shows similar results obtained when $w = 200$ μm. In this case, the null frequency associated with the fundamental resonance shifts to 0.46 THz, again in agreement with the frequency of the first Brillouin edge in Fig. 2.1. The measurements and simulations further reveal a higher-order resonance at approximately 1.2 THz.

To better illustrate the nature of the resonant plasmonic confinement, in Fig. 2.5 we plot the electric field profiles for the case when $w = 200$ μm, calculated at four different frequencies.

Fig. 2.5a shows the electromagnetic fields calculated at 0.2 THz, which is below the plasmonic resonant frequency. In this case, the wave propagation resembles as an unbound travelling wave above the surface, with no significant confinement in the periodic structure. In contrast, Fig. 2.5b shows the fields computed at the resonant

frequency of 0.46 THz. On resonance, the electromagnetic fields remain confined near the surface and inside of the V-grooves, and the spatial periodicity of the wave matches that of the grating. Fig. 2.5c shows the calculated fields at 0.8 THz (above resonance), again showing no significant surface confinement. Finally, in Fig. 2.5d we show the field profile at a frequency of 1.2 THz, which corresponds to a second-order resonance. In this case, the spatial periodicity of the wave matches the second spatial harmonic of the grating corrugation, and we again see plasmonic confinement near the surface (a weaker confinement than for the fundamental resonance.)

The degree of confinement in the plasmonic structure is closely related to the depth of the V-grooves, with deeper features producing stronger confinement. However, because of the anisotropic etching process used to fabricate the structures, the grating depth is restricted to be equal to $w/\sqrt{2}$. We note, however, that alternative fabrication methods, such as reactive ion etching, could potentially be used to produce V-grooves with much higher aspect ratios. Next we numerically analyze deeper V-grooves with a fixed width. Fig. 2.6a plots the calculated dispersion relation for three different plasmonic waveguides for which the pitch and width are fixed at p = 250 μm and w = 150 μm, respectively, but the apex angle is decreased from $\theta = 60^\circ$ to 20°. As before, in all cases the grating exhibits a resonant frequency at the edge of the Brillouin zone boundary, at which point the surface wave was found to be localized near the conductive surface. The steeper apex angles produce a much stronger deviation from the light line and a tighter confinement in the groove. Fig. 2.6b shows the related group velocity, obtained after numerically finding the slope of the dispersion curve. The steeper (and hence deeper) gratings show a slower

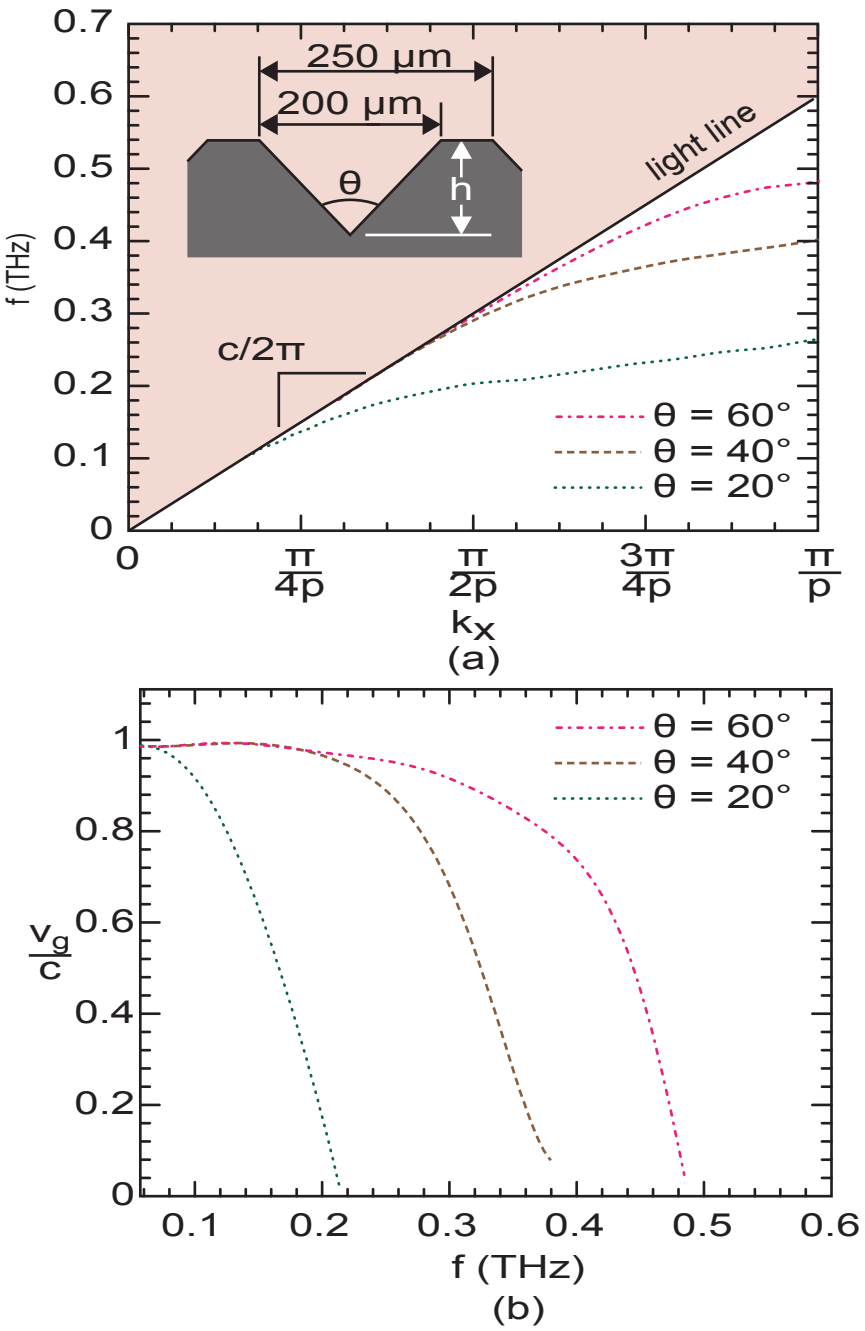

Figure 2.6: (a) Numerically calculated dispersion relation for the surface modes supported by a conductive grating structure with $p = 250$ μm, $w = 150\mu$m, and $\theta = 60°, 40°, 20°$. (b) The associated group velocity dispersion for the three structures considered in (a), showing the progressively slower wave velocities attained by increasing the depth of the grooves.

group velocity, associated with tighter confinement in the V-grooves.

In order to explain the correlations between the depth of the V-groove, the confinement of the surface mode, and the reduction in group velocity, we consider the special case of V-groove with an apex angle of 90°, which can be generalized from the recent analysis of Wood et al. [89]. In this case, the dispersion relation using quasi-analytical approach in the long wavelength limit and neglecting the higher order diffraction terms may be written as

$$k_x = k_0 \left[1 + 2 \left(\frac{h}{p} \tan \left(\frac{k_0 h}{\sqrt{2}} \right) \mathrm{sinc}^{-1} \left(\frac{k_0 h}{\sqrt{2}} \right) \right)^2 \right]^{\frac{1}{2}} \tag{2.1}$$

where k_x is the propagation constant in the x-direction (traveling wave direction), $k_0 = \frac{2\pi}{\lambda}$ is the free space propagation constant, h is the depth of the groove from the apex to the surface in normal direction and p is the periodicity. For the traveling surface plasma wave which has major component of the electric field in the transverse and the propagation direction, the transverse confinement factor (α) can be calculated as

$$\alpha = \left(k_x^2 - k_0^2 \right)^{1/2} \tag{2.2}$$

From the dispersion relation given in Eq. 2.1, one may easily calculate the group velocity of the traveling surface wave. We plot in Fig. 2.7 the confinement factor α and group velocity of the surface bound wave as a function of frequency for two different depths of $h = 50$ μm and $h = 75$ μm, using $p = 250$ μm and $\theta = 90°$. One may note that confinement factor increases with the frequency while group

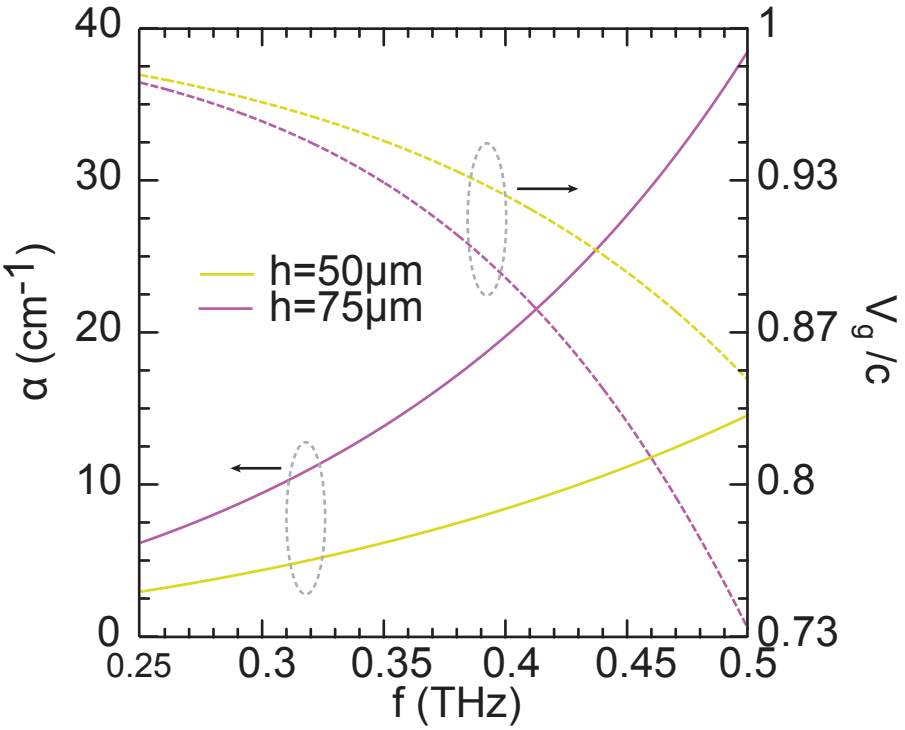

Figure 2.7: Variation of confinement factor and group velocity of the fundamental surface mode with the terahertz frequency for two different depths i.e. $h = 50$ μm and $h = 75$ μm of V-grooves. The solid line corresponds to confinement while the dotted curves corresponds to the group velocity of the surface mode.

velocity decreases. At any frequency considered, the deeper grooves show a higher confinement factor and smaller group velocity than the corresponding shallow-groove structure. Although the theoretical relationship only applies to the special case of $\theta = 90°$, our numerical simulations suggest that these general relations should also hold true for other V-groove structures as well.

2.2 Transverse confinement using pyramidal troughs

We have already demonstrated silicon V-grooves corrugations are able to provide vertical confinement of THz waves to the surface. Here, we show a one-dimensional array of finite width silicon troughs can serve as a THz plasmonic waveguide and provide confinement in both transverse directions.

2.2.1 Fabrication and Experiment set-up

We followed similar fabrication process as described above. The waveguide samples were fabricated on $\langle 100 \rangle$ oriented boron-doped silicon substrates by using anisotropical etching. The etching forms concave rectangular trough bounded by four facets aligned with the $\langle 111 \rangle$,$\langle \bar{1}\bar{1}1 \rangle$,$\langle \bar{1}11 \rangle$, and $\langle 1\bar{1}1 \rangle$ crystal planes, as shown in Fig. 2.8a. Each side facet is inclined at an angle of 54.73° with respect to the $\langle 100 \rangle$ surface. A 300 μm long, 100 μm deep and 2.5 mm wide coupling groove is separately fabricated using deep reactive ion etching near the input side of the waveguide to facilitate scattering of the normally incident THz wave into the surface plasmonic mode.

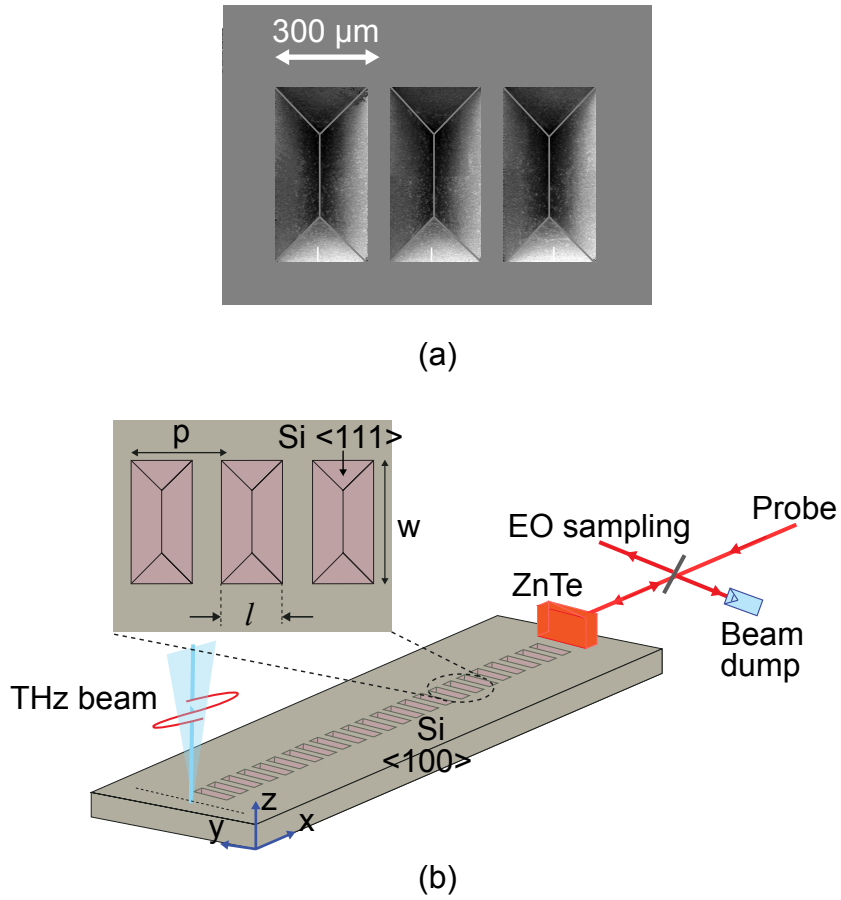

Figure 2.8: (a) Scanning electrom micrograph of a portion of anisotropically etched troughs in silicon.(b) Schematic of the plasmonic waveguide comprising a periodic array of pyramidal troughs in silicon. A rectangular groove at the input end is used to promote coupling in the out-of-plane direction.

A modified terahertz time domain spectroscopy system was employed to characterize the plasmonic waveguides (Fig.2.3b and Fig.2.8b). The focused THz beam of about 3 mm diameter is normally incident on the coupling groove. By comparing the intensity measured after the coupling groove to that obtained by replacing the device with an off-axis parabolic mirror, we estimated input coupling efficiency to be 10 %. After propagating along the patterned surface, the emerging THz wave is measured using a $\langle 110 \rangle$ oriented ZnTe crystal of thickness 1 mm, brought into close proximity to the surface.

2.2.2 Results

In our study, we fabricated three waveguide samples, each with a length of 5 cm and periodicity of $p = 300$ μm. The length and width of the rectangular troughs were varied. Fig. 2.9 shows both the experimentally observed (black) and numerically simulated (red) time domain signals for the case where the trough dimensions were 500×250 μm ($w \times l$). The corresponding frequency domain spectra, obtained by Fourier transform, are shown on the right panel of Fig. 2.9.

Both experiment and simulation exhibit resonant behavior, as evidenced by the long-lived oscillations in the time-domain traces and the corresponding null in the frequency spectra at 0.45 THz. The observed resonant frequency agrees well with that predicted numerically. Some discrepancies between the experimental measurement and numerical prediction exist, which we attribute to diffractive losses, interference from unguided radiation, and multiple internal reflections in the ZnTe

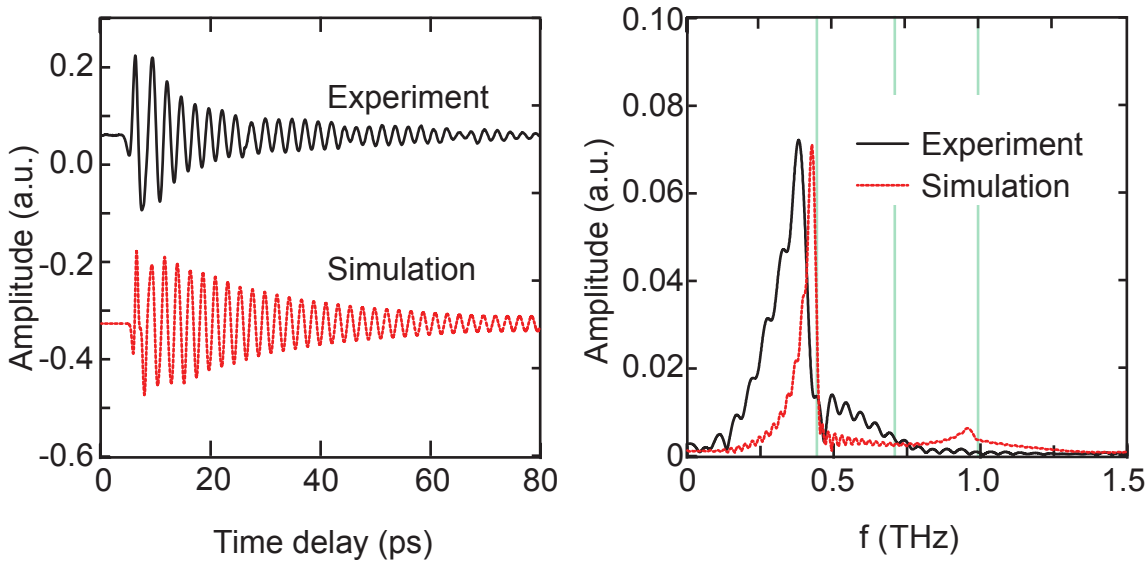

Figure 2.9: Time domain signal (left) and corresponding frequency domain spectra (right) of the transmitted THz waveform for a 300 μm period array of 500×250 μm ($w \times l$) troughs.

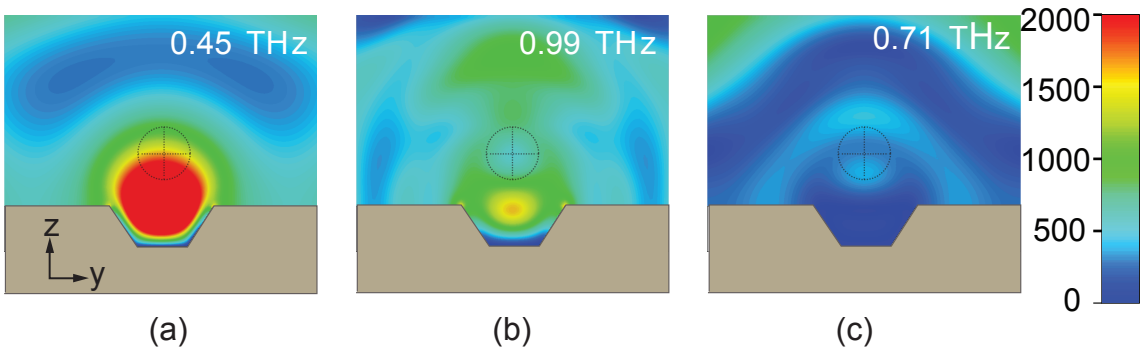

Figure 2.10: Simulated electric field profile evaluated at the center of a trough (a) at the resonant frequency (0.45 THz), (b) higher-order resonance (0.99 THz) and (c) off-resonance (0.71 THz). The dashed cross-hairs indicate the approximate size and position of the optical probe beam used in the experiment.

detection crystal–effects that are not captured by the simulation.

In order to better illustrate the mode behavior, in Fig. 2.10 we plot the numerically simulated electric field at the resonant frequency, evaluated in a cross sectional plane at the center of one trough. Clearly, at the resonant frequency of 0.45 THz, the field is highly confined within the trough. The simulated traces also show evidence of a higher order resonance 0.99 THz that is not as tightly-confined, as shown in Fig. 2.10(b). By contrast, at the off-resonance frequency of 0.71 THz the field profile is not confined to the surface, as shown in Fig. 2.10(c). Because of losses at higher frequencies, the higher order resonances were more difficult to observe experimentally.

Fig. 2.11(a) shows similar measurements and simulations performed on devices with trough dimensions of 500×200 μm and 400×250 μm ($w \times l$). While the overall

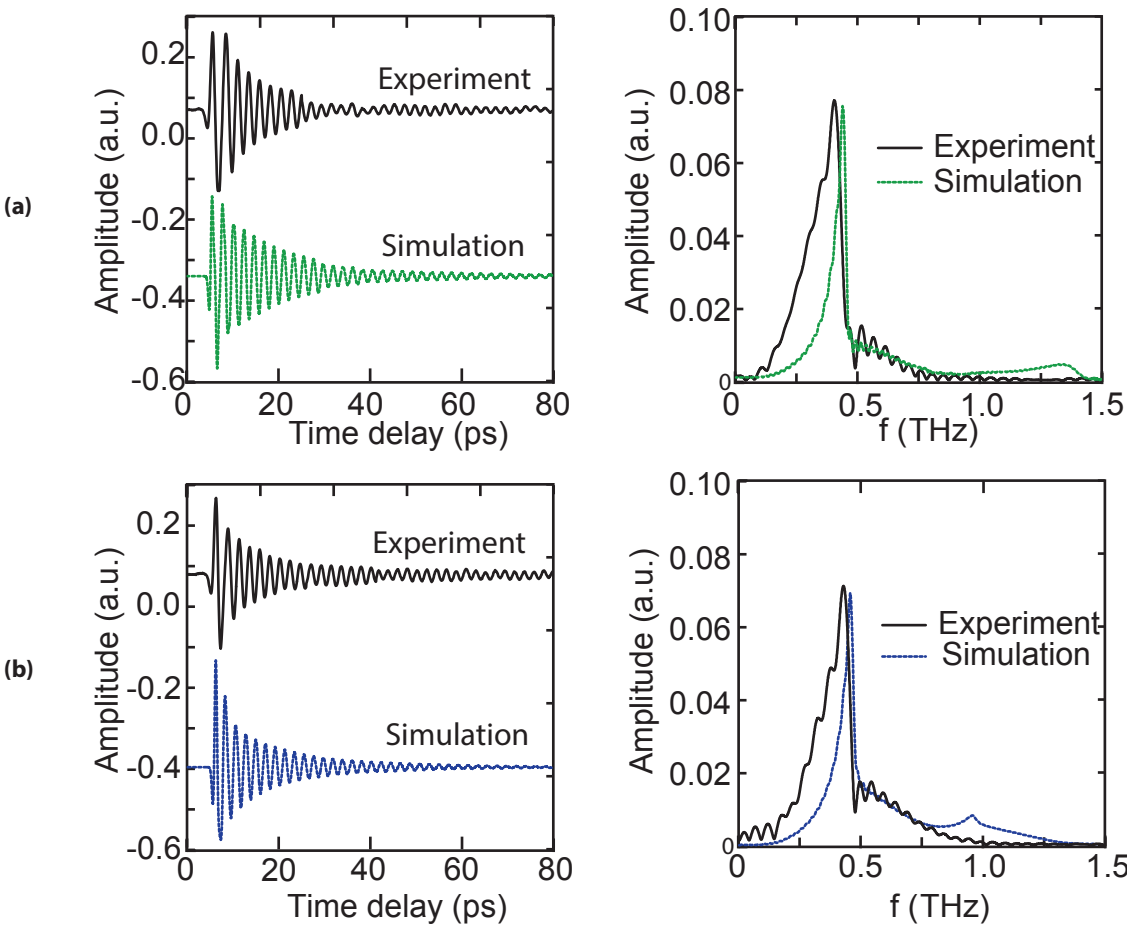

Figure 2.11: Experimentally observed and simulated time domain signal (left) and corresponding frequency domain spectra (right) for an array of troughs with dimensions (a) 500×200 μm and (b) 400×250 μm. In all cases the period was $p = 300$ μm.

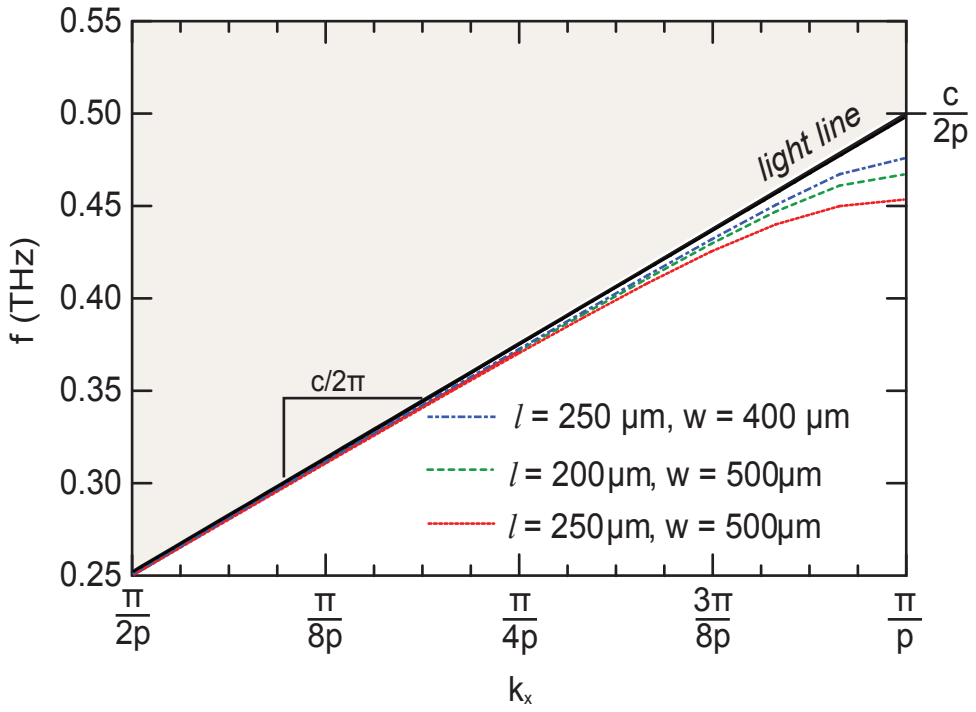

Figure 2.12: Numerically computed dispersion relation of the fundamental modes, calculated over the first Brilloun zone, for three different geometrical parameters.

responses are similar, the resonant frequencies for the fundamental mode show a slight red-shift (0.47 THz and 0.48 THz, respectively) in comparison to the that seen in Fig. 2.9, which is well confirmed by the numerical simulations.

In Fig. 2.12, we show the dispersion relations calculated numerically using a finite element eigenmode solver for the three waveguides examined experimentally in Figs. 2.9-2.11. The dispersion relation was calculated by numerically modeling one unit cell of the periodic structure, using Bloch boundary conditions along the direction of propagation and absorbing boundary conditions in the transverse directions. Perfect electrical conducting boundary conditions were assumed at the silicon

surface, as approximated for heavily doped silicon. The black solid line in the figure corresponds to the light line for plane waves propagating in vacuum. The blue, green and red curves correspond to surface electromagnetic modes supported by the periodically patterned troughs with dimensions $(w \times l) = 400 \times 250$, 500×200, and 500×250 μm, respectively. The periodicity in all the cases was held constant at p = 300 μm. Within the first Brillouin zone, the wavenumber and frequency increase monotonically, but with a reduced group and phase velocity compared to vacuum waves. The group velocity reduces to zero at the first Brillouin zone boundary ($k_x = \pi/p$), corresponding to the excitation of a confined resonant surface mode. The calculated frequency of the first Brillouin zone edge is observed to match the null-frequency seen in experiments and simulations. One can obtain the group velocity of the surface modes from the slope of the dispersion relations depicted in Fig. 2.12. The group velocity decreases with increasing depth of the trough, and approaches zero at the first Brillouin boundary.

In order to examine the dependance of the resonant frequency on the dimensions of the troughs, we carried out simulations for the various combinations of length, width and periodicity. The results are shown through a color and contour plot in Fig. 2.13. The length and width are plotted on the horizontal and vertical directions respectively, normalized relative to the period p. The resonant frequency, normalized to $c/2p$, is shown by the contours and color map. In the limit that the length of the trough is small compared to the period, the resonant frequency approaches $c/2p$ indicating that even near the Brillouin edge there is no substantial deviation from the vacuum light line. In the case when width is very large, the

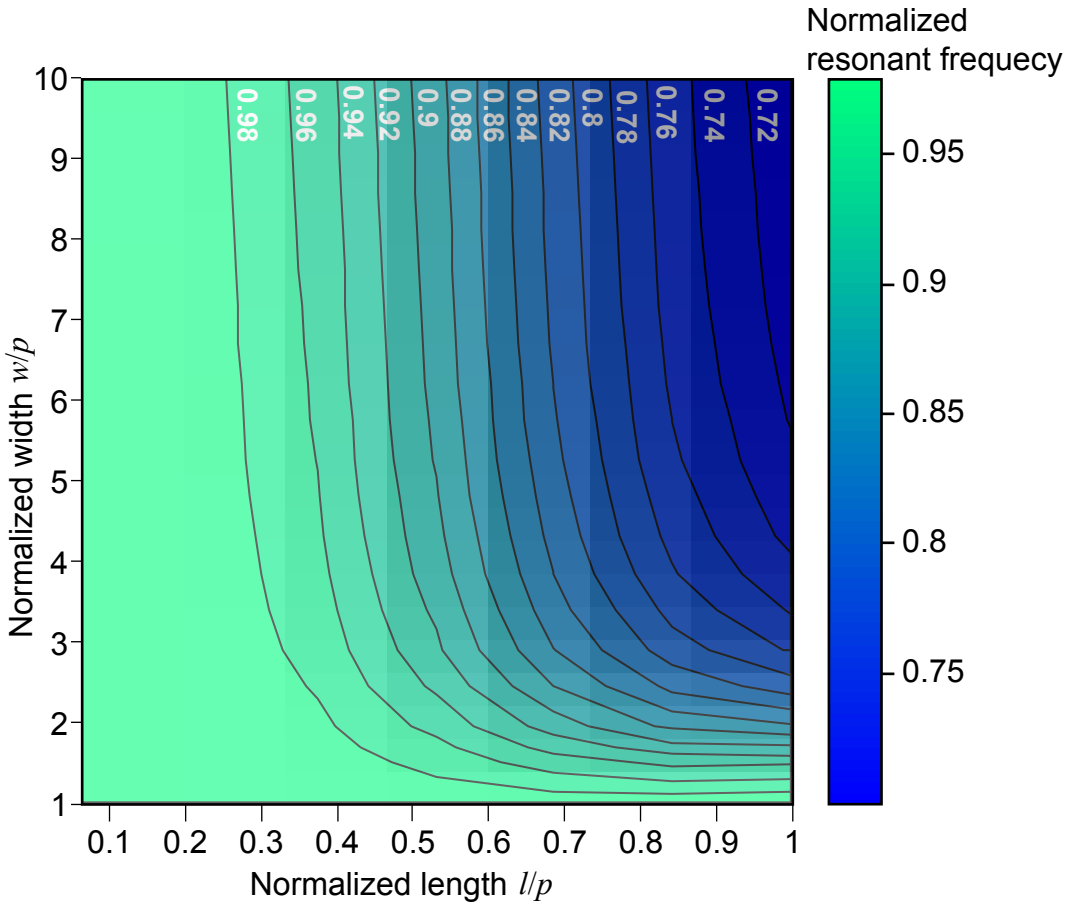

Figure 2.13: Contour plot of calculated resonant frequency (normalized to $c/2p$) as a function of the dimensions of the pyramidal trough.

resonant frequency approaches a constant value characteristic of what is expected for infinitely long (1-dimensional) V-grooves [21].

The plasmonic confinement in corrugated waveguide structures is a resonant effect with a frequency that depends on the size and shape of the pyramidal troughs. Many THz applications could benefit from further confinement in the longitudinal direction. We numerically investigated this possibility by simulating a periodic array with one dissimilar defect introduced at the center, as shown in Fig. 2.14. In this simulation the defect trough has dimensions of $(w \times l) = 500 \times 250$ μm. The experimental and simulated results presented in Fig. 2.9 suggest that these dimensions should exhibit a resonant frequency near 0.45 THz. The surrounding troughs measured 500×50 μm and formed a shallow, linear array of 6 mm length on either side of the defect. Fig. 2.14 plots the transverse electric field evaluated at the silicon surface, calculated at 0.45 THz (blue) and at the off-resonant frequency of 0.71 THz (red). As expected, when excited near the resonant frequency (0.45 THz), the plasmonic field shows significant enhancement in the defect, indicating that longitudinal confinement is possible by spatially tailoring the device dimensions. The inset to Fig. 2.14 plots the electric field profile calculated on resonance, further confirming the spatial localization of the resonant mode. It is important to mention that deeper structure can result in further confinement of the modes, however in the case examined here, depth is limited by the angle dependent etching. Therefore one needs to explore techniques of achieving waveguide structures with higher aspect ratio (depth to width ratio) in semiconductors.

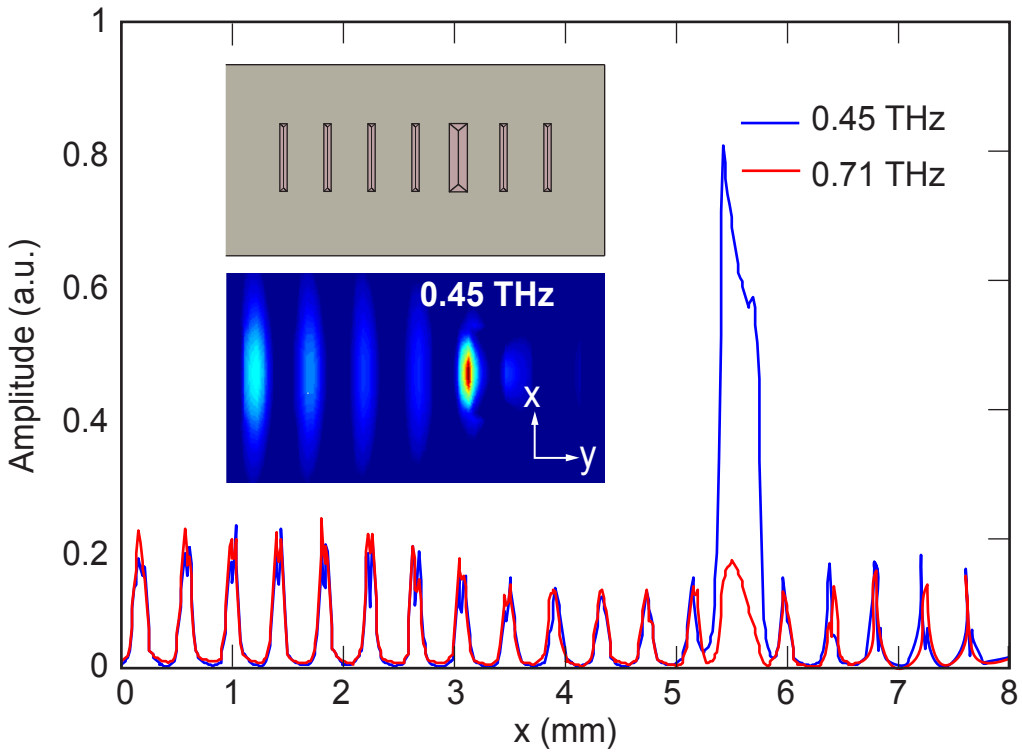

Figure 2.14: Simulated electric field amplitude for a periodic structure with a defect at the center, showing evidence of longitudinal confinement. The amplitudes are shown at the predicted resonant frequency of 0.45 THz (blue) and at the off-resonant frequency of 0.71 THz (red).

2.3 Conclusion

In this chapter, we described the analysis, theory, fabrication, and measurement of semiconductor plasmonic THz waveguides that use p^+-doped silicon as the conductive substrates that are patterned with array of grooves through anisotropic wet chemical etching. The structures are simulated using finite element methods, and measured using a terahertz time-domain spectroscopy system that was modified to sample surface fields. Measurements and simulations both show evidence of a resonant surface wave that occurs when $k_x = \pi/p$, with a reduced group velocity. The field confinement, the degree of reduction in group velocity, and the resonant frequency are related to the corrugation shape, with deeper structure producing a more pronounced effect. The study could play an important role in the developments of active and passive semiconductor devices operating at terahertz frequencies.

Chapter 3: Terahertz nonlinear conduction and absorption saturation in silicon waveguides

Among semiconductors, silicon is not only the most prevalent material in electronics, but it is also one of the most favorable dielectric materials for terahertz applications. Intrinsic silicon is transparent at wavelengths longer than 1100 nm, and has exceptionally low loss in the far infrared [1, 93, 94]. While the nonlinear properties and applications of silicon are well established in the near-infrared and mid-infrared regime [95–100], there have been very few observations of nonlinear propagation in the terahertz regime.

Silicon has band gap 1.11 eV. Its band structure is shown in Fig. 3.1. The terahertz photon energy (4.1 meV at 1 THz) is too small to produce new carriers in silicon through a 1- or 2-photon absorption, and hence the linear and nonlinear properties are caused by acceleration or heating of the existing electron (or hole) population. The traditional Drude model of conductivity Eq. 1.4 that is commonly used to describe free carrier absorption and dispersion in silicon in the terahertz regime fails to explain nonlinear wave propagation effects.

In 2010, Hebling et al. and Kaur et al. independently observed THz field induced absorption bleaching in n-doped bulk silicon, using terahertz pump-probe

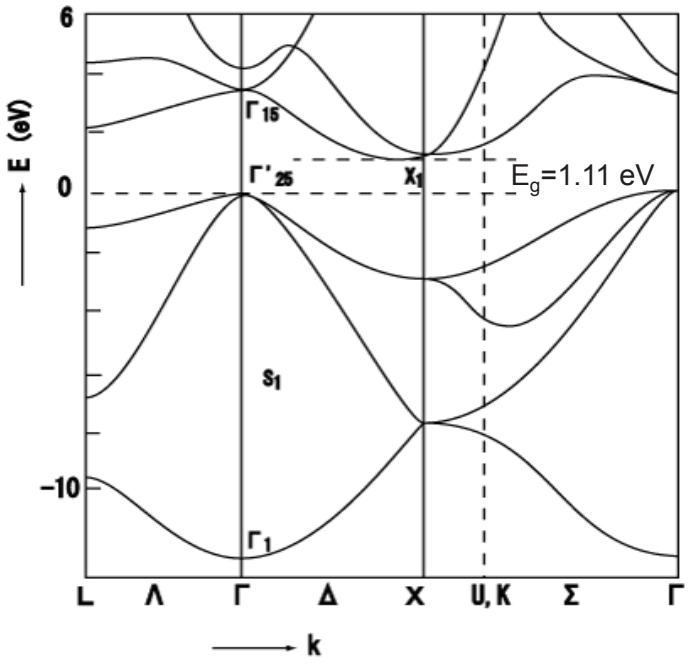

Figure 3.1: Silicon band structure(http://www2.warwick.ac.uk/fac/sci/physics/current/postgraduate/regs/mpags/ex5/bandstructure/)

measurements [3] and z-scan measurements [4]. They suggested that the effect might be explained by scattering of electrons into a higher energy (L) valley within the conduction band. More recently, Al-Naib et al. employed a two-dimensional terahertz metamaterial to enhance the nonlinearity at a silicon surface [60], and phenomenologically modeled the observations by a change in conductivity. Terahertz induced nonlinear effects have also been observed in a variety of other bulk semiconductors, including Ge [3], GaAs [48–53], GaP [54] and InSb [55–57], and numerous hot carrier effects have been offered as explanations, including intervalley scattering, band nonparabolicity, and impact ionization. In most cases, the observations were carried out using wafers or windows with optical thickness of only a few terahertz wavelengths. In such thin samples, the cumulative nonlinearity is necessarily quite small, and it is difficult to separate propagation effects from interface effects such as small changes in reflectivity, or spatial effects such as self-focusing and diffraction.

To overcome these limitations, we couple picosecond terahertz pulses into a 2 cm long silicon dielectric ridge waveguide. The waveguide greatly enhances the field concentration and nonlinear propagation length, thereby ensuring that the measured effect represents a true nonlinear wave interaction accumulated over hundreds of terahertz wavelengths, and also allows for interplay between the linear mode propagation and nonlinearity. The waveguide configuration also eliminates spatial nonlinear effects like self-focusing, enabling unambiguous measurement of the temporal nonlinear behavior. We observe over a two-fold increase in the power transmission ratio at high powers relative to low powers, depending on the carrier

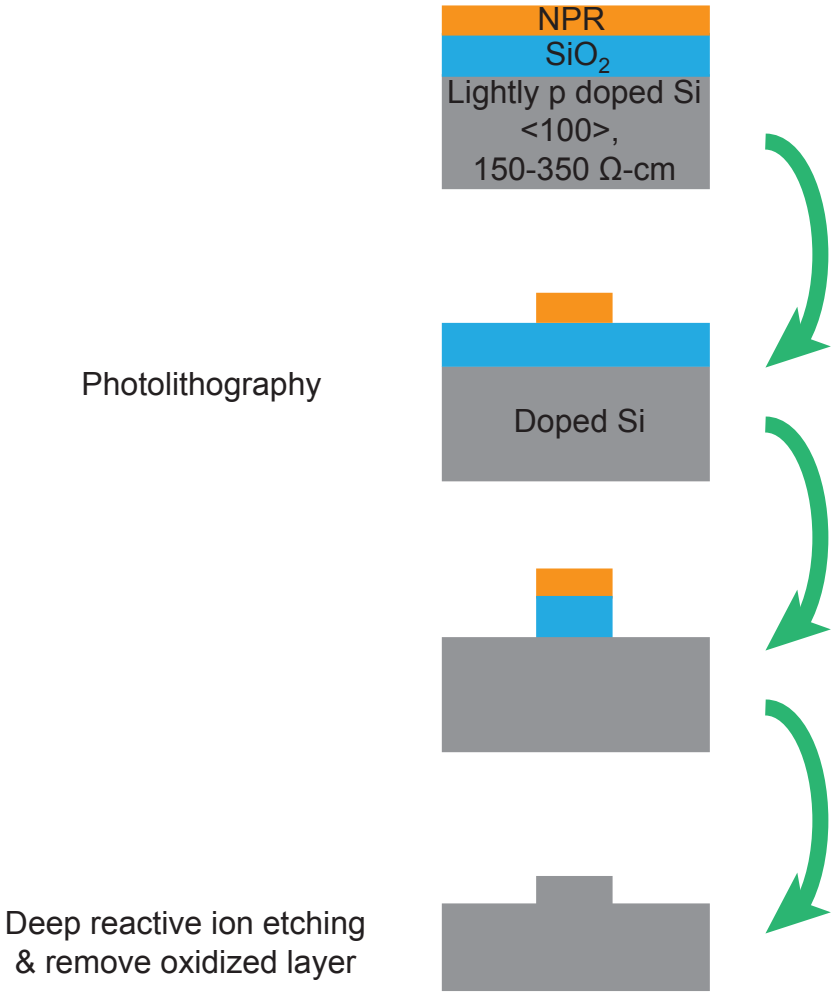

Figure 3.2: Fabrication process of ridge waveguide.

concentration, and we present a new physical and numerical model that offers an explanation of the observed behavior.

3.1 Fabrication

As shown in Fig. 3.2, the silicon ridge waveguides were fabricated from 400 μm thick, double-side polished (DSP), $\langle 100 \rangle$ silicon wafers. In order to better assess the role of carriers, we used two types of silicon: lightly p-doped wafers with a

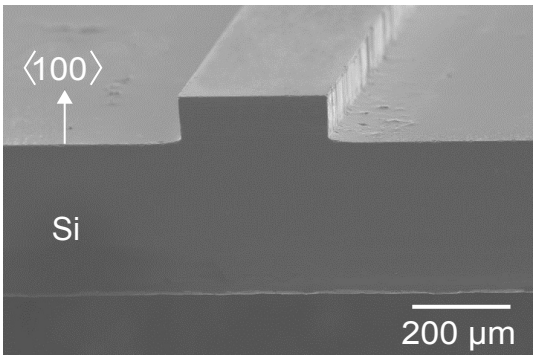

(a)

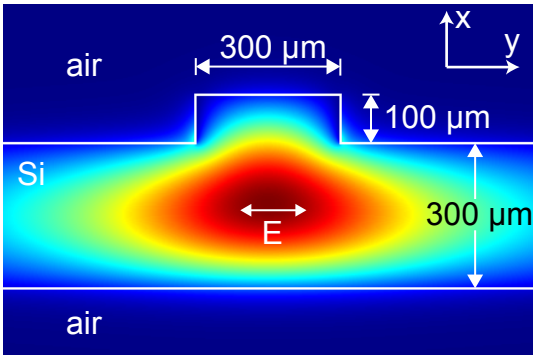

(b)

Figure 3.3: (a) Cross-sectional micrograph of fabricated silicon ridge waveguide and (b) calculated TE eigenmode at 0.5 THz.

nominal resistivity of of 150-350 Ω·cm and float-zone semi-insulating wafers with a resistivity of 10 kΩ·cm. A 1 μm sacrificial layer of SiO_2 was deposited by CVD on the wafers, and patterned using contact photolithography and reactive-ion etching to produce a 300 μm wide oxide hard-mask for subsequent etching of the waveguides. The waveguides were etched to a depth of 100 μm using pulsed deep reactive ion etching (Bosch process), after which the remaining photoresist and oxide hard mask were removed. Fig. 3.3(a) shows a cross-sectional micrograph of the completed ridge waveguide, and Fig. 3.3(b) shows the corresponding fundamental TE eigenmode of the waveguide, calculated at 0.5 THz. The transverse waveguide dimensions were chosen to ensure single-mode operation over the frequency range of interest. The waveguides were cut to a length of 2 cm using a dicing saw.

3.2 TE mode vs TM mode

The waveguide mode can be excited by terahertz polarized either along x(TM) or y(TE) direction. Fig. 3.4 displays the TE(Fig. 3.4(a)) and TM(Fig. 3.4(b)) output THz signals of our p-doped waveguide. The propagating distance is 1 cm. Fig. 3.4(b) is the result for TM mode and shows obviously higher group dispersion. In order to understand the cause of the observed pulse spreading, we used an optical eigenmode solver to compute the effective refractive index(shown in Fig. 3.5) at different frequencies for TE and TM mode of our waveguide structure. As shown in Fig. 3.5, the TM mode shows a stronger variation in group velocity compared to TE mode in the frequency range(0-1 THz) of interest, and leads to widely spread

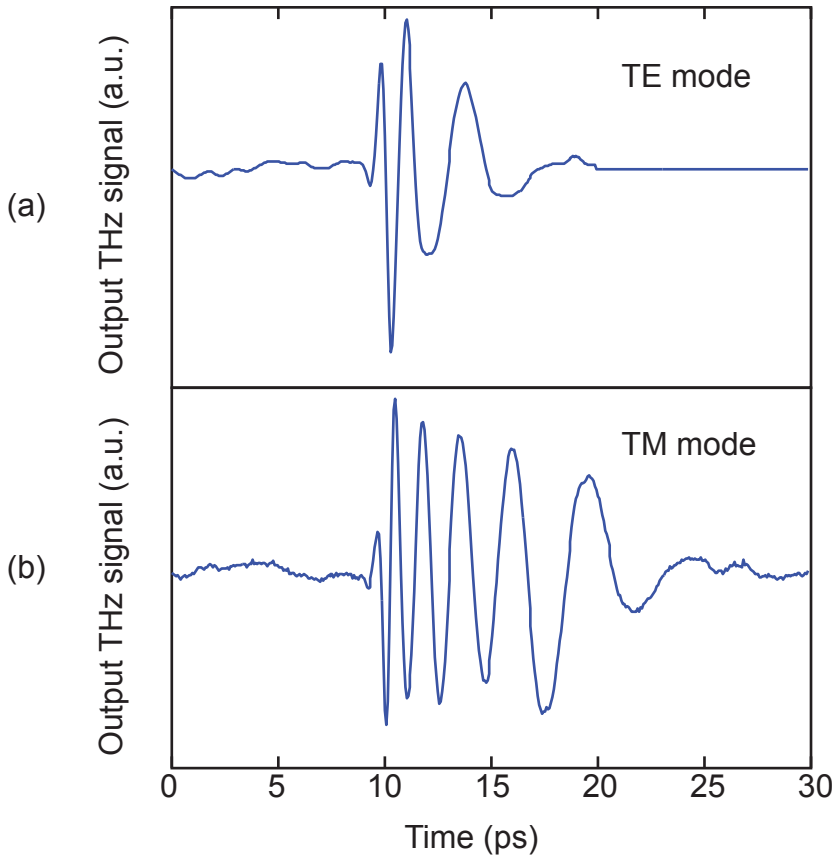

Figure 3.4: Measured output THz signals of TE(a) and TM(b) mode after 1 cm propagating distance

output signal. Because nonlinear effect is field-dependent, we prefer the THz signal to maintain tight shape and high intensity during propagation. Our measurements and simulations were therefore conducted under TE mode.

3.3 Experimental set-up and measurement

Fig. 3.6 illustrates the experimental setup used to characterize the THz nonlinear response. An amplified Ti-sapphire laser system produces 40 fs, 1 kHz repetition

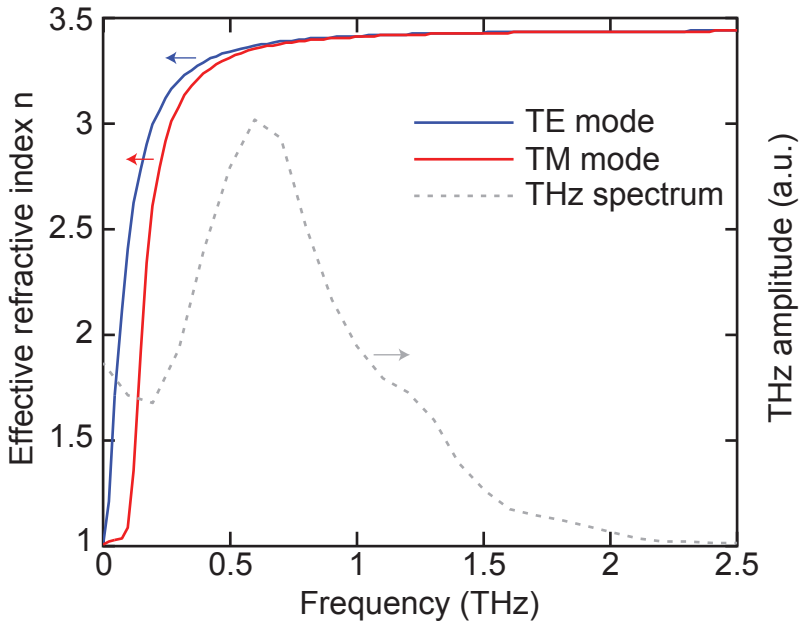

Figure 3.5: Effective refractive index for TE and TM mode of our waveguide structure.

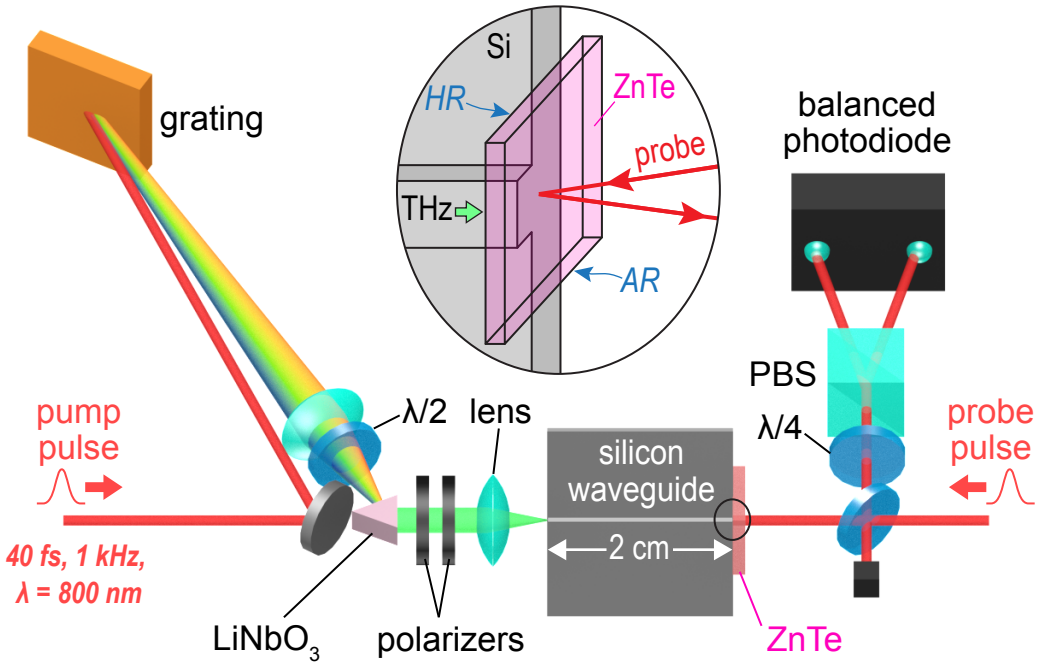

Figure 3.6: Experimental setup used to measure the THz nonlinear transmission through the silicon waveguide.

rate pulses at 800 nm center wavelength. The optical pulses are split (80:20) into pump and probe beams that are used for terahertz generation and detection, respectively. The pump pulse impinges on a grating (2000 lines/mm), producing a -1 order diffracted beam that has a tilted pulse front [42, 47, 101]. The tilted pulse was de-magnified by a factor of $2\times$ using a 60 mm focal length lens into a $LiNbO_3$ prism. A $\lambda/2$ waveplate rotates the optical beam polarization from horizontal to vertical direction to align with the optical axis of the $LiNbO_3$. The power of the THz output beam was adjusted using a pair of wire-grid polarizers, and focused using a polymethylpentene (TPX) lens onto the input waveguide facet. The THz beam was linearly polarized in the $\langle 011 \rangle$ crystallographic direction of the silicon waveguide. Using the experimentally measured energy, pulse duration, and focused spot size of the terahertz beam, the peak electric field at the focus before inserting the waveguide was estimated to be 200 kV/cm [101], of which detailed explanation will be shown in Chapter 4.

The THz pulses impinging on and emerging from the waveguides were measured using both a pyroelectric detector and electrooptic sampling. In the latter case, we used a 1 mm thick $\langle 110 \rangle$ ZnTe crystal that was coated with an 800 nm dielectric mirror front face, and antireflection coating on the rear face, which allows the probe beam to be introduced in a reflection geometry [102, 103], as shown in Fig. 3.6. The ZnTe electrooptic crystal was placed in contact with the output facet of the waveguide, to allow for near-field optical sampling of the mode emerging from the waveguide.

To measure the nonlinear transmission through the waveguide, we used the

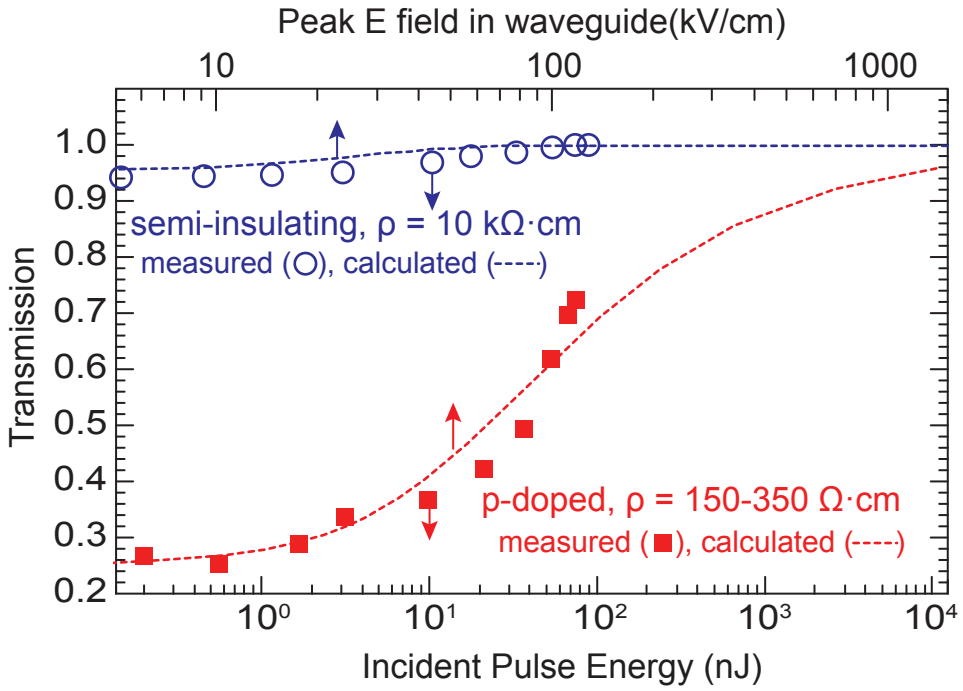

Figure 3.7: Normalized power transmission for semi-insulating (circle) and doped (square) waveguides, and corresponding calculated (dashed lines) pulse energy transmission.

Fourier transform to calculate the spectrum of the emerging waveform, and integrated the intensity spectrum to obtain a measure of the transmitted power. For the range of powers considered, the nonlinearity of the electrooptic detection process was confirmed to be negligible in comparison to the absorption saturation in the silicon waveguide.

Fig. 3.7 shows the normalized transmission ratio as a function of the input pulse energy and peak field for the two waveguides considered here. The semi-insulating silicon waveguide shows a small, but clearly measurable increase of 5%

in transmission as the pulse energy is increased from 0 to 75 nJ. The p-type silicon waveguide, by contrast, shows a more than 2-fold increase in transmission at higher fluence. The dashed lines plot the numerically calculated result (to be explained below), which shows that at sufficiently high pulse power, the power transmission ratio saturates at a level close to unity. The fact that the saturable absorption is much stronger in doped silicon clearly demonstrates the role of free carriers in the nonlinear response.

3.4 Discussion

A complete model of absorption in silicon waveguides must account for not only the field-dependent nonlinear carrier dynamics, but also the linear dispersion, which diminishes the peak field of the signal. The terahertz nonlinear wave propagation can be described by a simplified one-dimensional wave equation,

$$\left[\frac{\partial^2}{\partial z^2} - \frac{1}{c^2}\frac{\partial^2}{\partial t^2}\right] E = \mu_0 \left[\frac{\partial^2}{\partial t^2} P + \frac{\partial}{\partial t} J\right] , \tag{3.1}$$

where J is the current density (which is non-linearly related to E) and P is the linear polarization of the material, which is linearly related to the electric field in the frequency domain by:

$$\hat{P}(z,\omega) = \epsilon_0 \left[n^2(\omega) - 1\right] \hat{E}(z,\omega) , \tag{3.2}$$

where $n(\omega)$ is the effective the refractive index of the waveguide.

The propagation equation is not easy to solve as: (1) E(z,t) contains linear and nonlinear effect; (2) J(z,t) obtained from Monte Carlo or nonlinear Drude simulation changes with time and distance.

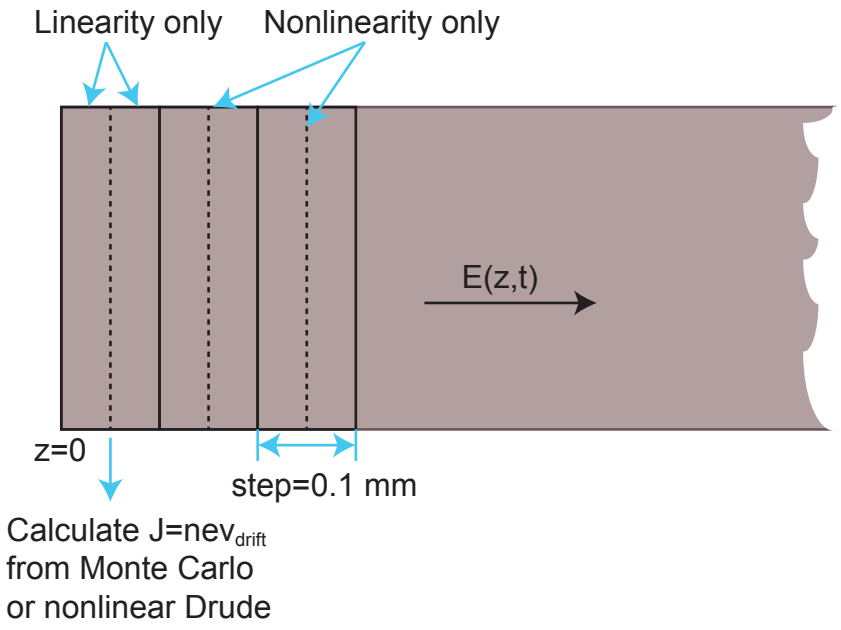

Figure 3.8: Scheme of split step method.

In order to simplify this problem, we adopted split-step Fourier method, which is a known numerical way, to solve this kind of nonlinear partial differential equation. Scheme of this method is shown in Fig. 3.8. Propagating distance is divided into several small steps. In each step, current density J, obtained from Monte Carlo or nonlinear Drude simulation at the beginning of that step, is assumed to be z independent. By treating nonlinear effect as a small perturbation to linearly propagating E field in each step, we are able to separate linear and nonlinear propagation.

Linear part: If the current is neglected, the forward traveling solution to Eq. 3.1 in the frequency domain is

$$\hat{E}(\Delta z, \omega) = \hat{E}(0, \omega) \exp\left[i\frac{\omega}{c} n(\omega) \Delta z\right] , \tag{3.3}$$

where the refractive index $n(\omega)$ incorporates material and modal dispersion of the

waveguide.

Nonlinear part: If the dispersion is neglected but the current term is retained, then the wave equation can be written as:

$$\frac{\partial^2 E}{\partial z^2} - \frac{1}{\bar{v}^2}\frac{\partial^2 E}{\partial t^2} = \mu_0 \frac{\partial J}{\partial t}\,, \tag{3.4}$$

where $\bar{v} \equiv c/n(\bar{\omega})$ represents the average velocity of the terahertz pulse, evaluated at the center frequency of the spectrum.

Combined result: Because the electric field travels in the $+z$ direction with an average velocity of $\bar{v}$, we assume that the resulting current density can be likewise cast as a function of a single argument, $J(t - z/\bar{v})$, in which case Eq. 3.4 can be integrated to find the field at the end of one step Δz:

$$E(\Delta z, t) = E(0, t - \Delta z/\bar{v}) + \frac{\bar{v}^2 \mu_0}{4} \int_{t-3\Delta z/\bar{v}}^{t-\Delta z/v} [J(t') - J(t - \Delta z/\bar{v})]\, dt' \tag{3.5}$$

The second term in Eq. 3.5 represents a perturbation ΔE in the electric field caused by the current J. The split-step numerical method replaces this accumulated nonlinearity by an equivalent lumped effect at $z = 0$, which is found by advancing Eq. 3.5 by the propagation time $\Delta z/\bar{v}$,

$$\Delta E(t) = \frac{\bar{v}^2 \mu_0}{4} \int_{t-2\Delta z/\bar{v}}^{t} [J(t') - J(t)]\, dt' \tag{3.6}$$

The nonlinear wave propagation is numerically simulated by dividing the total propagation distance into steps of size Δz, computing the linear propagation for each increment in the Fourier domain using Eq. 3.3, and incorporating the nonlinearity as lumped in the time domain using Eq. 3.6.

The nonlinear relationship between the electric field $E(t)$ and current density $J(t)$ can be described using the balance equations obtained from the Boltzmann transport equations. Although the complete Boltzmann transport equations can account for spatially-dependent heating and hot carrier diffusion in the transverse dimensions, the spreading of hot carriers is expected to be negligible for the dimensions and wavelength considered here. We therefore consider the homogeneous limit, where the momentum balance equation is [104]:

$$\frac{dv}{dt} + \Gamma_m(\varepsilon)v = \frac{qE}{m^*}\,, \tag{3.7}$$

where v represents the carrier velocity, which is directly proportional to the current density through $J = Nqv$, and $\Gamma_m(\varepsilon)$ is the momentum relaxation rate, which we take to be a function of the energy, ε.

The energy balance equation is

$$\frac{d\varepsilon}{dt} + \Gamma_\varepsilon\varepsilon = qEv\,, \tag{3.8}$$

where ε is the carrier energy relative to thermal equilibrium, and Γ_ε is the energy relaxation rate. The momentum and energy scattering rates are, in general, energy dependent, which couples these two equations. We adopt the simple, and widely used model where the energy relaxation rate Γ_ε is taken to be constant, while the momentum relaxation rate increases linearly with the carrier energy [105]:

$$\Gamma_m(\varepsilon) = \Gamma_0 + \frac{\Gamma_\varepsilon\varepsilon}{m^* v_{\mathrm{sat}}^2} \tag{3.9}$$

For sufficiently small carrier energy, the second term in Eq. 3.9 may be neglected, in which case Eq. 3.7 can be solved directly to give the familiar linear Drude rela-

tionship between v and E, in the frequency domain,

$$\hat{v}(\omega) = \frac{\mu}{1 - i\omega/\Gamma_0}\hat{E}(\omega)\,, \tag{3.10}$$

where $\mu \equiv q/m^*\Gamma_0$ is the low-field mobility. However, for sufficiently high fields, Eqs. 3.7-3.9 predict well-known nonlinear transport phenomena including the saturation(Fig. 3.9(a)) and overshoot(Fig. 3.9(b)) of carrier velocity at $v = v_{\rm sat}$ with increasing DC field strength. The electron and hole saturation velocities in silicon are approximately $v_{\rm sat} \sim 10^7$ cm/s, and the corresponding critical electric field strength above which saturation effects become important is $E_{\rm cr} = v_{\rm sat}/\mu \sim 7$ kV/cm (for electrons), 16 kV/cm (for holes) – conditions that are readily achieved for the terahertz pulses used in these experiments. A similar transition from ballistic to drift dynamics has been observed in photoexcited GaAs wafers for strong terahertz pulses. [53].

We used the split-step numerical method described above, together with the nonlinear Drude relations described in Eqs. 3.7-3.9 to calculate the power-dependent transmission as a function of input power for the two waveguides under consideration. For the p-doped silicon sample, we assumed a carrier concentration of $N = 8.5 \times 10^{13}$ cm^{-3}, a low-field hole mobility of $\mu = 470$ cm^2/(V·s), a hole effective mass of $m^* = 0.36\,m_0$, and a saturation velocity of 0.75×10^7 cm/s. For the high-resistivity float-zone silicon, we estimated a residual electron concentration of $N = 5 \times 10^{11}$ cm^{-3} and a low-field electron mobility of $\mu = 1,416$ cm^2/(V·s), effective mass of $m^* = 0.26\,m_0$, and an electron saturation velocity of 10^7 cm/s.

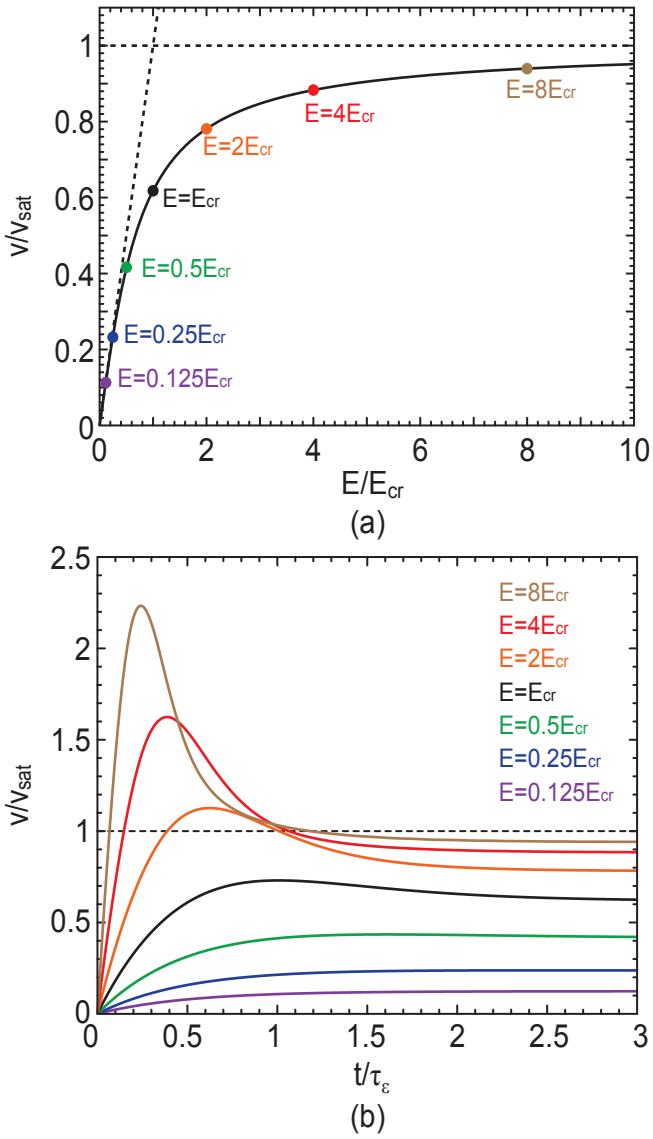

Figure 3.9: (a)Average drift velocity versus applied DC field. (b)Drift velocity step response to an electric field that is turned on at t=0.

In both cases the energy relaxation rate was taken to be $1/\Gamma_\varepsilon = 0.2$ ps. We used accepted physical parameters from the literature, and the only adjustable parameter in the calculation was the carrier concentration N, which was chosen to both match the resistivity range of the wafers and to also agree with the observed absorption in the low-field limit. The calculations were performed using 100 μm steps and a temporal window of 80 ps divided into 4000 steps. For the numerical calculations, the input THz waveform was taken to be of the form $E(t) = E_0 \cos(at - b)e^{-ct^2}$ where the constants a, b and c were chosen to best match the actual measured input waveform. The input coupling to the waveguide was estimated by projecting the Gaussian input beam onto the frequency-dependent computed eigenmode of the waveguide. The dashed lines in Fig. 3.7 show the calculated pulse energy transmission as a function of the input power and peak field, and agree well with the experimental measurements. In optical materials saturable absorption is often described by a factor $1/(1 + I/I_{sat})$, which can be derived from a simple two-level population model. While this phenomenological treatment can, by proper choice of I_{sat}, also match the observations in Fig. 3.7, it does not reduce to the conventional Drude model in the low-intensity limit and it fails to predict well-known nonlinear transport phenonemena such as velocity saturation in the limit of static fields.

Fig. 3.10 shows a numerical simulation of how the terahertz pulse evolves in time as it traverses the 2 cm long lightly p-doped silicon waveguide. The left portion was calculated using the conventional Drude model while the right portion includes the nonlinear split-step model discussed here, assuming a peak-peak input field of 100 kV/cm, clearly showing the enhanced field transmission.

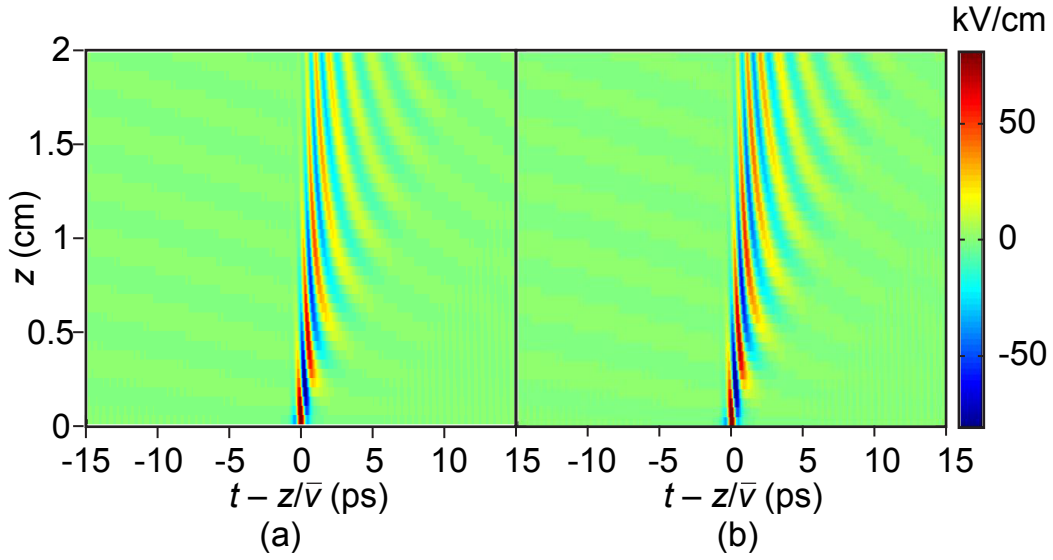

Figure 3.10: Evolution of the temporal profile of terahertz pulse along the p-doped waveguide obtained from (a)conventional Drude model and (b)nonlinear split-step simulation

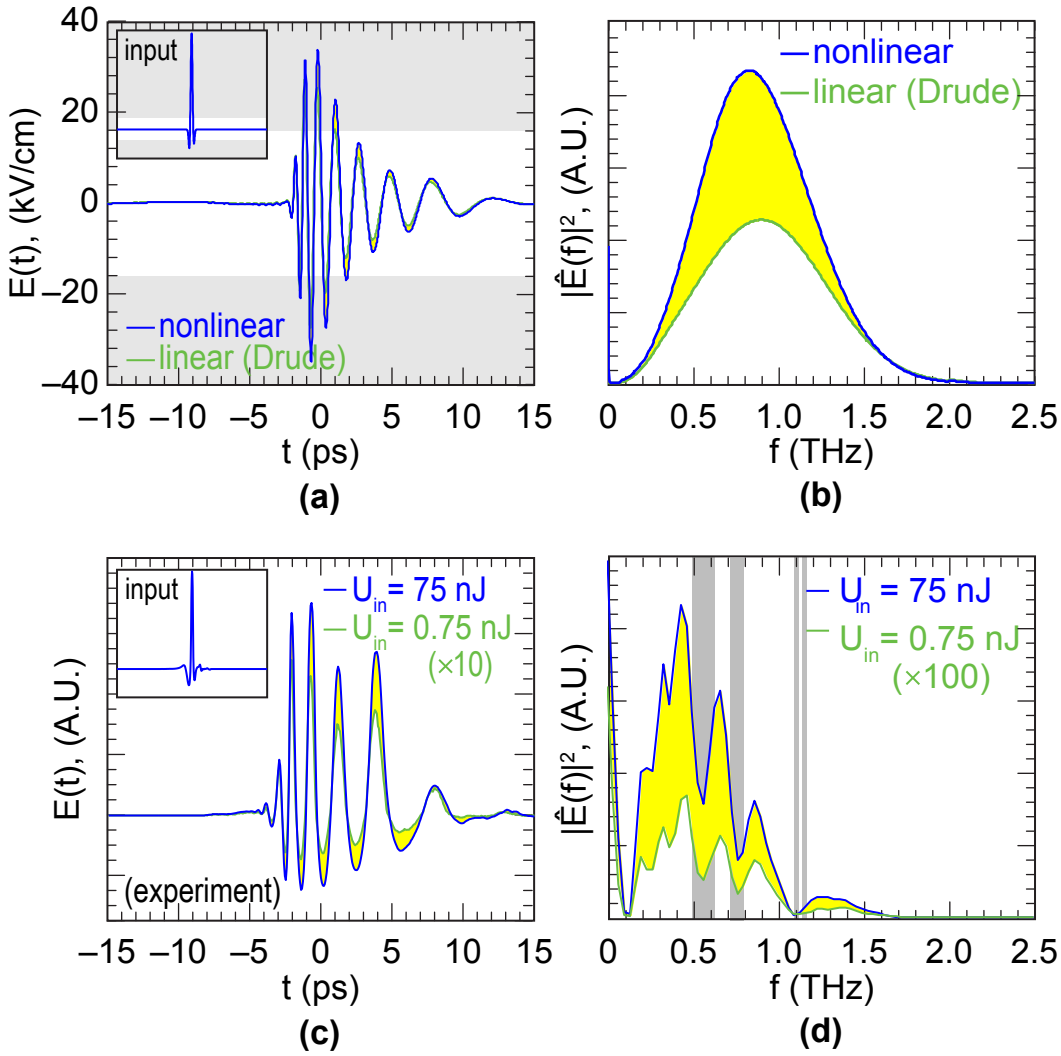

Figure 3.11: (a) Transmitted terahertz waveform, calculated using Monte Carlo simulation of carrier dynamics together with the split-step Fourier method. The linear (green) output curve was calculated using the conventional linear Drude model and waveguide dispersion, and shows lower transmission. Inset: the simulated input pulse, with a peak-peak field of 100 kV/cm. (b) Transmitted power spectrum, calculated with (blue) and without (green) nonlinearity. (c) Experimentally measured transmitted terahertz waveform for 75 nJ (blue) and 0.75 nJ (green) incident pulse energy. The green field was scaled by 10× to account for the 100× lower energy. (d) Experimentally measured power spectra for 75 nJ (blue) and 0.75 nJ (green) incident pulse energy. The green curve was scaled by 100× to account for the lower energy. Gray bands are additional losses caused by water absorption.

The balance equations Eqs. 3.7-3.9 provide a simple and efficient model of the nonlinear transport in silicon, but there are alternative models used to explain the energy-dependent relaxation rates. The most accurate and widely accepted approach is to use the Monte Carlo method to directly simulate the Boltzmann transport equations in the time domain [106–108]. To better resolve the physical origins of the nonlinearity, we used the same split-step Fourier method to compute the nonlinear propagation, but instead of Eqs. 3.7-3.9, the current density at each step was estimated using time-dependent Monte Carlo simulations of an ensemble of 10,000 carriers. This method is far more computationally intensive, and we therefore divided the waveguide into only 20 steps and simulated propagation for an input pulse with peak-peak field of 100 kV/cm. The same enhancement of transmission is observed (Fig. 3.11).

The Monte Carlo calculations incorporate several physical effects that contribute to the observed response, including band non-parabolicity, Coulomb scattering, intravalley acoustic phonon scattering, and equivalent intervalley optical phonon scattering. Of these, simulations revealed that intravalley and equivalent intervalley phonon scattering were found to be the dominant factors that contribute to the nonlinearity in the simulated response. In the Monte Carlo simulation, impact ionization is not included as THz field of interest is not strong enough to cause this phenomenon. And notably, higher energy L-X intervalley scattering does not play a significant role, as had been previously suggested.

Fig. 3.11(a)-(b) show the calculated output waveform and spectra, obtained using a combination of the Monte Carlo simulation with split step Fourier method,

for the highest input field (100 kV/cm) that was considered in the p-doped waveguide. The input pulse shape is obtained from experimentally measured results. For comparison we also show the field obtained from the conventional (linear) Drude model, which would predict a higher carrier velocity and lower output field. Media 1 provides an animation showing how the nonlinearity and dispersion accumulate as the pulse traverses waveguide.

Fig. 3.11(c)-(d) show the corresponding experimental measurements of the output terahertz waveforms and spectra, which show a similar increase in relative transmission at high fields. To assess the role of nonlinearity, we attenuated the input power by a factor of 100× and repeated the measurement of the output waveform. The green linear curve shown in Fig. 3.11(c)-(d) was then scaled by a factor of 10 or 100 to provide a direct comparison with the field and power (respectively) measured at higher power. The experimental spectra show additional loss that is caused by strong water absorption(details can be found in Fig. 3.12) at 0.55, 0.75 and 1.1 THz that was not included in the simulations, indicated by the gray bands in Fig. 3.11(d). These features also contribute to the discrepancy in the time-domain traces shown in Fig. 3.11(a) and (c). More precise matching of the temporal waveforms and spectral shape would require accurate determination of the frequency-dependent input coupling of the waveguide, as well as the atmospheric attenuation of the terahertz pulse—factors that were impossible to measure in our experiment. While the pulse shape and spectrum are determined by the linear dispersion and absorption, the nonlinear Drude absorption serves primarily to reduce the transmitted field amplitude at higher power. Notably, the measurements show

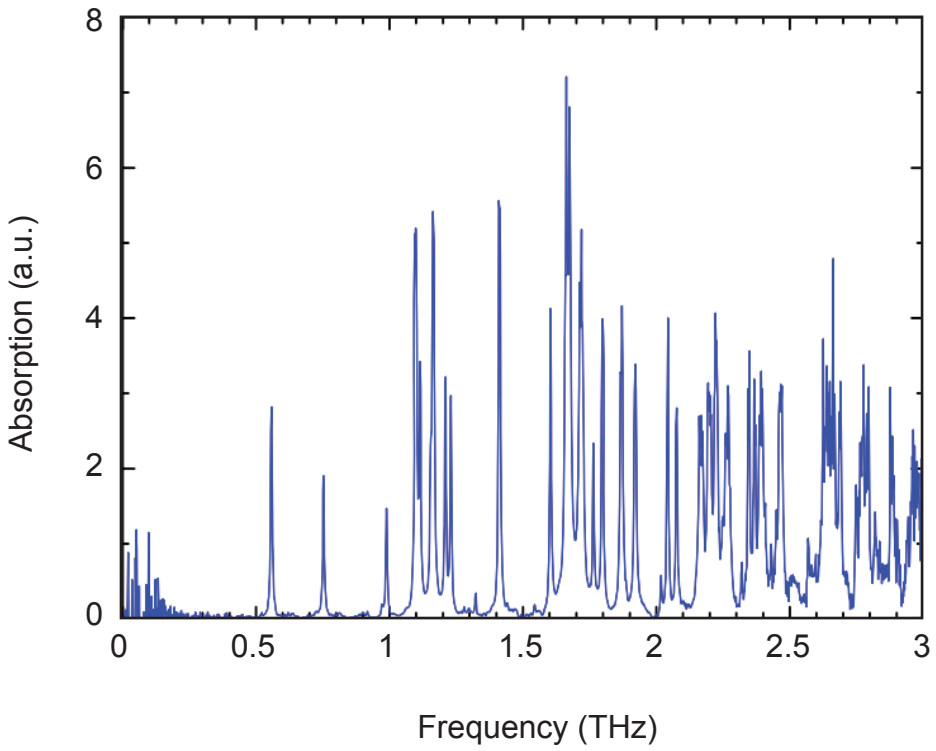

Figure 3.12: Atmospheric terahertz water absorption lines obtained by NPL(`http://www.npl.co.uk/upload/pdf/naftaly.pdf`)

that the relative transmission is significantly higher for strong terahertz pulses, and the degree of absorption saturation is comparable to that shown in Fig. 3.11(b).

A direct comparison of TE mode output signal from Monte Carlo and Balance Equation with same input signal (100 kV/cm) for the p-doped waveguide is shown in Fig. 3.13. Parameters used for the p-doped sample are E_{cr}=16 kV/cm, mobility μ=470 $cm^2/(V{\cdot}s)$, effective mass m^*=0.36 m_0, and doping density N=8.5 $\times$ 10^{13} cm^{-3}. From Fig. 3.13, we can see results from balance equation agree very well with that from Monte Carlo even after 2 cm propagation distance in p-doped waveguide. We also show the linear result calculated from linear Drude equation assembled

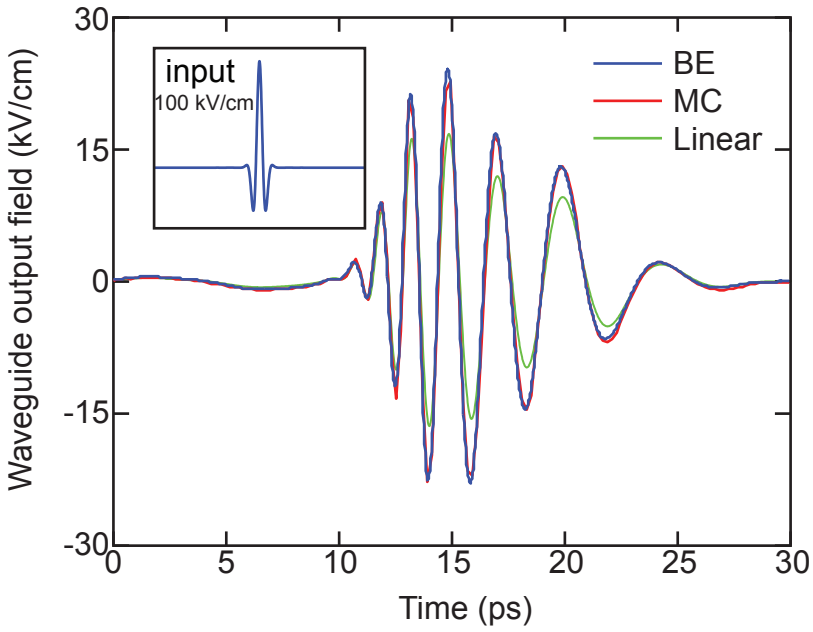

Figure 3.13: TE mode results from Monte Carlo simulation(red), balance equation(blue, and linear Drude model(green) with same input 100 kV/cm signal after 2 cm propagation distance.

with wave equation in this plot. Monte Carlo and balance equation both lead to enhancement of the transmission phenomenon.

3.5 Conclusion

In conclusion, we experimentally explore the phenomenon of absorption saturation in silicon dielectric waveguides at terahertz frequencies. The field-induced transparency and associated carrier velocity saturation is shown to be dynamical effect that cannot be adequately explained by a modified effective mobility or Drude model. We present a simple, nonlinear Drude model that supports the observations, and we confirm the model using rigorous Monte Carlo simulations. Further,

we introduce a numerical split-step method that models the interplay of nonlinearity and dispersion in the wave propagation. These results could have important consequences in future high-power terahertz guided-wave nonlinear devices, such as terahertz frequency converters, parametric oscillators, mixers, and modulators.

Chapter 4: Details about nonlinear THz propagation simulation

In chapter 3, we briefly introduced estimation of THz field and Monte Carlo simulation. Here, we will describe details about those theories and methods.

4.1 Estimation of terahertz field entering silicon waveguide

In our experiment, we used two ways to measure the THz signals. Pyroelectric detector can provide us the information of THz power, and we can obtain the amplitude and spectrum of our THz signal from EO sampling. For intense THz pulses, attenuation is required prior to EO sampling to avoid nonlinearity in the EO detection process. Both measurements do not give us the direct knowledge of input THz field amplitude needed by nonlinear propagation study.

During past years, many research groups tried to calibrate their THz field amplitude from these indirect measurements. Currently, there are 2 commonly used methods: (1)electro-optic sampling [43] and (2) intensity measurement [101].

4.1.1 Electro-optic sampling

Electro-optic(EO) sampling(Fig. 4.1) is an optoelectronic technique of optical sampling that exploits the linear Pockels effect. It measures the actual THz pulses

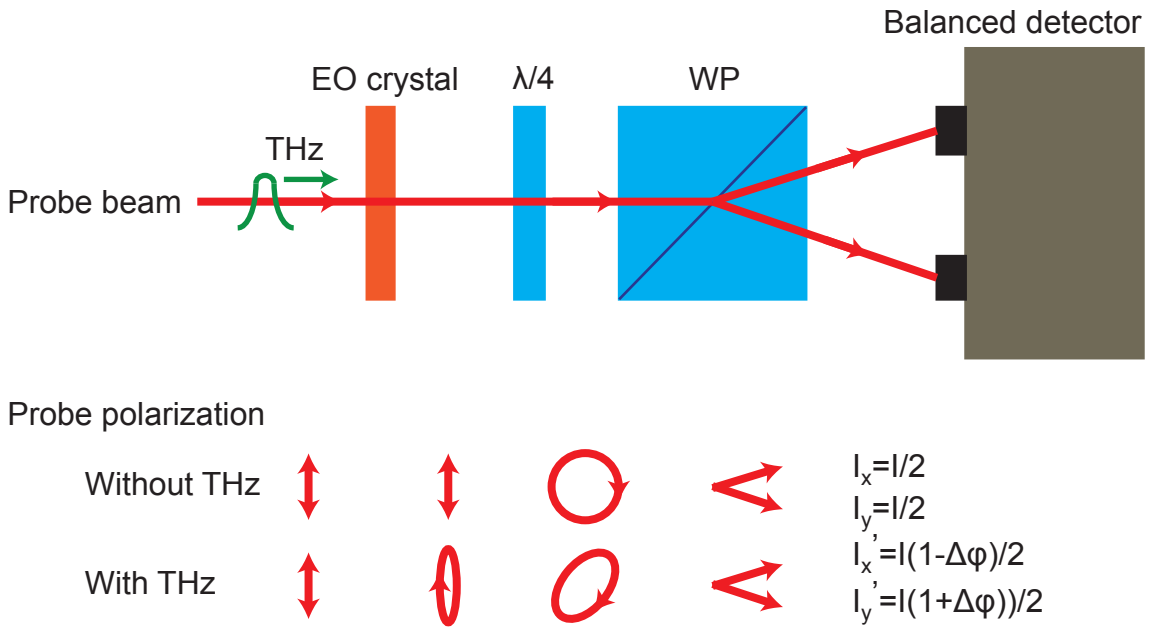

Figure 4.1: Schematic of THz Electro-Optic sampling

in the time domain. In EO sampling, THz and probe laser beam co-propagate in the electro-optic crystals, such as ZnTe or GaP. The existance of the THz field changes the birefringence of the EO crystal and causes the refractive index difference for polarizations along different axes of the crystal. The polarization of probe beam(with intensity I) is modulated by this birefringence change. This polarization change is converted to intensity change $\Delta I = I_y^{'} - I_x^{'}$ between the beams emerging from the Wollaston prism and polarization beam-splitter. A pair of balanced photodiodes is used to suppress the common laser noise while the signal is doubled.

For high enough power, the THz induced phase delay coming from the refractive change is no longer in the linear region. In order to attenuate THz, people often use several high-resistivity silicon wafers to reflect most power of THz. After attenuation, the linear EO signal $\Delta I/I$ measured by balanced photodetectors is related

to electric field amplitude E_{THz} by the formula:

$$\sin^{-1}(\Delta I/I) = \frac{2\pi n_0^3 r_{41} t_{ZnTe} t_{Si}^5 E_{THz} L}{\lambda_0}, \tag{4.1}$$

in which center wavelength λ_0 is 800 nm, $n_0 = 2.85$ is refractive index for ZnTe detection crystal at 800 nm, r_{41} =4 pm/V is ZnTe EO coefficient, L is the thickness of EO crystal, and $t_{ZnTe} = 0.48$ and $t_{Si} = 0.7$ are Fresnel transmission coefficient for ZnTe surface and Si wafer used to attenuate THz field. From Eq. 4.1, we can calculate without silicon wafer, the E-field needed to produce a $pi/2$(quarter-wave) birefringence is 45 kV/cm for 1 mm ZnTe.

4.1.2 Relation between intensity and E field

For a monochromatic propagating wave, such as a plane wave or a Gaussian beam, the local intensity is related to the amplitude E of the electric field via:

$$I = \frac{P}{A} = \frac{cn\epsilon_0}{2}|E_{THz}|^2. \tag{4.2}$$

A is the area. P is the THz peak power. Our average THz power is 110 μW. The repetition rate of our laser system is 1 kHz. And pulse duration measured by EO sampling is 1 ps. Hence, the real peak power of our pulsed teraherze wave was:

$$\begin{aligned} P &= (110 \times 10^{-6} W) \times \frac{1/\text{repetition rate}}{\text{pulse duration}} \\ &= (110 \times 10^{-6} W) \times \frac{1 \text{ ms}}{1 \text{ ps}} \\ &= 1.1 \times 10^5 \text{ W}. \end{aligned} \tag{4.3}$$

The spot size(FWHM) of focused terahertz beam measured by bolometer camera is 0.5 mm(diameter). Before entering the waveguide, electrical field is (refractive

index=1 for air):

$$|E_{THz}| = \sqrt{\frac{2P}{Area \times cn\epsilon_0}} = 205 \text{ kV/cm}. \tag{4.4}$$

4.1.3 Input coupling efficiency

When terahertz is coupled into silicon ridge waveguide from air, it experiences coupling loss at the input facet. This loss comes from two parts: reflection and mode matching.

4.1.3.1 Reflection loss

This loss arises from the discontinuity of refractive index at the input facet. Using field transmission formula for plane wave normal incidence, we can estimate the transmitted field is:

$$E_{trans} = E_{in}\frac{2n_{air}}{n_{Si} + n_{air}} = 0.45E_{in}. \tag{4.5}$$

We could also calculate electrical field inside waveguide by using power transmission formula, which represents as:

$$P_{trans} = P_{in} \times (1 - \left|\frac{n_{air} - n_{Si}}{n_{air} + n_{Si}}\right|^2) = 0.702P_{in}. \tag{4.6}$$

And by estimating the confined area of terahertz under the ridge to be 300×400 μm^2, we obtain the field from(refractive index n=3.4):

$$|E_{THz}| = \sqrt{\frac{2P_{trans}}{Acn\epsilon_0}} = 119 \text{ kV/cm}. \tag{4.7}$$

4.1.3.2 Mode matching loss

The reflection loss introduced above is good enough to estimate coupling efficiency of bulk sample. However, as our sample is a ridge waveguide, the coupling efficiency also depends on the overlap integral of Gaussian mode of the input THz beam and the fundamental mode of the waveguide.

The time domain THz field can be represented by:

$$E(x,y,z,t) = \frac{1}{2\pi}\int \hat{E}(\omega)\Phi(x,y,\omega)e^{i[\beta(\omega)z-\omega t]}d\omega \tag{4.8}$$

where $\Phi(x,y,\omega)$ is the eigenmode of the waveguide at frequency ω, z is the propagation direction. By assuming the $\Phi(x,y,\omega)$ is normalized to have a value of 1 at the measurement position (x_0,y_0) $\hat{E}(\omega)$ and its Fourier transform E(t) represent the on-axis electric field at the input of the waveguide:

$$E(x_0,y_0,z=0,t) = \frac{1}{2\pi}\int \hat{E}(\omega)e^{-i\omega t}d\omega = E(t). \tag{4.9}$$

By taking the Fourier transform of Eq. 4.8, at z =0, we find the equivalent frequency domain expression for the input electric field in the waveguide:

$$E(x,y,z=0,\omega) = \hat{E}(\omega)\Phi(x,y,\omega). \tag{4.10}$$

Using the same expansion to describe the Gaussian beam that is incident on the waveguide, we get:

$$E_{in}(x,y,z=0,\omega) = \hat{E}_{in}(\omega)\Phi_{in}(x,y,\omega), \tag{4.11}$$

where $\hat{E}_{in}(\omega)$ is the Fourier transform of the input THz waveform measured at (x_0,y_0). We assume $\Phi_{in}(x,y,\omega)$ is Gaussian beam with waist w and normalized to

have peak value of 1 at (x_0,y_0).

$$\Phi_{in}(x,y) = \exp\left(-\frac{(x-x_0)^2+(y-y_0)^2}{w^2}\right) \tag{4.12}$$

Now we can calculate the $\hat{E}(\omega)$ by a simple projection operation:

$$\hat{E}(\omega) = \frac{\int \Phi^*(x,y,\omega)\Phi_{in}(x,y)dxdy}{\int |\Phi(x,y,\omega)|^2 dxdy}\hat{E}_{in}(\omega). \tag{4.13}$$

For w=200 μm input Gaussian beam, the coupling coefficient at different frequency of our waveguide is calculated from Eq. 4.13 and plotted in Fig. 4.2, which indicates the coupling works as a high-pass filter. One thing to mention is we are not computing the power-coupling, but the peak on-axis electrica field coupling. This is what is modeled and also what is measured.

4.2 THz Monte Carlo simulation

As discussed in Chapter 1, high THz field induced transparency was observed in n-type bulk semiconductors including GaAs, Ge, and Si. Several theories were suggested for this phenomenon, such as intervalley scattering and nonparabolicity of the conduction band valleys. However more rigorous theory and simulation are needed to study the underlying physics.

Carriers' statistical behavior in semiconductors can be described by Boltzmann Transport Equation(BTE) [106]:

$$\frac{\partial f}{\partial t} + \mathbf{v} \times \nabla_r f + \mathrm{F} \times \nabla_p f = \frac{\partial f}{\partial t}|_{scatt}. \tag{4.14}$$

The first item is probability density function $f(\mathrm{r},\mathrm{p},t)$ changes with time. The second comes from diffusion. v is the carrier velocity. The third represents drift. F

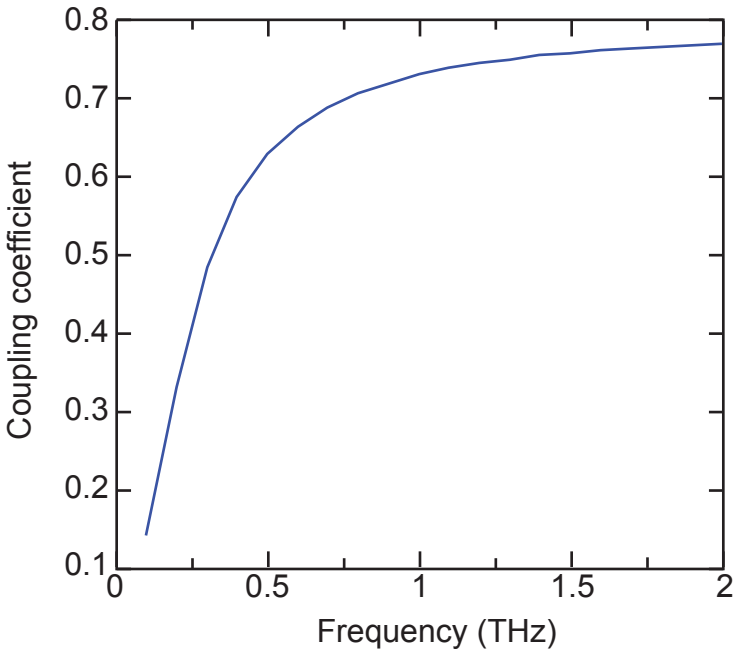

Figure 4.2: Input coupling coefficient at different frequency for the silicon ridge waveguide shown in Chapter 3 with input Gaussian beam width 200 μm.

is the force applied on the carrier. The term on the right side accounts for carrier scattering. The BTE enables us to calculate position and momentum versus time for each carrier inside silicon.

The BTE is usually very difficult to solve. It's much easier to simulate the trajectories of individual carriers as they move in semiconductors under the influence of electric fields and random scattering forces. Monte Carlo is such a simulation method, and provides the most accurate simulation results for studying transport by tracking a large amount of carriers through time. We adopted the Monte Carlo process [109]. The flowchart of our Monte Carlo simulation is shown in Fig. 4.3.

4.2.1 Initialization

First, we read in all related parameters such as effective mass m^*, nonparabolicity factor α, lattice temperature T, doping density n, terahertz field E_{THz} and time step Δt. Silicon material parameters used are listed in Table. 4.1. We note that typically simulation of holes in silicon is more complicated than electrons. The valance band consists 3 bands at $\vec{k} = 0$: heavy band, light band, and split-off band. In previous Monte Carlo calculations, the simplest way people reported to describe valance band is to use one band model [110]. Here for simplicity, we adopt an one band nonparabolic model as used for conduction band.

We calculated the 10,000 carriers' initial energy and k distribution(Fig. 4.4) from Maxwellian Boltzmann distribution equations:

$$E = \pm\frac{3}{2}k_B T \ln\left(\frac{1}{r}\right), r \text{ is chosen randomly between 0 to1 for each carrier,} \quad (4.15)$$

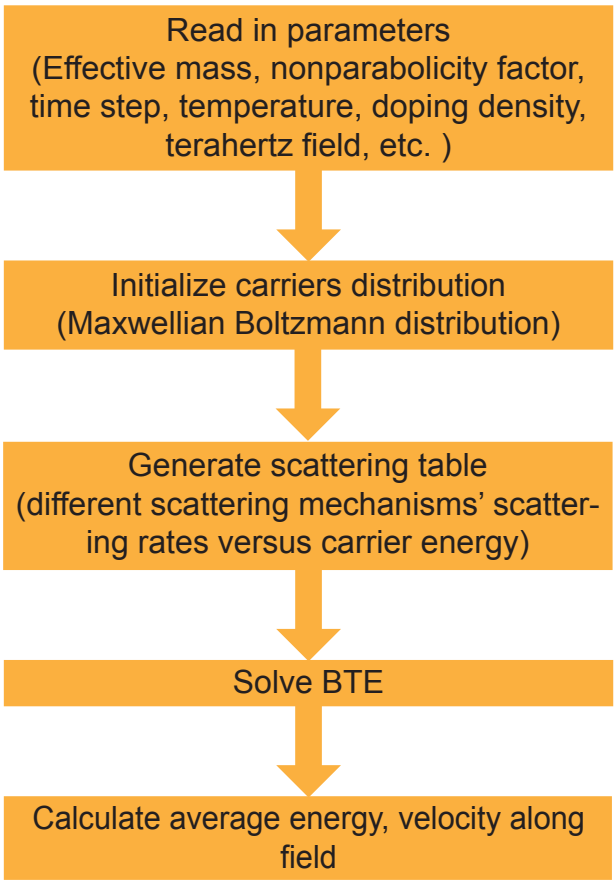

Figure 4.3: Flowchart of Monte Carlo simulation

Table 4.1: Silicon material parameters

Lattice constant(Angstroms)	5.43
Density(g/cm^3)	2.329
Sound velocity(m/s)	9040
Relative Dielectric Constant	10.92
Electron effective mass	$0.26m_0$
Hole effective mass	$0.36m_0$
Electron acoustic deformation potential(eV)	9.5
Hole acoustic deformation potential(eV)	5
Optical phonon energy (eV)	0.063

$$\alpha = \frac{(1-\frac{m^*}{m_0})^2}{E_{gap}}, \; E_{gap} \text{ is energy gap between conduction and valence band.} \quad (4.16)$$

$$k = \sqrt{\pm\frac{2m(E \pm \alpha E^2)}{\hbar^2}}, \quad (4.17)$$

$$\left.\begin{aligned} k_x &= k\sqrt{1-(1-2r)^2}\cos(2\pi r) \\ k_y &= k\sqrt{1-(1-2r)^2}\sin(2\pi r) \\ k_z &= k(1-2r) \end{aligned}\right\} 0 \le r \le 1 \quad (4.18)$$

in which, + for electron, - for hole. E is initial carrier energy. k_B is Boltzmann constant. T represents temperature. α is nonparabolicity factor for silicon. m^* is effective mass. $\hbar$ is Planck constant. k is initial wavevector. r is a random number

uniformly distributed from zero to one. Distribution of k along x, y, z directions is calculated from Eq. 4.18.

Then we generate scattering table for different scattering mechanisms. In our Monte Carlo simulation, scattering mechanisms considered are acoustic phonon scattering, equivalent intervalley scattering, intravalley optical phonon scattering, and Coulomb scattering. Impact ionization is not included here as field of interest is not strong enough to induce this phenomenon for the experimental conditions considered here.

Acoustic phonon scattering: It is carrier-lattice interaction. The carrier exchanges energy with an acoustic mode of the vibration of atoms in the crystal lattice.

Equivalent intervalley phonon scattering: This type of scattering accounts for the charge carrier transition from initial states to final states which belong to different but equivalent valleys. For conduction band, silicon has six equivalent valleys located at $\langle 100 \rangle$ axes. Two types of intervalley scattering are possible in Si; 'g-type' processes move a carrier from a given valley to one on the opposite side of the same axis. The 'f-type' processes move a carrier to one of the remaining valleys.

Intravalley phonon scattering accounts for carriers' transition within the same valley, i.e., carrier resides in the same valley before and after scattering. The phonons involved are those with wave vectors near the center of Brillouin zone.

Coulomb scattering rises from carrier-carrier interaction and reflects the electrostatic forces between charge carriers.

In our simulation, acoustic, intervalley and intravalley scattering are consid-

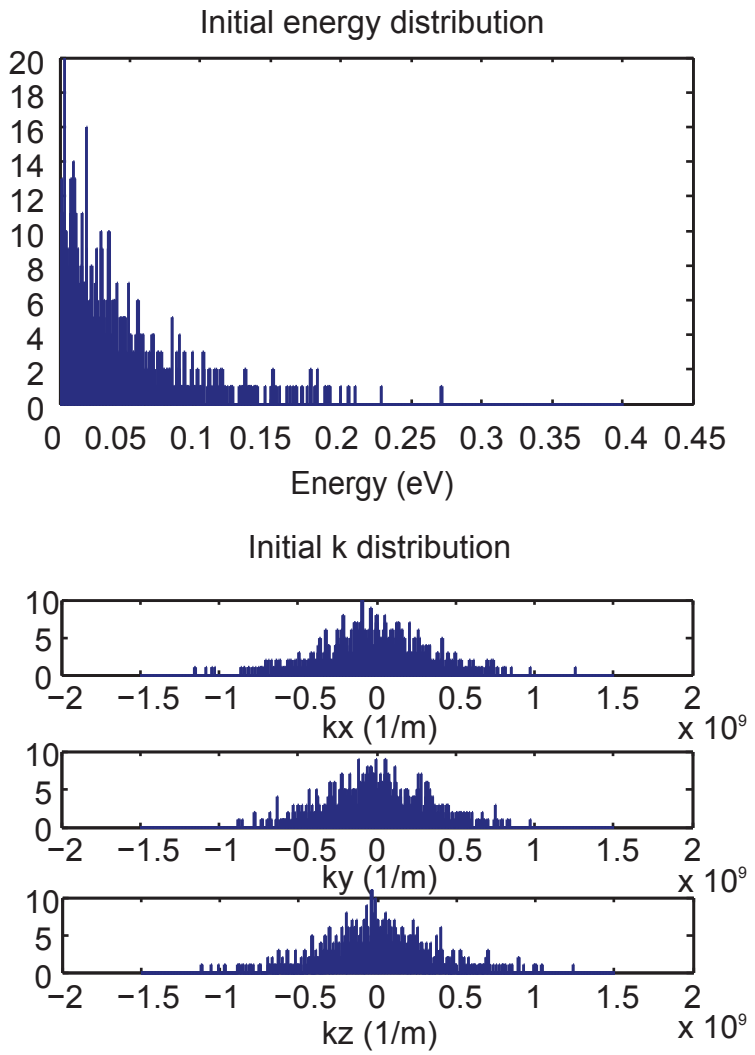

Figure 4.4: Representative initial distribution of energy and k for 10000 electrons

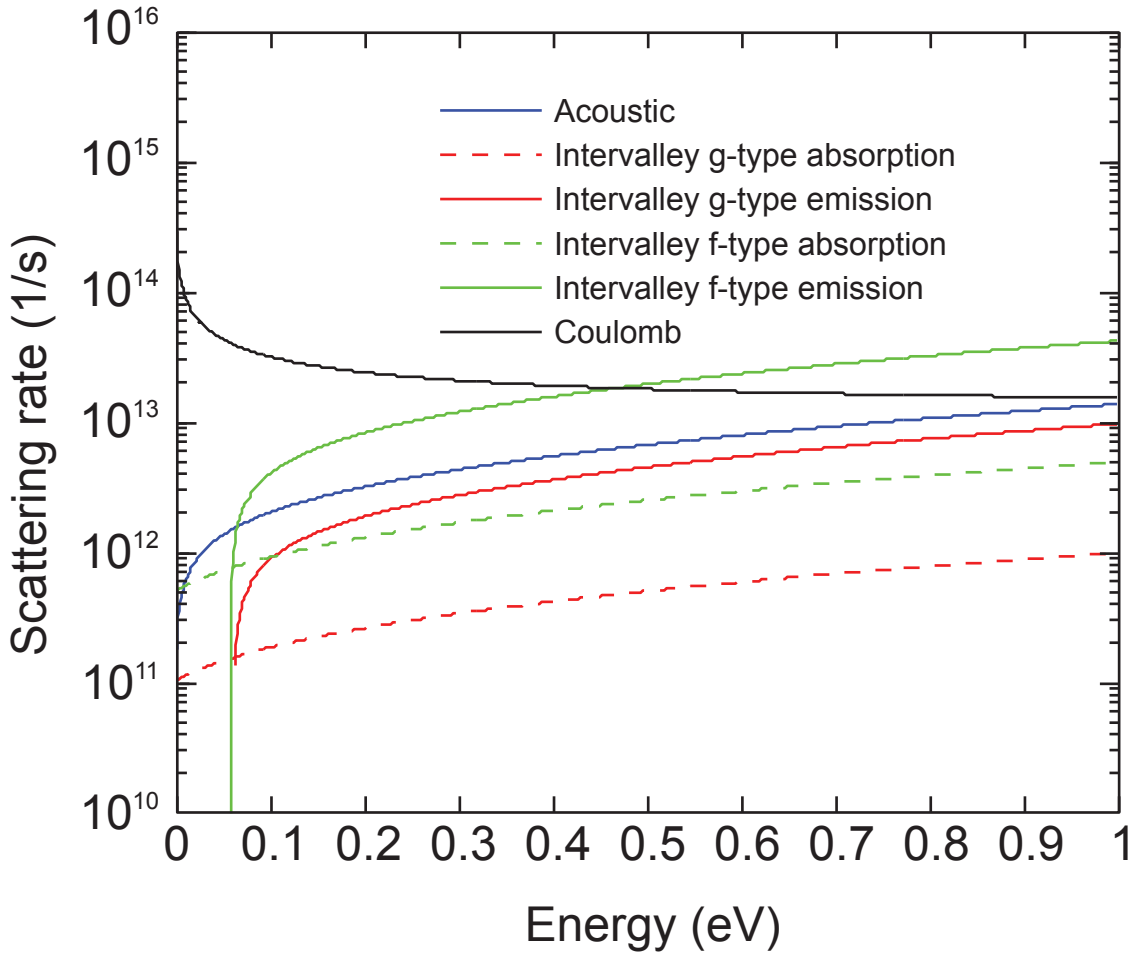

Figure 4.5: Scattering table for different mechanism for electron

ered to be isotropic inelastic scattering. Coulomb scattering is treated as anisotropic elastic scattering.

Scattering rates for electrons for different mechanisms versus energy are shown in Fig. 4.5.

4.2.2 Monte Carlo process

After initialization, the next step is true Monte Carlo process. We divide the total time window into several time steps dt. During each time step, terahertz field

is assumed to be constant.

4.2.2.1 Drift

In each time step, carriers move under the influence of terahertz field.

$$\mathbf{F} = \frac{d\mathbf{p}}{dt} = q\mathbf{E}. \tag{4.19}$$

in which $\mathbf{F}$ is the force on the carrier, $\mathbf{p}$ is the carrier momentum, $\mathbf{E}$ is the electrical field. This is called free flight. The free flight is terminated by different scattering events that change the carriers energy and momentum. In order to mimic this, for each carrier in every step, we first generate a free flight time using random time generator(Eq. 4.20). This will generate scattering events at random times with exponential inter-scattering times.

$$dt_f = -\frac{1}{\Gamma_0} ln(r_1) \tag{4.20}$$

Γ_0 is an empirical determined number. In our cases, it's assumed to be 3×10^{14} s^{-1}. During the free flight process, carrier is drifted under the influence of terahertz field. If free flight time is smaller than time step, carrier will encounter scatterings. Otherwise, we will directly go to the next time step. Because the duration of the collision is typically much shorter than the duration of the free flight between collisions, collisions are treated as instantaneous events here. After scattering, we generate a new free flight time dt_{f2} and check whether $dt_f + dt_{f2} > dt$. If $dt_f + dt_{f2} < dt$, we accelerate carrier to $dt_d = dt_{f2}$ and scatter it again.

4.2.2.2 Identification of scattering mechanism

After the process of free flight in each time step dt, momentum, position and energy of that carrier are updated at dt_f. If dt_f is smaller than dt, collisions take place and alter the carrier's momentum and energy. This change varies by adopting different scattering mechanisms. And in reality, the collision can be caused by any scattering mechanisms. In order to update the momentum and energy, we should first identify which scattering event is happening. The mathematical description of the identification procedure is to select mechanism l, if

$$\frac{\sum_{i=1}^{l-1} \frac{1}{\tau_i(E)}}{\Gamma_0} \leq r_2 < \frac{\sum_{i=1}^{l} \frac{1}{\tau_i(E)}}{\Gamma_0}, l = 1, 2, 3...k+1, \tag{4.21}$$

in which r_2 is a random number uniformly distributed from zero to one, τ_i is the scattering time for mechanism l at energy E. Details of this process is shown in Fig. 4.6.

For anisotropic elastic scattering such as Coulomb scattering, changing the wave vector $\mathbf{k}$ follows these steps.

1. Determine original θ_0 and ϕ_0.

2. Rotate original coordinate. z axis is directed along initial $\mathbf{k}$.

3. Scatter the carrier:

$$\cos(\theta) = 1 - \frac{2r}{1 + 4k^2 L_D^2 (1 - r)}, \phi = 2\pi r \tag{4.22}$$

   in which r is a random number between 0 and 1, L_D is Debye length.

4. Return to original coordinate.

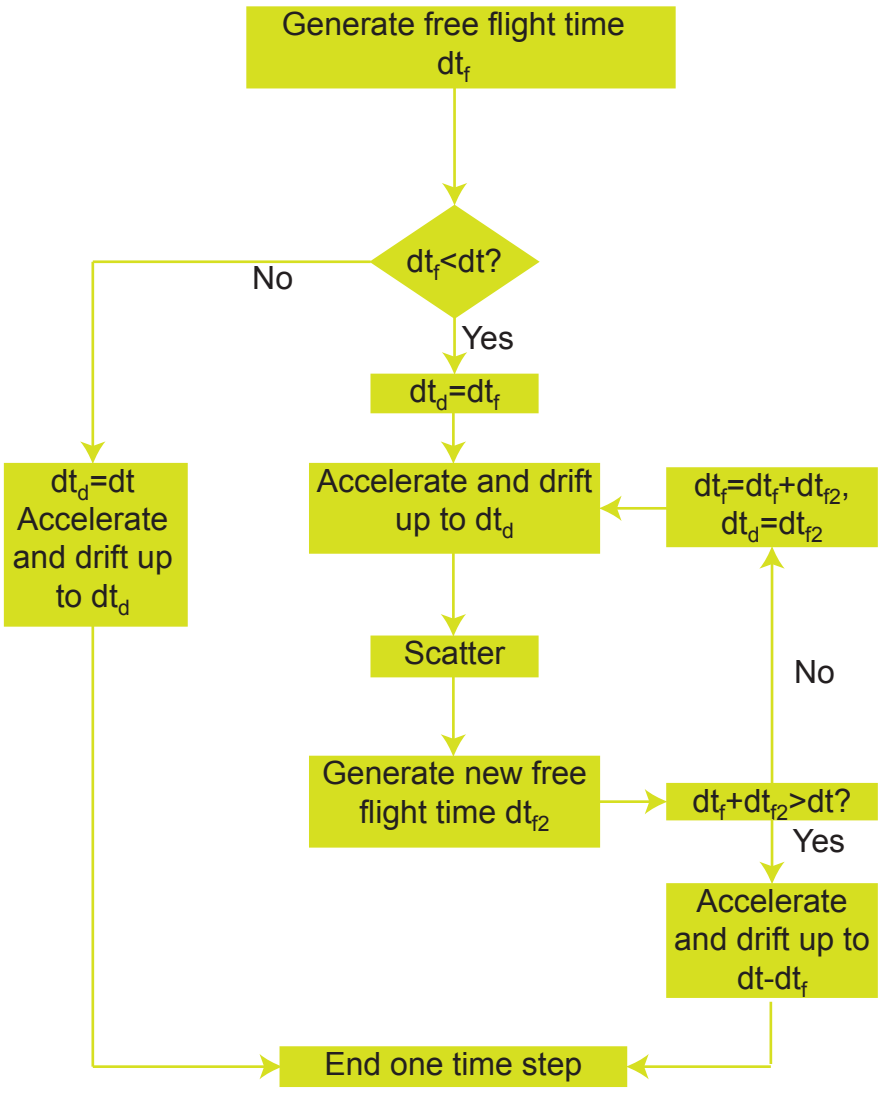

Figure 4.6: Process in each time step in Monte Carlo

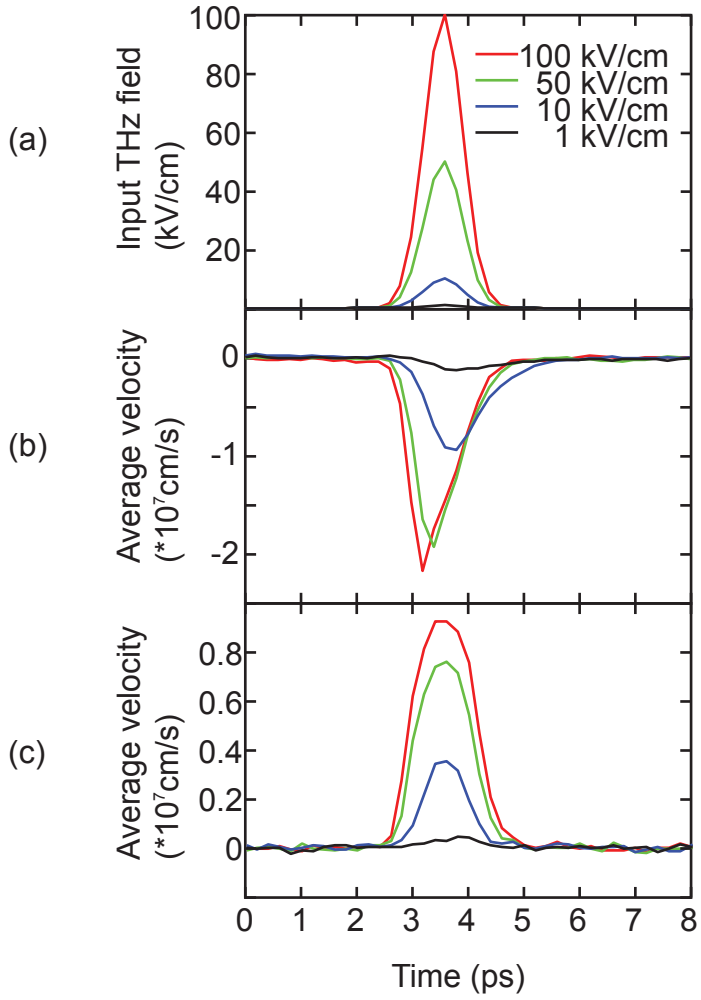

Figure 4.7: (a) Input THz signals(pulse duration 1 ps) with different intensities and corresponding (b) drift velocity of electron in intrinsic silicon and (c) drift velocity of hole in 250 $\Omega \cdot cm$ p-doped silicon in room temperature obtained from Monte Carlo simulation.

While for isotropic inelastic scattering, the angle changed by: $\cos(\theta) = 1 - 2r$, $\phi = 2\pi r$. Again r is a random number between 0 and 1.

In Fig. 4.7, we are showing electrons' average drift velocity in intrinsic silicon and holes' average drift velocity in p-doped silicon in room temperature after applying high field THz(pulse duration 1 ps) along $\langle 100 \rangle$ direction with different intensity. The reason that the velocities of hole and electron are in reverse direction is they have opposite charge sign. It's clear that drift velocity begins to saturate above 50 kV/cm.

4.3 Conclusion

In this chapter, we provide theory and simulation details about the Monte Carlo process introduced in Chapter 3. First, we describe how we estimate the THz field coupled into waveguide. Two different estimation methods are provided. Then, we show how the Monte Carlo works, including description of initialization, drift, and scattering processes. Average drift velocities of electrons and holes under high terahertz field obtained from Monte Carlo simulation is also presented. Velocity saturation phenomenon at high field is observed for both carriers.

Chapter 5: Summary and future work

5.1 Summary

In this thesis, we studied two types of silicon-based terahertz waveguides: plasmonic waveguide and ridge waveguide. Experimental results were obtained by terahertz time domain spectroscopy(THz-TDS). The low THz generation source utilized optical rectification in ZnTe crystal. The high power THz system adopted the tilted pump pulse front technique to generate THz in LN. At detection side, both used electro-optic sampling method.

In chapter 2, the plasmonic waveguide based on anisotropically etched highly doped silicon substrate is proved to be able to confine THz at its surface. Simulation performed in CST Microwave Studio, a commercial software, confirms our THz-TDS measurements. By varying the depth and width of those periodic structures, the confinement and resonant frequency can be changed. Due to the capability of confining spoof surface plasmon polaritons, this waveguide can find application in many areas, such as waveguide-based sensing and switching.

In chapter 3 and 4, we present the experimental results and theoretic study of nonlinear terahertz transmission through intrinsic and lightly doped silicon ridge waveguide. Enhanced transmission through waveguide at high THz field is observed.

A simple and efficient nonlinear Drude model assembled split-step method is proposed and compared to rigorous Monte Carlo simulation to support our observations. This research can be used for development of terahertz saturable absorber and high power terahertz guided-wave devices.

5.2 Future work

5.2.1 Impact ionization

The range of THz field considered in Chapter 3 and Chapter 4 is from 0 to 200 kV/cm. In this region, people observed enhanced transmission at high THz field through intrinsic and lightly doped silicon. Our Monte Carlo simulation suggests the physical origins of this nonlinear phenomenon come from acoustic, intervalley, and intravalley scatterings. Recently, Tarekegne fabricated antenna array on high resistivity silicon to enhance local field and observed impact ionization in this semiconductor induced by MV/cm THz field [58]. The impact ionization generated new electron-hole pair and caused a decrease in transmission, an opposite phenomenon to former results measured in the range 0 to 200 kV/cm THz field. Current Monte Carlo simulation does not include impact ionization scattering and fails to explain this phenomenon. In the future, we will add this scattering mechanism in the original Monte Carlo simulation to cover MV/cm THz-induced nonlinear transmission.

5.2.2 Frequency-dependent property of THz-induced nonlinear transmission in silicon

THz-induced absorption saturation can find potential applications in THz saturable absorbers, modulators and THz frequency converters. Those applications reply on nonlinear capability at discrete frequency. In order to examine the frequency-dependent property of this phenomenon, we explore how high field wave at specific frequency behaves after propagating in the silicon ridge waveguide using the nonlinear Drude model assembled with split step Fourier method. For simplification, we adopt sinusoidal waveform to do simulation. Several results for different frequencies are shown in Fig. 5.1. The input THz waves are with the form:

$$E_{input} = E_{peak} \times \sin \omega t, \omega = 2\pi f. \tag{5.1}$$

Frequencies f simulated are 0.1 THz, 0.5 THz, 1 THz, 5 THz, and 10 THz. The sample parameters are the same as our p-doped silicon. E_{peak} is the input peak field and assigned to be 100 kV/cm for all the cases. Linear results(green) calculated from conventional Drude model are also displayed. From these simulated results, we can predict the nonlinear effects are very obvious for frequencies below 1 THz. Above 5 THz, the enhanced transmission is barely observed. Experiments is needed to confirm these simulations.

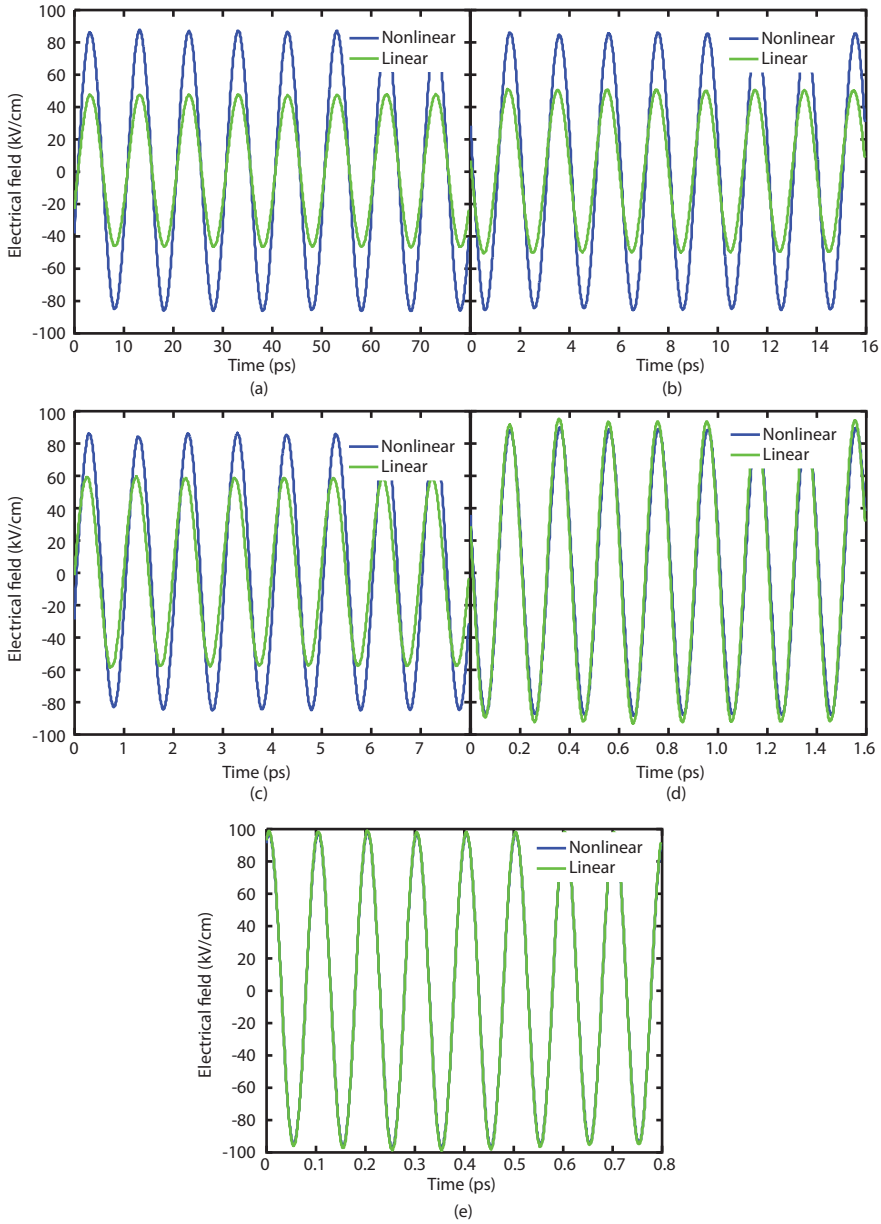

Figure 5.1: Nonlinear and linear Drude TE mode simulation results for (a)f=0.1 THz, (b)f=0.5 THz, (c)f=1 THz, (d)f=5 THz and (e)f=10 THz input fields after 2 cm propagation in p-doped silicon waveguide.

Chapter A: List of publications

A.1 Journal

1. **S. Li**, M. M. Jadidi, T. E. Murphy, and G. Kumar. Terahertz surface plasmon polaritons on a semiconductor surface structured with periodic V-grooves, *Opt. Express*, 21(6):70417049, 2013.

2. **S. Li**, M. M. Jadidi, T. E. Murphy, and G. Kumar. Plasmonic Terahertz Waveguide Based on Anisotropically Etched Silicon Substrate, *IEEE Transactions on Terahertz Science and Technology*, 4(4):454458, 2014.

3. **S. Li**, G. Kumar, and T. E. Murphy. Terahertz nonlinear conduction and absorption saturation in silicon waveguides. *Optica*, 2(6):553-557, 2015.

4. G. Kumar, **S. Li**, M. M. Jadidi, and T. E. Murphy. Terahertz surface plasmon waveguide based on a one-dimensional array of silicon pillars, *New J. Phys.*, 15(8), 085031, 2013.

5. X. Cai, A. B. Sushkov, R. J. Suess, M. M. Jadidi, G. S. Jenkins, L. O. Nyakiti, R. L. Myers-Ward, **S. Li**, J. Yan, D. K. Gaskill, T. E. Murphy, H. D. Drew, M. S. Fuhrer. Sensitive room-temperature terahertz detection via photother-

moelectric effect in graphene, *Nature Nanotechnology*, Sept. 16. 2014.

A.2 Conference

1. **S. Li**, Kumar, and T. E. Murphy. Terahertz Absorption Saturation in Intrinsic Silicon Dielectric Ridge Waveguides, *CLEO*: 2014, STh3F.3, 2014.

2. G. Kumar, **S. Li**, M. M. Jadidi, and T. E. Murphy. Anisotropically Etched Silicon Surfaces for Planar Plasmonic Terahertz Guided Wave Devices, *CLEO*: 2014, JW2A.97, 2014.

3. M. M. Jadidi , G. Kumar, **S. Li**, and T. E. Murphy. Terahertz plasmonic waveguide based on periodically structured silicon surface, *CLEO*: 2013, CTh1K.1, 2013.

Bibliography

[1] Jianming Dai, Jiangquan Zhang, Weili Zhang, and D. Grischkowsky. Terahertz time-domain spectroscopy characterization of the far-infrared absorption and index of refraction of high-resistivity, float-zone silicon. *J. Opt. Soc. Am. B*, 21(7):1379–1386, 2004.

[2] J. B. Pendry, L. Martn-Moreno, and F. J. Garcia-Vidal. Mimicking surface plasmons with structured surfaces. *Science*, 305(5685):847–848, 2004.

[3] János Hebling, Matthias C. Hoffmann, Harold Y. Hwang, Ka-Lo Yeh, and Keith A. Nelson. Observation of nonequilibrium carrier distribution in Ge, Si, and GaAs by terahertz pump terahertz probe measurements. *Phys. Rev. B*, 81:035201, 2010.

[4] G. Kaur, Pengyu Han, and X.-C. Zhang. Terahertz induced nonlinear effects in doped Silicon observed by open-aperture Z-scan. In *2010 35th International Conference on Infrared Millimeter and Terahertz Waves (IRMMW-THz)*, pages 1–2, 2010.

[5] C. Canali, G. Majni, R. Minder, and G. Ottaviani. Electron and hole drift velocity measurements in silicon and their empirical relation to electric field and temperature. *Electron Devices, IEEE Transactions on*, 22(11):1045–1047, 1975.

[6] Louise Ho, M Pepper, and P Taday. Terahertz spectroscopy: Signatures and fingerprints. *Nature Photonics*, 2:541–543, 2008.

[7] P.H. Siegel. Terahertz technology in biology and medicine. In *Microwave Symposium Digest, 2004 IEEE MTT-S International*, volume 3, pages 1575–1578, 2004.

[8] Ruth M. Woodward. Terahertz technology in global homeland security (invited paper). *Proc. SPIE*, 5781:22–31, 2005.

[9] K. Ishigaki, M. Shiraishi, S. Suzuki, M. Asada, N. Nishiyama, and S. Arai. Direct intensity modulation and wireless data transmission characteristics of terahertz-oscillating resonant tunnelling diodes. *Electronics Letters*, 48(10):582–583, 2012.

[10] M Tonouchi. Cutting-edge terahertz technology. *Nature Photonics*, 1:97–105, 2007.

[11] J. S. Melinger, N. Laman, S. S. Harsha, and D. Grischkowsky. Line narrowing of terahertz vibrational modes for organic thin polycrystalline films within a parallel plate waveguide. *Appl. Phys. Lett.*, 89(25):251110, 2006.

[12] M Nagel, M Frst, and H Kurz. Thz biosensing devices: fundamentals and technology. *Journal of Physics: Condensed Matter*, 18(18):S601, 2006.

[13] M. M. Awad and R. A. Cheville. Transmission terahertz waveguide-based imaging below the diffraction limit. *Appl. Phys. Lett.*, 86(22):221107, 2005.

[14] Q. Gan, Z. Fu, Y. J. Ding, and F. J. Bartoli. Ultrawide-bandwidth slow-light system based on thz plasmonic graded metallic grating structures. *Phys. Rev. Lett.*, 100:256803, 2008.

[15] H.-T. Chen, W. J. Padilla, J. M. O. Zide, A. C. Gossard, A. J. Taylor, and R. D. Averitt. Active terahertz metamaterial devices. *Nature*, 444:597–600, 2006.

[16] S. Coleman and D. Grischkowsky. Parallel plate THz transmitter. *Appl. Phys. Lett.*, 84(5):654–656, 2004.

[17] J. Liu, R. Mendis, and D. M. Mittleman. The transition from a TEM-like mode to a plasmonic mode in parallel-plate waveguides. *Appl. Phys. Lett.*, 98(23):231113, 2011.

[18] K. Wang and D. M. Mittleman. Metal wires for terahertz wave guiding. *Nature*, 432:376–379, 2004.

[19] Alireza Hassani, Alexandre Dupuis, and Maksim Skorobogatiy. Porous polymer fibers for low-loss Terahertz guiding. *Opt. Express*, 16(9):6340–51, April 2008.

[20] Li-Jin Chen, Hung-Wen Chen, Tzeng-Fu Kao, Ja-Yu Lu, and Chi-Kuang Sun. Low-loss subwavelength plastic fiber for terahertz waveguiding. *Opt. Lett.*, 31(3):308–310, 2006.

[21] Shanshan Li, Mohammad M. Jadidi, Thomas E. Murphy, and Gagan Kumar. Terahertz surface plasmon polaritons on a semiconductor surface structured with periodic v-grooves. *Opt. Express*, 21(6):7041–7049, 2013.

[22] Shanshan Li, Mohamad M. Jadidi, Thomas E. Murphy, and Gagan Kumar. Plasmonic terahertz waveguide based on anisotropically etched silicon substrate. *IEEE Trans. Terahertz Sci. Technol.*, 4(4):454–458, 2014.

[23] Shanshan Li, Gagan Kumar, and Thomas E. Murphy. Terahertz nonlinear conduction and absorption saturation in silicon waveguides. *Optica*, 2(6):553–557, 2015.

[24] R. W. McGowan, G. Gallot, and D. Grischkowsky. Propagation of ultrawideband short pulses of terahertz radiation through submillimeter-diameter circular waveguides. *Opt. Lett.*, 24(20):1431–1433, 1999.

[25] R. Mendis and D. Grischkowsky. Undistorted guided-wave propagation of subpicosecond terahertz pulses. *Opt. Lett.*, 26(11):846–848, Jun 2001.

[26] Chih-Hsien Lai, Yu-Chun Hsueh, Hung-Wen Chen, Yuh jing Huang, Hung chun Chang, and Chi-Kuang Sun. Low-index terahertz pipe waveguides. *Opt. Lett.*, 34(21):3457–3459, 2009.

[27] Shaghik Atakaramians, Shahraam Afshar V., Michael Nagel, Henrik K. Rasmussen, Ole Bang, Tanya M. Monro, and Derek Abbott. Direct probing of evanescent field for characterization of porous terahertz fibers. *Appl. Phys. Lett.*, 98(12):121104, 2011.

[28] Martin van Exter and D. Grischkowsky. Optical and electronic properties of doped silicon from 0.1 to 2 thz. *Appl. Phys. Lett.*, 56(17):1694–1696, 1990.

[29] S. Nashima, O. Morikawa, K. Takata, and M. Hangyo. Measurement of optical properties of highly doped silicon by terahertz time domain reflection spectroscopy. *Appl. Phys. Lett.*, 79(24):3923–3925, 2001.

[30] Robert P. Lucht. In *Drude Model for dielectric constant of metals.*, 2006.

[31] J. B. Pendry, A. J. Holden, W. J. Stewart, and I. Youngs. Extremely low frequency plasmons in metallic mesostructures. *Phys. Rev. Lett.*, 76:4773–4776, 1996.

[32] G. Kumar, S. Pandey, A. Cui, and A. Nahata. Planar plasmonic terahertz waveguides based on periodically corrugated metal films. *New J. Phys.*, 13(3):033024, 2011.

[33] Linfang Shen, Xudong Chen, and Tzong-Jer Yang. Terahertz surface plasmon polaritons on periodically corrugated metal surfaces. *Opt. Express*, 16(5):3326–3333, 2008.

[34] A. I. Fernández-Domínguez, E. Moreno, L. Martín-Moreno, and F. J. Garcia-Vidal. Terahertz wedge plasmon polaritons. *Opt. Lett.*, 34:2063, 2009.

[35] Y. Shen, T. Watanabe, D. A. Arena, C.-C. Kao, J. B. Murphy, T. Y. Tsang, X. J. Wang, and G. L. Carr. Nonlinear cross-phase modulation with intense single-cycle terahertz pulses. *Phys. Rev. Lett.*, 99:043901, 2007.

[36] D. You, D. R. Dykaar, R. R. Jones, and P. H. Bucksbaum. Generation of high-power sub-single-cycle 500-fs electromagnetic pulses. *Opt. Lett.*, 18(4):290–292, Feb 1993.

[37] F. Blanchard, L. Razzari, H.C. Bandulet, G. Sharma, R. Morandotti, J. C. Kieffer, T. Ozaki, M. Reid, H. F. Tiedje, H. K. Haugen, and F. A. Hegmann. Generation of 1.5 uj single-cycle terahertz pulses by optical rectification from a large aperture znte crystal. *Opt. Express*, 15(20):13212–13220, Oct 2007.

[38] Jae-Hyeok Jeong, Bong-Joo Kang, Ji-Soo Kim, Mojca Jazbinsek, Seung-Heon Lee, Seung-Chul Lee, In-Hyung Baek, Hoseop Yun, Jongtaek Kim, Yoon Sup Lee, Jae-Hyeok Lee, Jae-Ho Kim, and Fabian Rotermund & O-Pil Kwon. High-power broadband organic thz generator. *Scientific Reports*, 3(3200), 2013.

[39] Mostafa Shalaby and Christoph P. Hauri. Demonstration of a low-frequency three-dimensional terahertz bullet with extreme brightness. *Nature Communications*, 6(5976), 2015.

[40] T I Oh, Y S You, N Jhajj, E W Rosenthal, H M Milchberg, and K Y Kim. Intense terahertz generation in two-color laser filamentation: energy scaling with terawatt laser systems. *New J. Phys.*, 15(7):075002, 2013.

[41] D. J. Cook and R. M. Hochstrasser. Intense terahertz pulses by four-wave rectification in air. *Opt. Lett.*, 25(16):1210–1212, 2000.

[42] János Hebling, Ka-Lo Yeh, Matthias C. Hoffmann, Balázs Bartal, and Keith A. Nelson. Generation of high-power terahertz pulses by tilted-pulse-front excitation and their application possibilities. *J. Opt. Soc. Am. B*, 25(7):B6–B19, 2008.

[43] H. Hirori, a. Doi, F. Blanchard, and K. Tanaka. Single-cycle terahertz pulses with amplitudes exceeding 1 MV/cm generated by optical rectification in $LiNbO_3$. *Appl. Phys. Lett.*, 98(9):091106, 2011.

[44] K. Y. KIM, A. J. TAYLOR, and J. H. GLOWNIA & G. RODRIGUEZ. Coherent control of terahertz supercontinuum generation in ultrafast lasergas interactions. *Nature Photonics*, 2:605–609, 2008.

[45] Matteo Clerici, Marco Peccianti, Bruno E. Schmidt, Lucia Caspani, Mostafa Shalaby, Mathieu Giguère, Antonio Lotti, Arnaud Couairon, Fran çois Légaré, Tsuneyuki Ozaki, Daniele Faccio, and Roberto Morandotti. Wavelength scaling of terahertz generation by gas ionization. *Phys. Rev. Lett.*, 110:253901, 2013.

[46] J. A. Fülöp, L Pálfalvi, S Klingebiel, G Almási, F Krausz, S Karsch, and J Hebling. Generation of sub-mJ terahertz pulses by optical rectification. *Opt. Lett.*, 37(4):557–559, 2012.

[47] Janos Hebling, Gabor Almasi, Ida Kozma, and Jurgen Kuhl. Velocity matching by pulse front tilting for large area thz-pulse generation. *Opt. Express*, 10(21):1161–1166, 2002.

[48] P. Gaal, K. Reimann, M. Woerner, T. Elsaesser, R. Hey, and K. H. Ploog. Nonlinear Terahertz Response of n-Type GaAs. *Phys. Rev. Lett.*, 96:187402, 2006.

[49] Matthias C. Hoffmann, János Hebling, Harold Y. Hwang, Ka-Lo Yeh, and Keith A. Nelson. THz-pump/THz-probe spectroscopy of semiconductors at high field strengths. *J. Opt. Soc. Am. B*, 26(9):A29–A34, 2009.

[50] G. Sharma, I. Al-Naib, H. Hafez, R. Morandotti, D. G. Cooke, and T. Ozaki. Carrier density dependence of the nonlinear absorption of intense THz radiation in GaAs. *Opt. Express*, 20(16):18016–18024, 2012.

[51] Dmitry Turchinovich, Jørn M. Hvam, and Matthias C. Hoffmann. Self-phase modulation of a single-cycle terahertz pulse by nonlinear free-carrier response in a semiconductor. *Phys. Rev. B*, 85:201304, 2012.

[52] Young-Gyun Jeong, Michael J. Paul, Seung-Hyun Kim, Ki-Ju Yee, Dai-Sik Kim, and Yun-Shik Lee. Large enhancement of nonlinear terahertz absorption in intrinsic GaAs by plasmonic nano antennas. *Appl. Phys. Lett.*, 103(17):171109, 2013.

[53] P. Bowlan, W. Kuehn, K. Reimann, M. Woerner, T. Elsaesser, R. Hey, and C. Flytzanis. High-Field Transport in an Electron-Hole Plasma: Transition from Ballistic to Drift Motion. *Phys. Rev. Lett.*, 107:256602, 2011.

[54] Matthias C. Hoffmann and Dmitry Turchinovich. Semiconductor saturable absorbers for ultrafast terahertz signals. *Appl. Phys. Lett.*, 96(15):151110, 2010.

[55] H. Wen, M. Wiczer, and A. M. Lindenberg. Ultrafast electron cascades in semiconductors driven by intense femtosecond terahertz pulses. *Phys. Rev. B*, 78:125203, 2008.

[56] Matthias C. Hoffmann, János Hebling, Harold Y. Hwang, Ka-Lo Yeh, and Keith A. Nelson. Impact ionization in InSb probed by terahertz pump/terahertz probe spectroscopy. *Phys. Rev. B*, 79:161201, 2009.

[57] F. Junginger, B. Mayer, C. Schmidt, O. Schubert, S. Mährlein, A. Leitenstorfer, R. Huber, and A. Pashkin. Nonperturbative Interband Response of a Bulk InSb Semiconductor Driven Off Resonantly by Terahertz Electromagnetic Few-Cycle Pulses. *Phys. Rev. Lett.*, 109:147403, 2012.

[58] Abebe T Tarekegne, Krzysztof Iwaszczuk, Maksim Zalkovskij, Andrew C Strikwerda, and Peter U Jepsen. Impact ionization in high resistivity silicon induced by an intense terahertz field enhanced by an antenna array. *New J. Phys.*, 17(4):043002, 2015.

[59] Kebin Fan, Harold Y. Hwang, Mengkun Liu, Andrew C. Strikwerda, Aaron Sternbach, Jingdi Zhang, Xiaoguang Zhao, Xin Zhang, Keith A. Nelson, and Richard D. Averitt. Nonlinear terahertz metamaterials via field-enhanced carrier dynamics in gaas. *Phys. Rev. Lett.*, 110(21):217404, 2013.

[60] Ibraheem Al-Naib, Gargi Sharma, Marc M. Dignam, Hassan Hafez, Akram Ibrahim, David G. Cooke, Tsuneyuki Ozaki, and Roberto Morandotti. Effect of local field enhancement on the nonlinear terahertz response of a silicon-based metamaterial. *Phys. Rev. B*, 88:195203, 2013.

[61] Ganesh Samudra, Soo Jin Chua, Ajoy K. Ghatak, and Vijay K. Arora. High-field electron transport for ellipsoidal multivalley band structure of silicon. *J. Appl. Phys.*, 72(10):4700, 1992.

[62] W. Maes, K. De Meyer, and R. Van Overstraeten. Impact ionization in silicon: A review and update. *Solid-State Electronics*, 33(6):705–718, 1990.

[63] Lianghong Yin and Govind P. Agrawal. Impact of two-photon absorption on self-phase modulation in silicon waveguides. *Opt. Lett.*, 32(14):2031–2033, 2007.

[64] H. K. Tsang, C. S. Wong, T. K. Liang, I. E. Day, S. W. Roberts, A. Harpin, J. Drake, and M. Asghari. Optical dispersion, two-photon absorption and self-phase modulation in silicon waveguides at 1.5μm wavelength. *Appl. Phys. Lett.*, 80(3):416–418, 2002.

[65] H. Raether. *Surface Plasmons on Smooth and Rough Surfaces and on Gratings*, volume 111 of *Springer Tracts in Modern Physics*. Springer-Verlag, 1988.

[66] T.-I. Jeon and D. Grischkowsky. THz Zenneck surface wave (THz surface plasmon) propagation on a metal sheet. *Appl. Phys. Lett.*, 88(6):061113, 2006.

[67] P. Berini. Long-range surface plasmon polaritons. *Adv. Opt. Photon.*, 1:484–588, 2009.

[68] S. A. Maier and S. R. Andrews. Terahertz pulse propagation using Plasmon-polariton-like surface modes on structures conductive surface. *Appl. Phys. Lett.*, 88:251120, 2006.

[69] G. Kumar and V. K. Tripathi. Surface enhanced Raman Scattering of a surface plasma wave. *J. Phys. D: Appl. Phys.*, 39:4436, 2006.

[70] Z. Tian, R. Singh, J. Han, J. Gu, Q. Xing, J. Wu, and W. Zhang. Terahertz superconducting plasmonic hole array. *Opt. Lett.*, 35(21):3586–3588, 2010.

[71] J. N. Anker, W. P. Hall, O. Lyandres, N. C. Shah, J. Zhao, and R. P. Van Duyne. Biosensing with plasmonic nanosensors. *Nature Mater.*, 7:442, 2008.

[72] S. Palomba, M. Danckwerts, and L. Novotny. Nonlinear plasmonics with gold nanoparticle antennas. *J. Opt. A: Pure Appl. Opt.*, 11:114030, 2009.

[73] P. L. Stiles, J. A. Dieringer, N. C. Shah, and R. P. Van Duyne. Surface-Enhanced Raman Spectroscopy. *Annu. Rev. Anal. Chem.*, 1:601, 2008.

[74] A. V. Zayats, I. I. Smolyaninov, and A. A. Maradudin. Nano-optics of surface plasmon polaritons. *Phys. Rep.*, 408(34):131 – 314, 2005.

[75] Z. Ruan and M. Qiu. Slow electromagnetic wave guided in subwavelength region along one-dimensional periodically structured metal surface. *Appl. Phys. Lett.*, 90:201906, 2007.

[76] W. Zhu, A. Agrawal, A. Cui, G. Kumar, and A. Nahata. Engineering the propagation properties of planar plasmonic terahertz waveguides. *IEEE J. of Select. Topics Quant. Electron.*, 17:146, 2011.

[77] C. R. Williams, S. R. Andrews, Maier. S. A., A. I. Fernandez-Dominguez, L. Martin-Moreno, and F. J. Garcia-Vidal. Highly confined guiding of terahertz surface plasmon polaritons on structured metal surfaces. *Nature Photonics*, 2:175–179, 2008.

[78] F. J. Garcia-Vidal, L. Martín-Moreno, and J. B. Pendry. Surfaces with holes in them: new plasmonic metamaterials. *J. Opt. A: Pure Appl. Opt.*, 7:S97–S101, 2005.

[79] Gagan Kumar, Albert Cui, Shashank Pandey, and Ajay Nahata. Planar terahertz waveguides based on complementary split ring resonators. *Opt. Express*, 19(2):1072–1080, 2011.

[80] J. Gomez Rivas, M. Kuttge, P. Haring Bolivar, and H. Kurz. Propagation of Surface Plasmon Polaritons on Semiconductor Gratings. *Phys. Rev. Lett.*, 93:256804, 2004.

[81] W. Zhao, O. M. Eldaiki, R. Yang, and Z. Lu. Deep subwavelength waveguiding and focusing based on designer surface plasmons. *Opt. Express*, 18:21498, 2010.

[82] T. Jiang, L. Shen, J.-J. Wu, T.-J. Yang, Z. Ruan, and L. Ran. Realization of tightly confined channel plasmon polaritons at low frequencies. *Appl. Phys. Lett.*, 99:261103, 2011.

[83] S. I. Bozhevolnyi and J. Jung. Scaling for gap plasmon based waveguides. *Opt. Express*, 16:2676, 2008.

[84] F. Liu, S. Peng, H. Jia, M. Ke, and Z. Liu. Strongly localized acoustic surface waves propagating along a V-groove. *Appl. Phys. Lett.*, 94:023505, 2009.

[85] Y. J. Zhou, Q. Jiang, and T. J. Cui. Bidirectional bending splitter of designer surface plasmons. *Appl. Phys. Lett.*, 99:111904, 2011.

[86] C. L. C. Smith, B. Desiatov, I. Goykmann, I. Fernandez-Cuesta, U. Levy, and A. Kristensen. Plasmonic V-groove waveguides with Bragg grating filters via nanoimprint lithography. *Opt. Express*, 20:5696, 2012.

[87] S. I. Bozhevolnyi, V. S. Volkov, E. Devaux, and T. W. Ebbesen. Channel Plasmon-Polariton Guiding by Subwavelength Metal Grooves. *Phys. Rev. Lett.*, 95:046802, 2005.

[88] S. I. Bozhevolnyi, V. S. Volkov, E. Devaux, J.-Yves Laluet, and T.W. Ebbesen. Channel plasmon subwavelength waveguide components including interferometers and ring resonators. *Nature Lett.*, 440:508, 2006.

[89] J. J. Wood, L. A. Tomlinson, O. Hess, S. A. Maier, and A. I. Fernández-Domínguez. Spoof plasmon polaritons in slanted geometries. *Phys. Rev. B*, 85:075441, 2012.

[90] S. Sriram and E. P. Supertzi. Novel V-groove structures on silicon. *Appl. Opt.*, 24(12):1784–1787, 1985.

[91] U. Fano. Effects of configuration interaction on intensities amd phase shifts. *Phys. Rev.*, 124:1866, 1961.

[92] A. Agrawal, T. Matsui, Z. V. Vardeny, and A. Nahata. Terahertz transmission properties of quaisperiodic and aperiodic aperature arrays. *J. Opt. Soc. Am. B*, 24:2545, 2007.

[93] D. Grischkowsky, Søren Keiding, Martin van Exter, and Ch. Fattinger. Far-infrared time-domain spectroscopy with terahertz beams of dielectrics and semiconductors. *J. Opt. Soc. Am. B*, 7(10):2006–2015, Oct 1990.

[94] Cristo M. Yee and Mark S. Sherwin. High-Q terahertz microcavities in silicon photonic crystal slabs. *Appl. Phys. Lett.*, 94(15):154104, 2009.

[95] Haisheng Rong, Ansheng Liu, Richard Jones, Oded Cohen, Dani Hak, Remus Nicolaescu, Alexander Fang, and Mario Paniccia. An all-silicon Raman laser. *Nature*, 433(7023):292–294, 2005.

[96] Mark A. Foster, Amy C. Turner, Jay E. Sharping, Bradley S. Schmidt, Michal Lipson, and Alexander L. Gaeta. Broad-band optical parametric gain on a silicon photonic chip. *Nature*, 441(7096):960–963, 2006.

[97] Q. Lin, Oskar J. Painter, and Govind P. Agrawal. Nonlinear optical phenomena in silicon waveguides: modeling and applications. *Opt. Express*, 15(25):16604–16644, 2007.

[98] J. Zhang, Q. Lin, G. Piredda, R. W. Boyd, G. P. Agrawal, and P. M. Fauchet. Anisotropic nonlinear response of silicon in the near-infrared region. *Appl. Phys. Lett.*, 91(7):071113, 2007.

[99] Bahram Jalali. Silicon photonics: Nonlinear optics in the mid-infrared. *Nature Photonics*.

[100] Bart Kuyken, Xiaoping Liu, Richard M. Osgood Jr., Roel Baets, Günther Roelkens, and William M. J. Green. Mid-infrared to telecom-band supercontinuum generation in highly nonlinear silicon-on-insulator wire waveguides. *Opt. Express*, 19(21):20172–20181, 2011.

[101] K.-L. Yeh, M. C. Hoffmann, J. Hebling, and Keith A. Nelson. Generation of 10μJ ultrashort terahertz pulses by optical rectification. *Appl. Phys. Lett.*, 90(17):171121, 2007.

[102] M. A. Seo, A. J. L. Adam, J. H. Kang, J. W. Lee, S. C. Jeoung, Q. H. Park, P. C. M. Planken, and D. S. Kim. Fourier-transform terahertz near-field imaging of one-dimensional slit arrays: mapping of electric-field-, magnetic-field-, and Poynting vectors. *Opt. Express*, 15(19):11781–11789, 2007.

[103] Reshmi Chakkittakandy, Jos A. Corver, and Paul C. Planken. Quasi-near field terahertz generation and detection. *Opt. Express*, 16(17):12794–12805, 2008.

[104] J. P. Nougier, J. C. Vaissiere, D. Gasquet, J. Zimmermann, and E. Constant. Determination of transient regime of hot carriers in semiconductors, using the relaxation time approximations. *J. Appl. Phys.*, 52(2):825–832, 1981.

[105] W. Hänsch and M. Miura-Mattausch. The hot electron problem in small semiconductor devices. *J. Appl. Phys.*, 60(2):650–656, 1986.

[106] Mark Lundstrom. *Fundamentals of Carrier Transport*. Cambridge University Press, 2nd edition, 2000.

[107] T. Grasser, Ting-Wei Tang, H. Kosina, and S. Selberherr. A review of hydrodynamic and energy-transport models for semiconductor device simulation. *Proc. IEEE*, 91(2):251–274, 2003.

[108] K. J. Willis, S. C. Hagness, and I. Knezevic. Terahertz conductivity of doped silicon calculated using the ensemble Monte Carlo/finite-difference time-domain simulation technique. *Appl. Phys. Lett.*, 96(6):062106, 2010.

[109] Dragica Vasileska, Stephen M. Goodnick, and Gerhard Klimeck. *Computational Electronics: Semiclassical and Quantum Device Modeling and Simulation*. CRC Press, 2010, 2010.

[110] S.H. Gamal and T.S. Al-Harbi. Simple and efficient monte carlo simulation of high-temperature hole transport in silicon and diamond. *Microelectronics Journal*, 32(4):327 – 329, 2001.